

UNCLASSIFIED

AD NUMBER
AD487242
NEW LIMITATION CHANGE
TO Approved for public release, distribution unlimited
FROM Distribution authorized to U.S. Gov't. agencies and their contractors; Administrative/Operational Use; 01 JUL 1966. Other requests shall be referred to Air Force Rocket Propulsion Laboratory, Edwards AFB, CA.
AUTHORITY
AFRPL ltr dtd 20 Dec 1971

THIS PAGE IS UNCLASSIFIED

487642

LIQUID ROCKET ENGINE
COMBUSTION INSTABILITY STUDIES

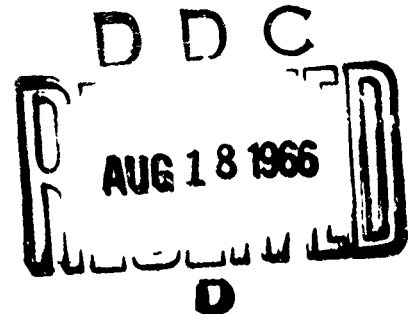
Final Report, Contract No. AF 04(611)-10542

AFRFL-TR-66-125

AIR FORCE ROCKET PROPULSION LABORATORY
RESEARCH AND TECHNOLOGY DIVISION
AIR FORCE SYSTEMS COMMAND
UNITED STATES AIR FORCE
EDWARDS, CALIFORNIA

Project No. 3505, Task No. 04

1 July 1966



DYNAMIC SCIENCE, A DIVISION
of MARSHALL INDUSTRIES
1900 Walker Avenue
Monrovia, California 91016

**LIQUID ROCKET ENGINE
COMBUSTION INSTABILITY STUDIES**

Final Report, Contract No. AF 04(611)-10542

AFRFL-TR-66-125

For the

**AIR FORCE ROCKET PROPULSION LABORATORY
RESEARCH AND TECHNOLOGY DIVISION
AIR FORCE SYSTEMS COMMAND
UNITED STATES AIR FORCE
Edwards, California**

Project No. 3505, Task No. 04

Prepared by

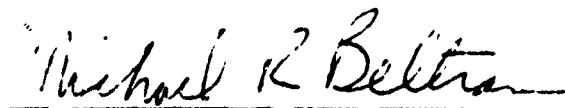
**M. R. Beltran
B. P. Breen
T. C. Kosvic
C. F. Sanders
R. J. Hoffman
R. O. Wright**

**DYNAMIC SCIENCE, A DIVISION
of MARSHALL INDUSTRIES
1900 Walker Avenue
Monrovia, California 91016**

FOREWORD

This final report describes the development of various analytical techniques to predict combustion instability in liquid rocket engines. The report was prepared by M. R. Beltran, B. P. Breen, T. C. Kosvic, C. F. Sanders, R. J. Hoffman, and R. O. Wright of the Dynamic Science Division of Marshall Industries, Propulsion Department, 1900 Walker Avenue, Monrovia, California. The work was funded on Air Force Contract No. AF 04(611)-10542 under Task No. 04 of Project No. 3505, during the period January 1, 1965 through December 30, 1965. This contract was administered under the direction of R. R. Weiss and Lt. J. J. Stewart of the Rocket Propulsion Laboratory, Edwards Air Force Base, Edwards, California.

Approved:


Michael R. Beltran
Michael R. Beltran
Director of Propulsion


Melvin Gerstein, Ph.D.
Melvin Gerstein, Ph.D.
President

NOTICES

This report may be reproduced to satisfy the needs of U.S. Government Agencies. No other reproduction is authorized except with the permission of the U.S. Air Force, Rocket Propulsion Laboratory, Edwards Air Force Base, California. The distribution of this report is limited because general foreign dissemination is not desired.

Qualified users may obtain copies of this report from the Defense Documentation Center.

ABSTRACT

This final report describes the work performed on various combustion problems related to high frequency instability in liquid rocket engines. Using the steady-state and instability computer programs developed under this study, a parametric investigation was conducted. This investigation determined the influence of droplet radius, droplet distribution, injection velocity, chamber pressure, and mixture ratio on the minimum threshold disturbance required to trigger combustion instability in a Transtage type engine configuration. The propellant combination considered was monomethylhydrazine/nitrogen tetroxide. Results of the study show that increases in injection velocity and droplet distribution increased stability. An increase in chamber pressure, based on constant flow rate, increased stability while increases in chamber pressure, at a constant contraction ratio, decreased stability. There appears to be a droplet size for minimum stability, with changes in either direction resulting in improved stability. Results also show that due to the vapor phase reactions, monomethylhydrazine/nitrogen tetroxide vaporize at approximately the same rate. Thus, the oxidizer or fuel could be made to control the combustion process by slight changes in the injector and engine parameters. For the engine configuration studied the oxidizer vaporized slower than the fuel. A program review, work on droplet atomization, and a study of hypergolic liquid phase reactions is also reported. The review summarizes the work reported in the Semiannual (DSC SN-68-51) and Special report (AFRPL-TR-65-254) written under this program.

TABLE OF CONTENTS

	<u>Page No.</u>
I INTRODUCTION	1
II. REVIEW	2
1. Steady-State Combustion Model/Hydrazine-NTO	2
2. Instability Model	10
3. Scaling	17
4. Droplet Atomization	27
5. Solid Particle Effects on Stability	34
III. PARAMETRIC STUDY OF COMBUSTION INSTABILITY	41
1. Steady-State Analysis	41
2. Stability Analysis	89
Experimental Correlation	96
Conclusions	101
IV. LIQUID PHASE MIXING AND REACTION	102
1. Liquid Phase Reaction	102
2. Liquid Phase Separation Potential	109
3. Characteristic Ignition Index	113
4. Conclusions	114
V. ATOMIZATION	115
1. Theoretical Development	116
2. Theoretical Distribution Function Compared to Experimental Data	120
3. Correlation of Atomization to Process Parameters	125
4. Conclusions	126
REFERENCES	127
DISTRIBUTION	129
Document Control Data Form DD 1473	138

NOMENCLATURE

A	combustor contraction ratio, A_c/A_t
A_c	cross-sectional area of combustor
A_p	amplitude of pressure disturbance
A_t	nozzle-throat area of combustor
A_v	amplitude of velocity disturbance
a	speed of sound in gases
C_p	specific heat at constant pressure
C_v	specific heat at constant volume
C^*	characteristic exhaust velocity
D_n	nozzle diameter
D_o	injection stream diameter
E	stream impingement energy
\bar{x}	local fuel fraction vaporized
$f(\gamma)$	function of gamma $\sqrt{\frac{2}{\gamma+1}} \frac{\gamma+1}{\gamma-1}$
g	acceleration due to gravity
I	momentum flux
I_n	instability index
J_H	mechanical equivalent
J	viscous-dissipation parameter
k	thermal conductivity
L	burning-rate parameter
M	molecular weight

m	burning rate of propellant, fraction/inch and mass of drop
Nu_h	Nusselt number, heat transfer
Nu_m	Nusselt number, mass transfer
n	number of drops/second in each drop size group and exponent
P	pressure
P_r	Prandtl number
ΔP	pressure difference
q	rate of heat transferred
R_{max}	liquid phase heat release with perfect mixing
R	universal gas constant
Re	Reynolds number
Re_d	Reynolds number of droplet based on the speed of sound
r	drop radius and radial direction
Δr	radial element thickness
r_{an}	radius of annular ring
r_t	decomposition flame radius
S	surface area
S_c	Schmidt number
T	temperature
\bar{T}	average film temperature $(T_g - T_l)/2$
t	time
U_l	internal energy of liquid
u	gas velocity
v	velocity and drop velocity

Δv	absolute value of velocity difference between gases and drops
Δv_z	absolute value of velocity difference between gases and drops in axial direction
\dot{W}	propellant flow rate
w	vaporization rate of single drop (lbm/sec)
x	axial position ($x=0$ at injector)
z	axial direction
Δz	axial element thickness
ϵ	correction factor for mass transfer
β	defined by
γ	specific-heat ratio
∇	del operator
η_{C^*}	efficiency based on characteristic velocity
θ	angular direction
λ	heat of vaporization and thermal conductivity of gases
μ	viscosity
ξ	defined by equation
ρ	density
T_{mix}	mixing time of impinging streams
τ	stress tensor
ϕ	mixture ratio, O/F
ψ	defined by equation
ω	local instantaneous burning rate (lbm/sec in ³)

Subscripts

a	vapor
c	combusted or combustion chamber
d	droplet
f	fuel
g	product gas
i	index of summation
j	at injector
l	liquid
m	vaporization mantle
o	oxidizer, stagnation, or steady-state
p	particle
s	stability quantity
v	vaporized

Superscripts

'	reduced parameter, defined in equation
-	average

I. INTRODUCTION

The work conducted under AF 04(611)-10542 has been directed toward developing methods for designing stable rocket engines. The various areas investigated during this program are:

- 1) A steady-state combustion model for hydrazine type propellants.
- 2) A combustion instability model.
- 3) A scaling criteria for stable engines.
- 4) An experimental program to verify the developed scaling criteria.
- 5) A survey of atomization literature.
- 6) An experimental program to determine the influence of propellant properties and hydraulic parameters on atomization.
- 7) An analysis of the effects of solid particles on damping combustion instability in gelled propellants.
- 8) A parametric study of injector and engine parameters on stability of a Transtage type engine.
- 9) A study to determine the effects of liquid phase reactions on atomization and combustion of hypergolic propellants.
- 10) A correlation and prediction of droplet size from an impact energy method by minimizing surface energy.

Items (1) and (2), i.e., the development of the steady-state and combustion instability models, their application to predict instability zones and listings of the developed computer programs are reported in the Special Report (Ref.1) and reviewed in Section II., Items (3) to (7) were reported in the Semiannual Report (Ref.2) and pertinent results are also summarized in Section II. In Sections III, IV, and V, Items (8), (9), and (10) will be covered respectively. Thus, this report will concentrate on the results of a parametric study on combustion instability in a Transtage type engine, the effects of liquid phase reactions on atomization and combustion, and a method of predicting droplet size from an impact energy method by minimizing surface energy.

II. REVIEW

This section will review the work conducted on the subject contract and reported in detail in the Special and Semiannual Report (Refs. 1 and 2). This section will discuss: 1) development of the steady-state model; 2) development of a combustion instability model; 3) criteria for scaling and an experimental program to verify these criteria 4) an atomization literature review and an outline of an experimental program to determine the influences of propellant parameters and triplet injector geometries on droplet size; and 5) an analysis of the effects of solid particles on damping combustion instability in gelled propellants.

1. Steady-State Combustion Model/Hydrazine-NTO

Analysis of high frequency combustion instability requires complete spatial knowledge of such parameters as vaporization rate, relative velocity, and droplet Reynolds number. To determine these parameters, a detailed steady-state combustion model was developed for decomposing type propellants and additional information was determined on hydrazine droplet combustion, atomization and liquid phase reactions. To develop a hydrazine combustion model, experiments were conducted which indicated that a single diffusion flame front model, as shown in Figure 1, is not realistic and two-flame fronts appear in the combustion of MMH and hydrazine in nitrogen tetroxide, as shown in Figures 2 and 3. It has been shown that existence of "two flames" depends on the convective environment and the hydrazine decomposition kinetics. The two-regime model of the decomposition front position is shown in Figure 4. In regime I the laminar diffusion mantle thickness B is larger than the distance required for decomposition (X^*) and two flames occur simultaneously, i.e., an outer oxidation flame with an inner decomposition flame. Regime II is the same as the laminar diffusion model shown in Figure 1. Here the film thickness is thinner than the distance required for the hydrazine to decompose and a single flame exists. Profiles of combustion rate and film thickness along the combustion chamber length are shown in Figure 5. When the propellant is injected into the combustion chamber it is traveling at approximately the injection velocity, while the axial velocity of the combustion gases is approximately zero. As combustion takes place the gas velocity increases, while

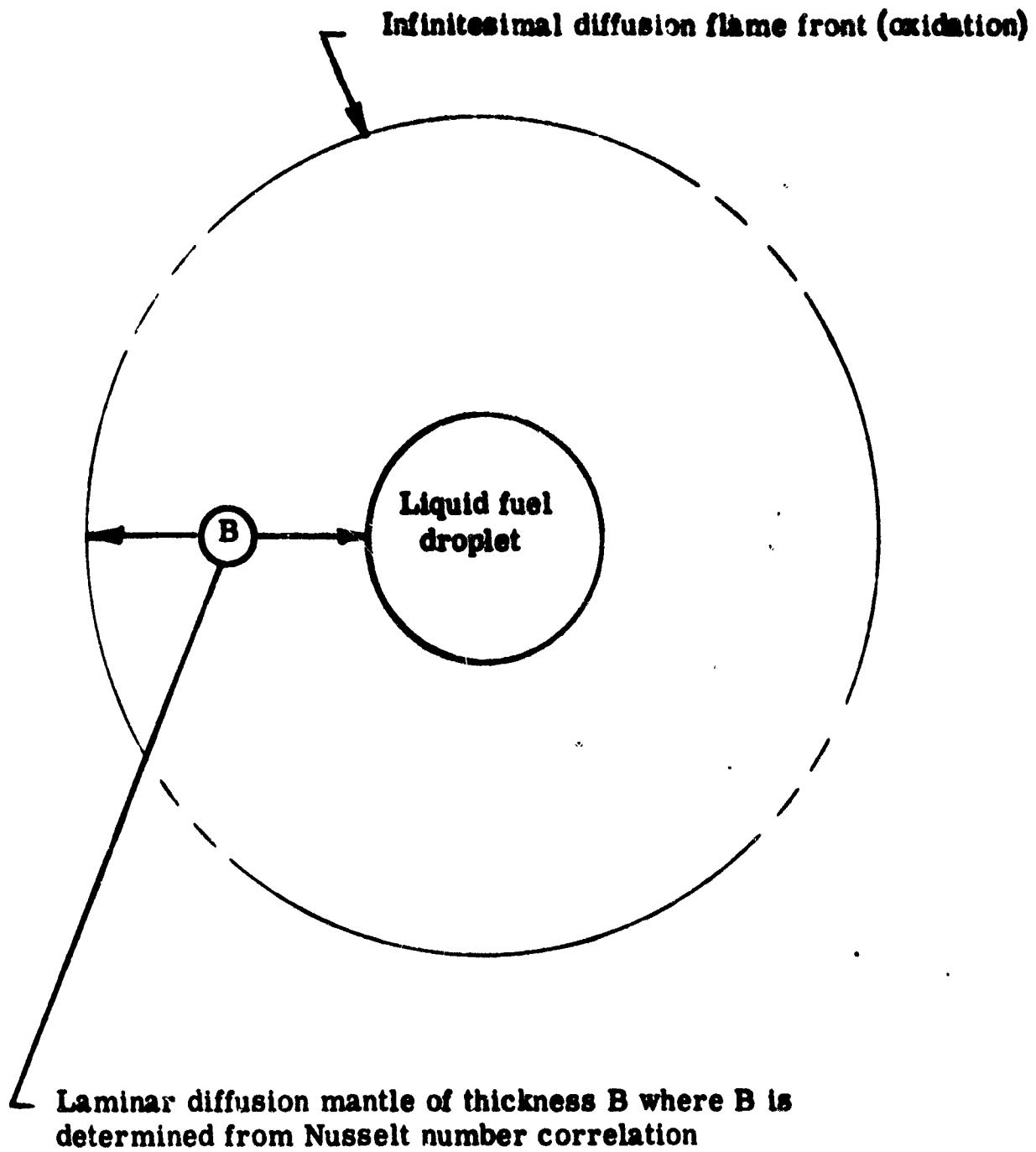


FIGURE 1. LAMINAR DIFFUSION MODEL, SINGLE FLAME FRONT



**Note: The liquid
drop is within the
wire support.**

**MMH Burning in still nitrogen
tetroxide, at one atmosphere**

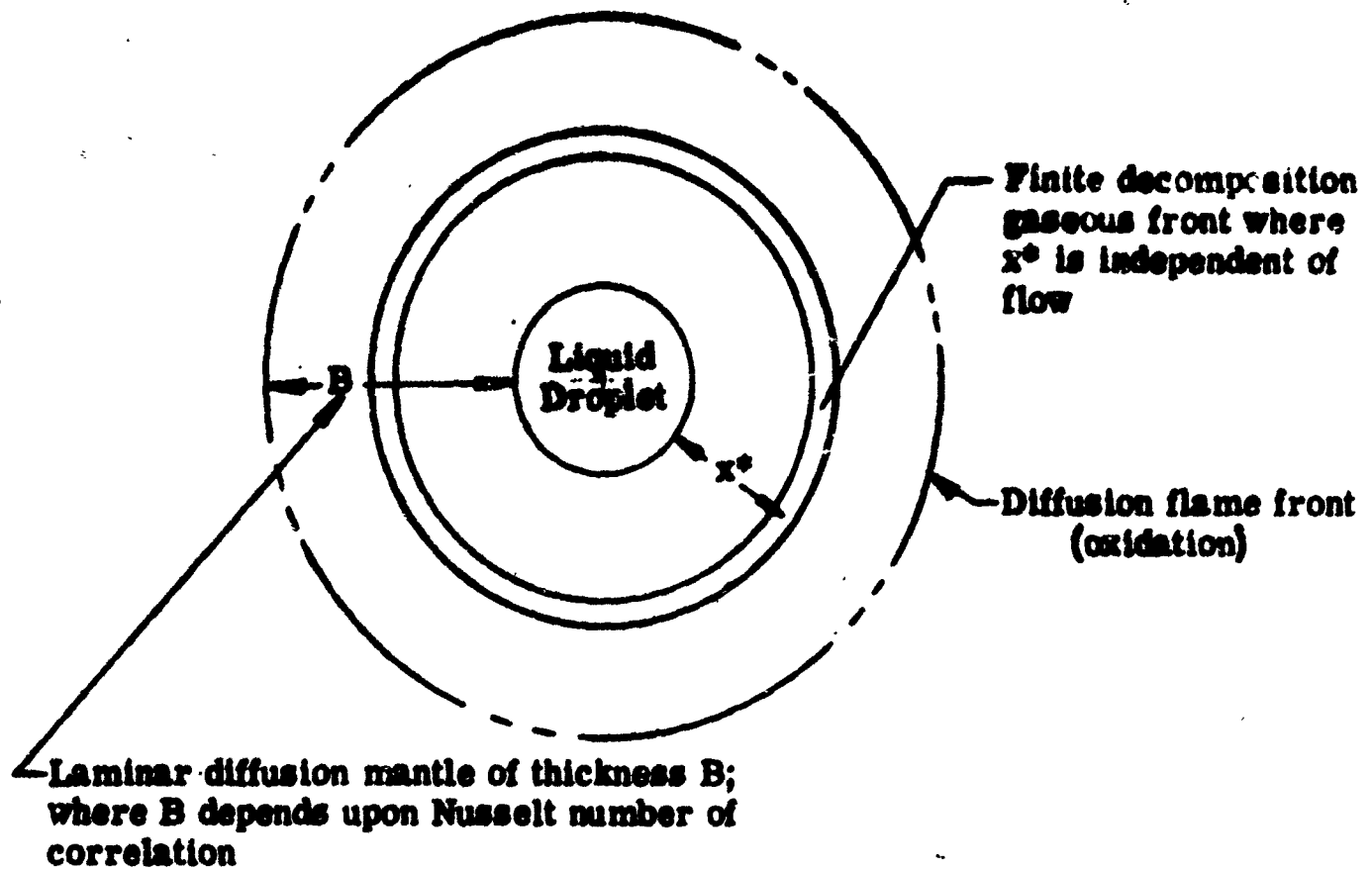
**FIGURE 2. PHOTOGRAPH OF EXPERIMENTAL BURNING
DROP SHOWING TWO FLAME FRONTS**



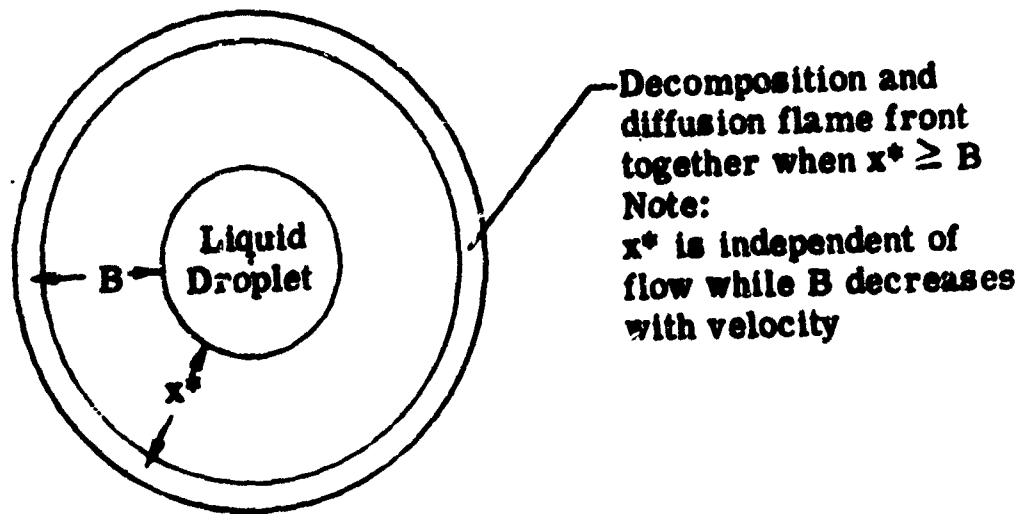
Note: The liquid drop is within the wire support.

Hydrazine burning in still nitrogen tetroxide, at one atmosphere

FIGURE 3. PHOTOGRAPH OF EXPERIMENTAL BURNING DROP SHOWING TWO FLAME FRONTS



DECOMPOSITION FRONT WITHIN DIFFUSION MANTLE, REGIME I



LAMINAR DIFFUSION MODEL WHEN $x^* \geq B$, REGIME II (This is the same as Figure 1)

FIGURE 4. TWO-REGIME MODEL OF DECOMPOSITION FRONT POSITION

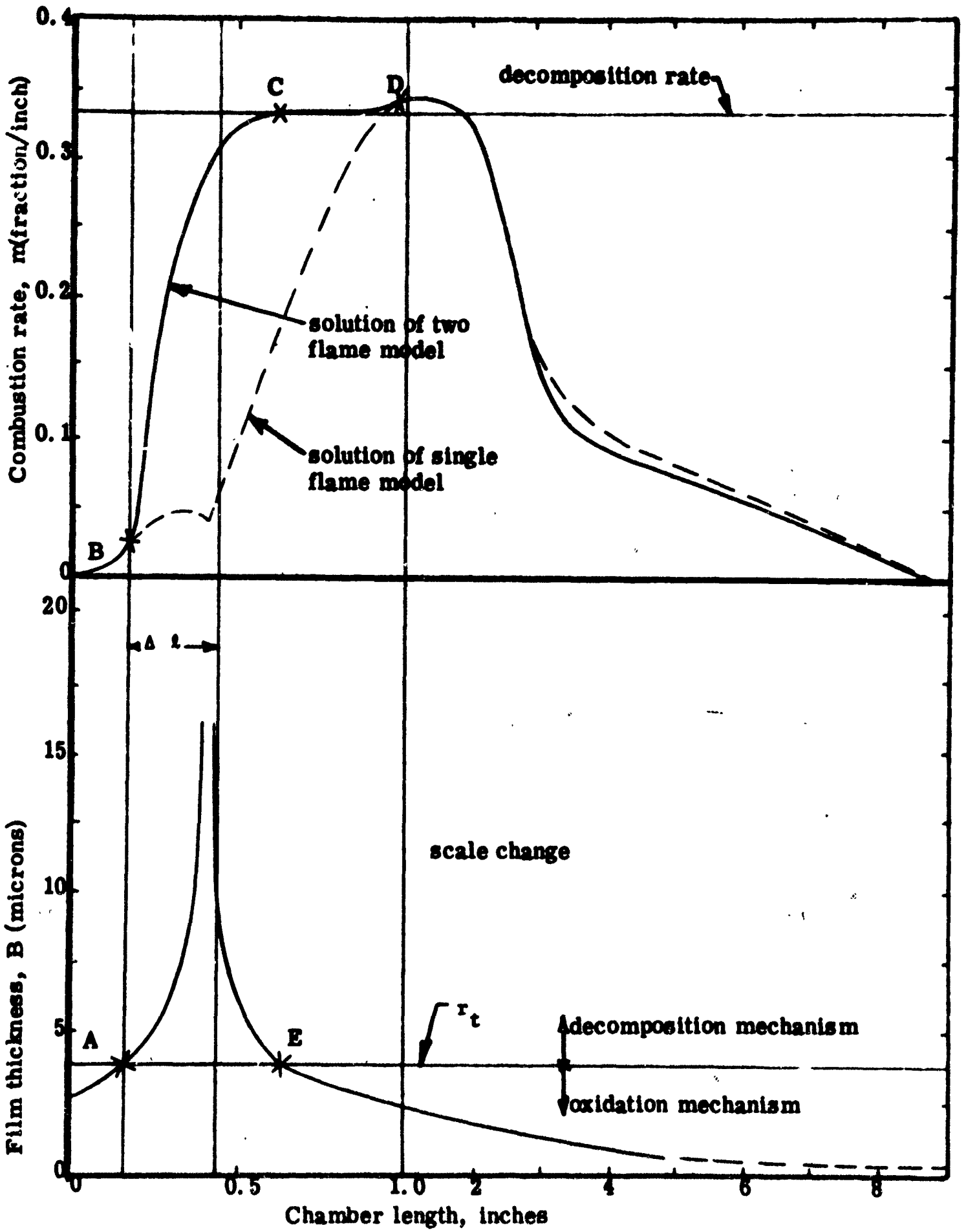
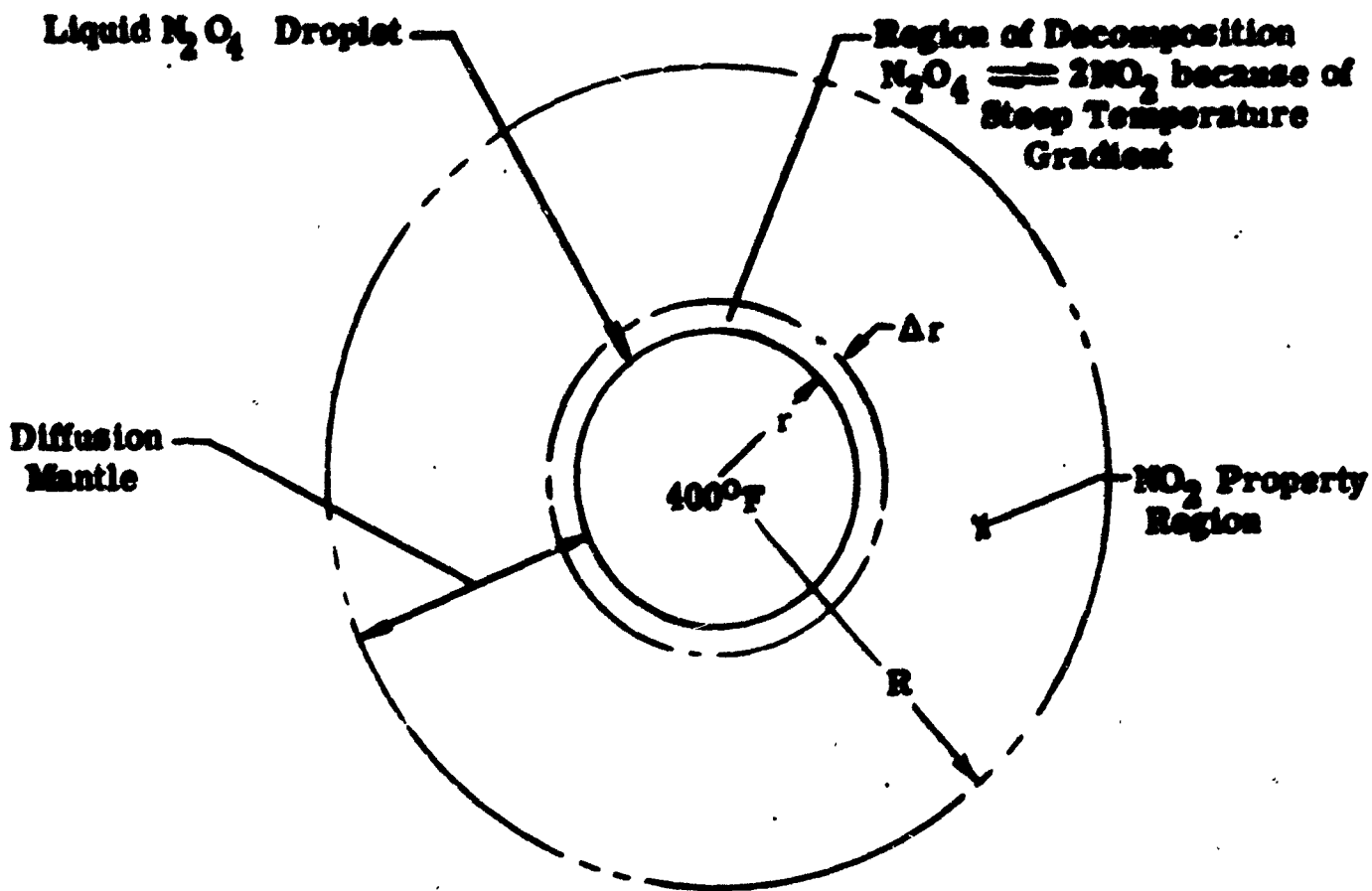


FIGURE 5. Combustion Rate, Initial Drop Size 49.4 μ

the liquid decelerates, until the gas and liquid are traveling at the same velocity. As combustion proceeds, the gas velocity increases further, with the liquid accelerating toward the gas velocity. The convective film thickness varies inversely to the relative velocity between the gases and liquid. From Figure 5 it is shown that when the propellant is first injected into the chamber the film thickness is less than the decomposition thickness because of the high relative velocity and the droplets are burning in regime II. The gas-liquid relative velocity decreases to point A, where the oxidation and decomposition are the same. Up to this point the combustion rate follows the single flame model solution as shown at point B. As the relative velocity is further decreased, the film thickness grows larger than the decomposition thickness and the regime I controls the combustion process. The increased rate of the "two-flame" model occurs at point C. After the relative velocity reaches a minimum, the gas passes the droplets and the film thickness decreases to point E, where the droplets re-enter regime I. The burning rate remains relatively constant between C and D since the droplets have heated to their wet-bulb point. The integrated result of the increased combustion rate is that the fraction of propellant combusted near the injector face is higher than would occur with propellant under the same conditions, without decomposition.

To compute steady-state combustion profiles a detailed knowledge of the vaporization rate of N_2O_4 is also required. As shown in Figure 6, the entering oxidizer droplet is assumed to be N_2O_4 . However, as the N_2O_4 evaporates it goes to approximately 50% NO_2 . Then, since the temperature gradient is very steep, (Figure 6) the vapor will be 100% NO_2 before it crosses even 10% of the diffusion mantle. The approximation that NO_2 is the vaporizing species was thus made. Using this approximation it was possible to account for chemical change by adding the heat of decomposition to the heat of vaporization for N_2O_4 . Since this reaction is endothermic the effective heat of vaporization is increased and the vaporization rate is slower than that predicted when decomposition is not taken into account.

A propellant vaporization model developed by Priem and Heidmann (Ref. 3) was used to compare calculated and experimental combustion efficiencies for a



The assumption making possible the inclusion of heat of reaction with heat of vaporization is

$$\Delta r < 10\% \text{ of } (R - r).$$

DROPLET VAPORIZATION MODEL

FIGURE 6.

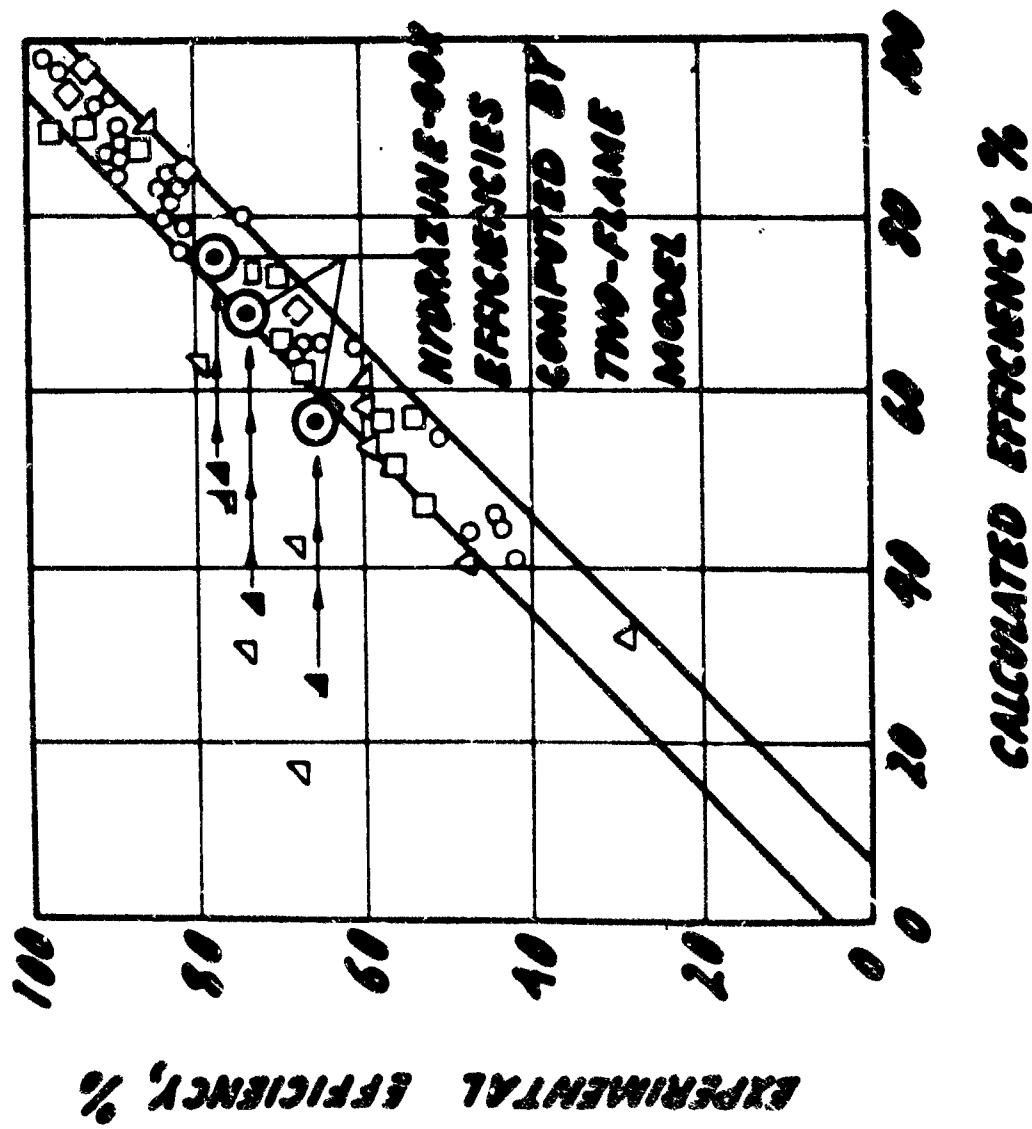
large number of propellant combinations. (Shown in Figure 7). While excellent agreement was obtained with many propellants, hydrazine efficiencies were always calculated lower than measured. Using the hydrazine "two-flame" decomposition model, combustion efficiencies for hydrazine and gaseous oxygen were recomputed as shown in Figure 7. The results showed that the decomposition model predicted a more accurate and higher combustion rate than the single flame model used by Priem and Heidmann (Ref. 3), correlating the data. It was also shown that the maximum effect occurred for shorter chamber lengths, agreeing with the decomposition model which showed the increase in combustion near the injector face at the minimum relative velocity region.

To obtain a complete spatial knowledge of vaporization rate, relative velocity and droplet Reynolds number the steady-state vaporization model with a vapor phase decomposition flame was programmed and solved on a Control Data 3400 digital computer. Computer solutions are being used in parametric studies to determine the effect of physical properties and design parameters upon combustion. The computer model treats decomposition both in the nitrogen tetroxide and hydrazine system. The program can compute vaporization of a bipropellant system, thus enabling a realistic prediction of chamber parameters.

2. Instability Model

Dynamic Science Corporation has developed a nonlinear model for determining the zones of a liquid rocket engine in which a tangential mode of high frequency instability is most easily initiated. This model has been related to hardware design parameters, i.e., parameters related to injector design, chamber configuration, and propellants, thereby enabling the influences of system design and stability rating devices to be determined.

Combustion instability zones in a liquid rocket engine are determined by combining a nonlinear instability model with a steady-state vaporization program. The instability model considers the nonlinear conservation equations with mass addition using a steady-state expression for the burning rate. This model applies to a one-dimensional annulus of small length (Δz) and



- PROPELLANT** **INJECTOR**
- NEPTANE-OXYGEN
 - IMPINGING JETS
 - △ TRIPLET
 - PARALLEL JETS
 - NEPTANE, LIQUID OXYGEN, GASEOUS OXYGEN
 - AMMONIA, LIQUID OXYGEN, GASEOUS OXYGEN, FLUORINE
 - ◇ HYDROGEN, LIQUID OXYGEN, FLUORINE
 - △ JP-4, LIQUID OXYGEN
 - △ HYDRAZINE, LIQUID OXYGEN, GASEOUS OXYGEN, FLUORINE

FIGURE 7.

thickness (Δr) shown in Figure 8. Applying the results of this model, as shown in Figure 9, a rocket engine can be analyzed by incrementally dividing the combustion chamber into annular nodes in the r and z directions. Steady-state properties at each annular node or position in the chamber are computed from a steady-state vaporization program described in Paragraph 1. These steady-state properties, i.e., vaporization rate, relative velocity, and droplet Reynolds number, and the curves from the instability model (Figure 9) are used to determine the stability of the node. This process is repeated for each node to determine a stability map of the entire engine, as shown in Figure 10.

From a nonlinear model important nonlinear phenomena are predicted, i.e., (1) stability dependence on disturbance wave shape, amplitude, type (velocity or pressure), and position; (2) the limiting amplitude of the unstable pressure oscillations; and (3) the shape of the unstable wave forms. Major results of this analysis show that the amplitude and position of a pressure disturbance required to initiate instability can be determined, thereby defining a sensitive zone (and the best place to disturb the engine). This sensitive zone extends several inches from the injector face and occurs where the average droplets are moving the slowest relative to the gases.

Dynamic Science Corporation has shown that an annular combustor section will be more stable as the droplet Reynolds number approaches zero. Thus, a significant result of this work is that there are, for a vaporization controlled combustion process, three parameters affecting stability:

- (a) Burning rate parameter - L
- (b) Absolute value of relative velocity - Δv
- (c) Reynolds number of drop based on speed of sound - Re_d .

Such information is not only of use from the preliminary design standpoint, but also as an invaluable tool in understanding how rocket engines should be disturbed during their development test programs to determine the degree of stability of an engine. The

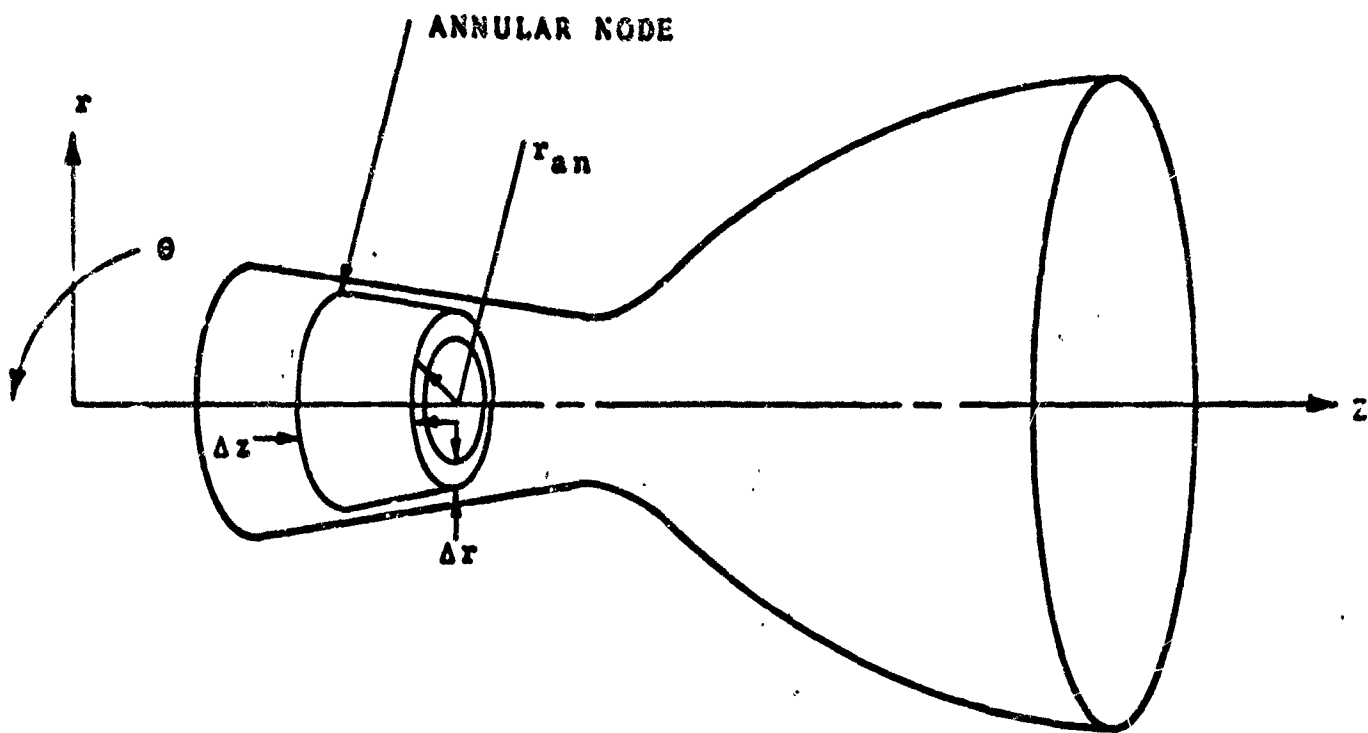


FIGURE 8. Transtage Rocket Engine Model

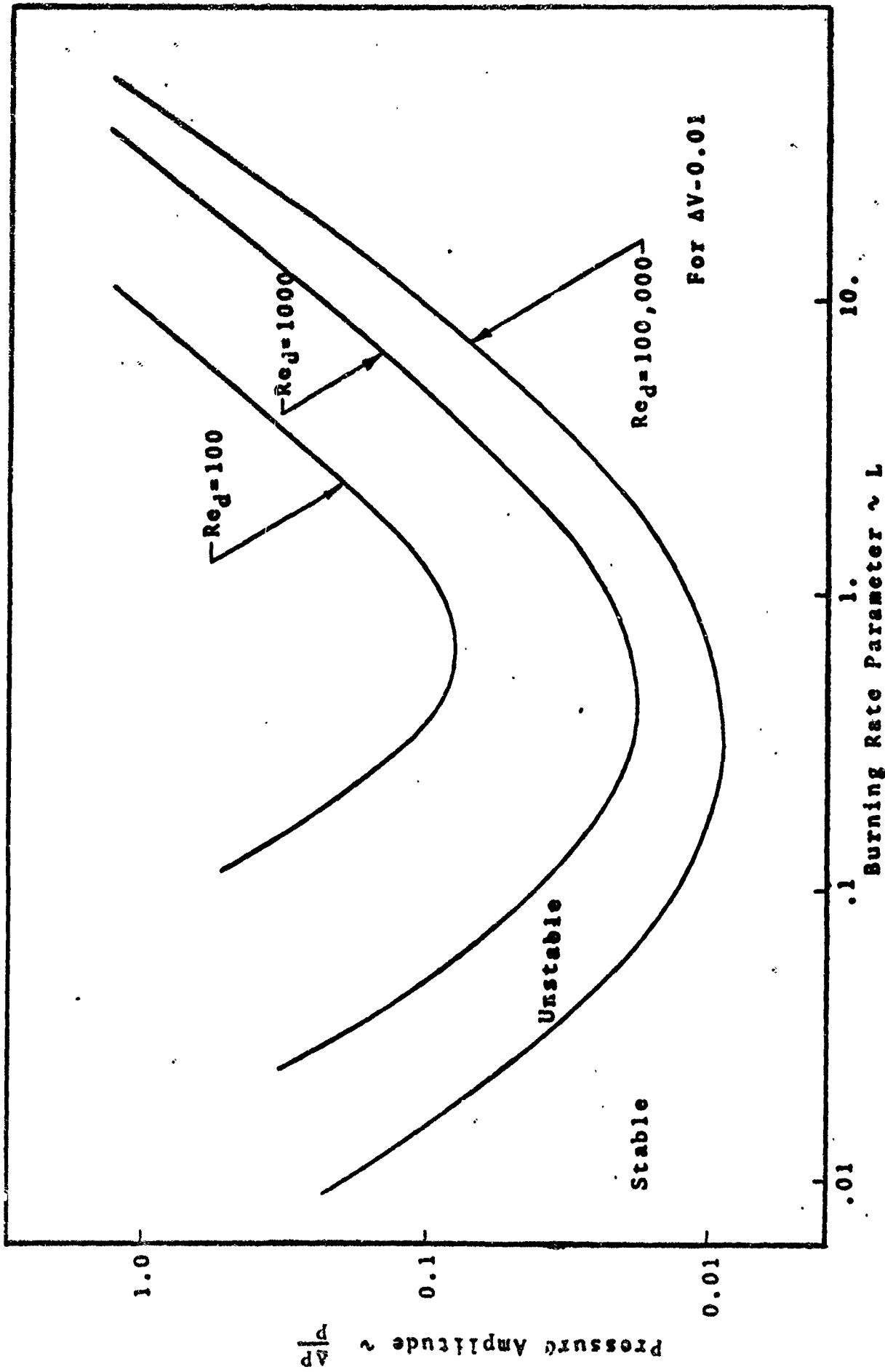


FIGURE 9. Stability Limit Curve

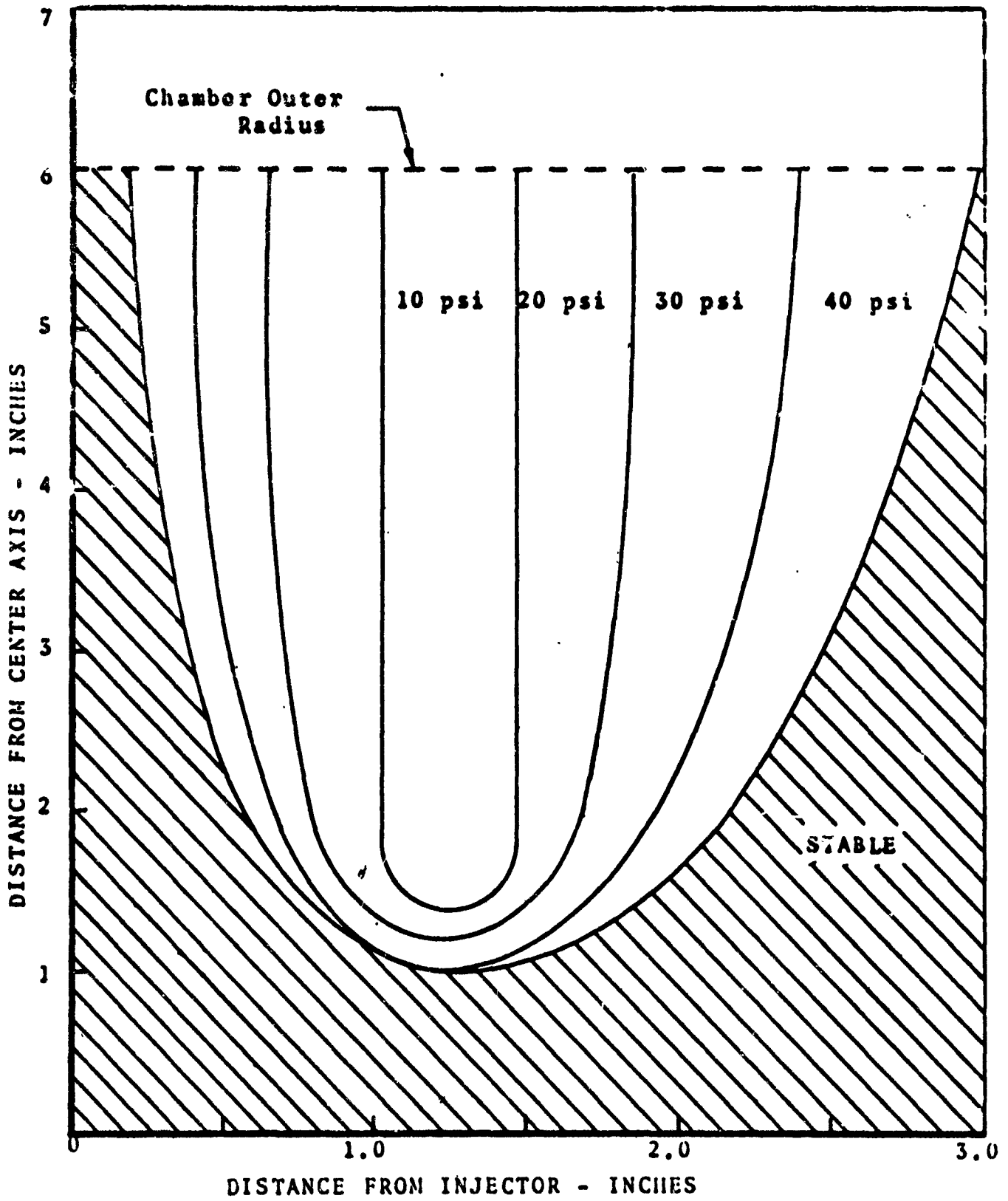


FIGURE 10. Pulse Pressure Contour Lines Defining Unstable Zones

Dynamic Science Corporation model enables the engine designer to determine the position to introduce the disturbance, a reasonable disturbance amplitude criteria, and the most effective wave profile (pressure and/or velocity disturbance). Since the injector design variables can be related to threshold disturbance amplitude, parameters can be modified to increase stability of a given engine configuration or be used in the preliminary design of an engine.

3. Scaling.

Design and scaling criteria for stable liquid rocket engines were developed using a nonlinear combustion instability model with a droplet vaporization model. The scaling parameters were formed into an "Instability Number" which was used to correlate approximately 60 runs conducted by the USAF RPL and Aerojet.

Result of the nonlinear instability showed that three parameters define the shape of a sensitive instability zone: (1) burning rate parameter; (2) Reynolds number of the droplets based on the speed of sound; and (3) relative velocity between the gas and droplets. The study further showed that a liquid rocket engine is most sensitive when the gas-droplet relative velocity is a minimum or zero. Thus, in developing a scaling parameter for the tangential mode of high frequency, one of the three important parameters can be eliminated and only the burning rate parameter (L) and (Re_d) Reynolds number of droplet, need be considered at $\Delta V=0$. If two engines have the same L and Re_d at $\Delta V=0$, they will have the same stability, that is, the same minimum threshold disturbance required to trigger instability.

For most injectors built, the most sensitive region is at the outer radius of the engine. Therefore, if there is a small diameter low-thrust high-performance engine utilizing a given propellant, and a larger thrust engine with the same stability characteristics is required, scaling the burning rate parameter and Reynolds number of the droplet at the outer radius on the $\Delta V=0$ plane will insure the same stability characteristics (for $L < 2$). However, since the injector variables will be changed in this scaling process, length as well as diameter must be scaled to retain η_{C^*} . As shown in Figure 11, scaling from a model engine (1) to a full-size engine (2) required ($\Delta V=0$ and $L < 2$):

$$Re_{d1} \geq Re_{d2}$$

$$L_1 \geq L_2$$

By scaling with conditions (II-1) and (II-2) the full-size engine has equal or greater stability, i.e., an equal or greater disturbance required to trigger instability. By assuming that the propellant and mixture ratio are retained in the scale engine L and Re_d may be related to engine parameters by

$$\frac{Re_{d2}}{Re_{d1}} \approx \frac{r_2 P_2}{r_1 P_1} < 1$$

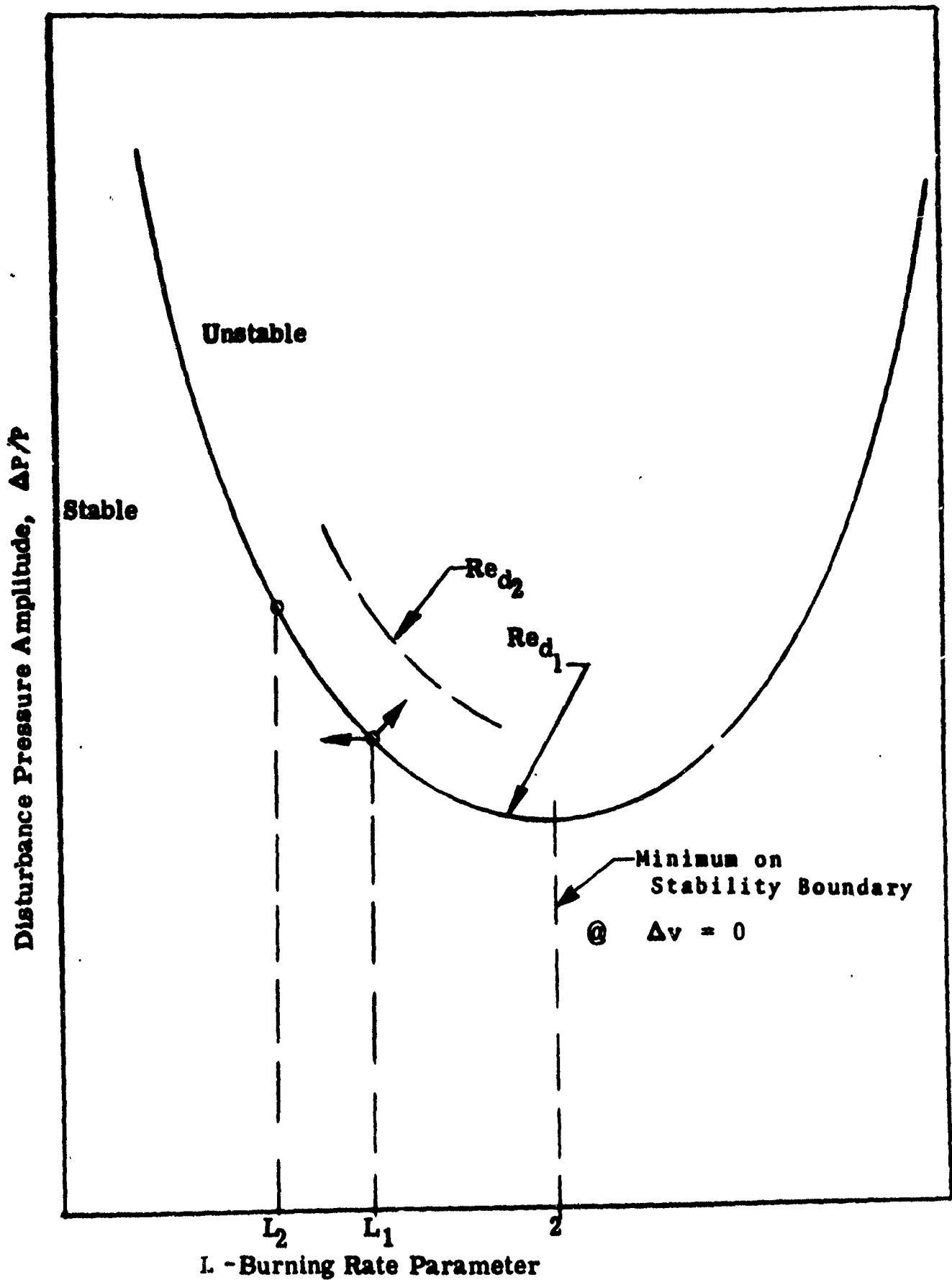


FIGURE 11. STABILITY LIMIT CURVE

$$\frac{L_2}{L_1} \propto \frac{r_{a1} P_1 \dot{W}_2 V_{j1} r_1^2}{r_{a2} P_2 \dot{W}_1 V_{j2} r_2^2} \leq 1$$

These criteria are shown in Figure 12. For conditions II-1 and II-2 to be fulfilled the ratios must fall inside the box. To combine these two groups a functional relationship is required between L , Re_d and $\Delta P/P$ such that:

$$\frac{\Delta P}{P} = f(Re_d, L)$$

For $L < 2$, such a relationship can be approximated by curve fitting the computed stability limit curves, with an expression of the form:

$$\frac{\Delta P}{P} \propto \frac{1}{L Re_d^n} \text{ where } n=1 \text{ to } 3$$

Lines 1 and 2 of Figure 12 represent locus of solutions for $n=1$ and 3 respectively. The conditions II-1 and II-2 guarantees ($L < 2$):

- a. The engine is more stable than the scale if

$$\frac{L_2}{L_1} < 1 ; \frac{Re_{d2}}{Re_{d1}} < 1$$

- b. The engine is as stable as the scale if

$$\frac{L_2}{L_1} = 1 ; \frac{Re_{d2}}{Re_{d1}} = 1$$

- c. The engine is less stable than the scale if

$$\frac{L_2}{L_1} > 1 ; \frac{Re_{d2}}{Re_{d1}} > 1$$

To facilitate experimental correlation, L and Re_d are formed into an "instability number." Engines with the same instability number will have the same stability, i.e., they will be triggered unstable to the same $\Delta P/P$ pulse. As presented in Reference 2, two instability numbers are formed from the product of Reynolds number of the droplet and burning rate parameter.

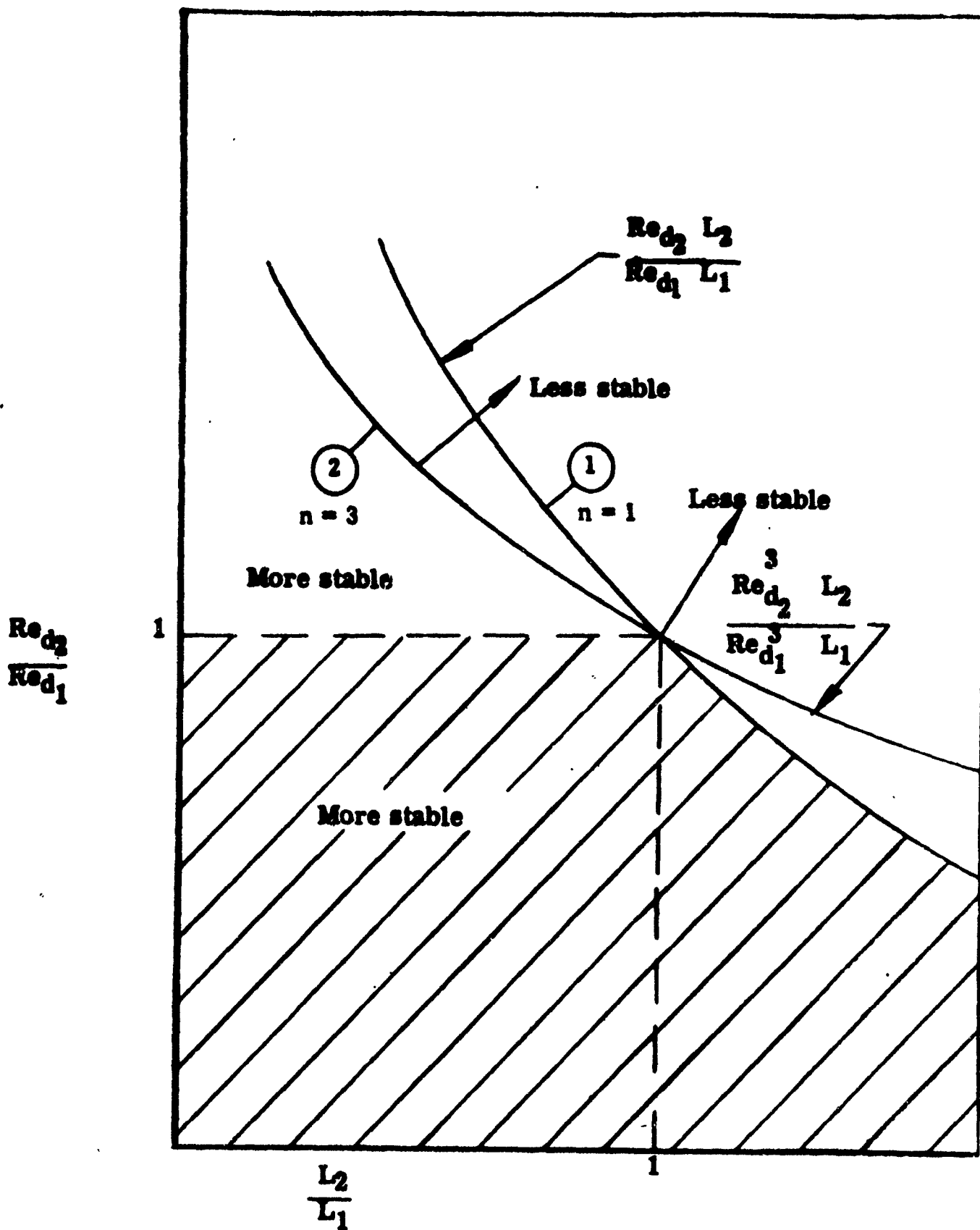


FIGURE .12. STABILITY PARAMETERS ($L < 2$)

$$I_n \propto \frac{P D_n^2 D^{1/6}}{V_f}$$

and

$$I_n \propto \frac{W_f^{(s+1)} E^{1/6}}{V_f}$$

Where E is the summation of the impact energy which the streams exert normal to each other. This term is an attempt to relate stream geometry and velocity to drop radius.

These "instability numbers" are used to correlate engine tests as shown in Figures 13-17. In addition to the MMH tests conducted at USAF-RPL, this relation correlated 57 out of 61 tests with pulse motors at Aerojet* using:

- a. MON-10 and U-DETA
- b. N_2O_4 and N_2H_4
- c. IRFNA and UDMH

Figures 13-15 show the usual stability decreasing with increasing I_n ; however at a certain value of I_n the trend reverses itself corresponding to moving to the $L > 2$ side of the stability curves. Pulse strengths from the RPL data are lower because they are measured in a rocket engine, while the Aerojet* data was measured in a shock tube. The Aerojet data does not compare quantitatively with the RPL data due to difference in measurements, however the trends are the same.

In conclusion, a set of scaling criteria have been developed which enable retaining scale stability when building a larger engine or changing operation conditions. An instability index or number is being derived which enable rating engines in order of stability. Several semi-analytical expressions, based on the product of Re_d and L were successful in the correlation of the experimental data however, more work has to be done before a complete understanding of the stability number can be obtained.

* Gray, P.D., and Krieg, H.C. "Pulse-Motor Evaluation of Injector-Pattern Combustion Stability with Storable Propellants, Aerojet Special Report for USAF-RPL, Confidential, AD-318667, 29 July 1960.

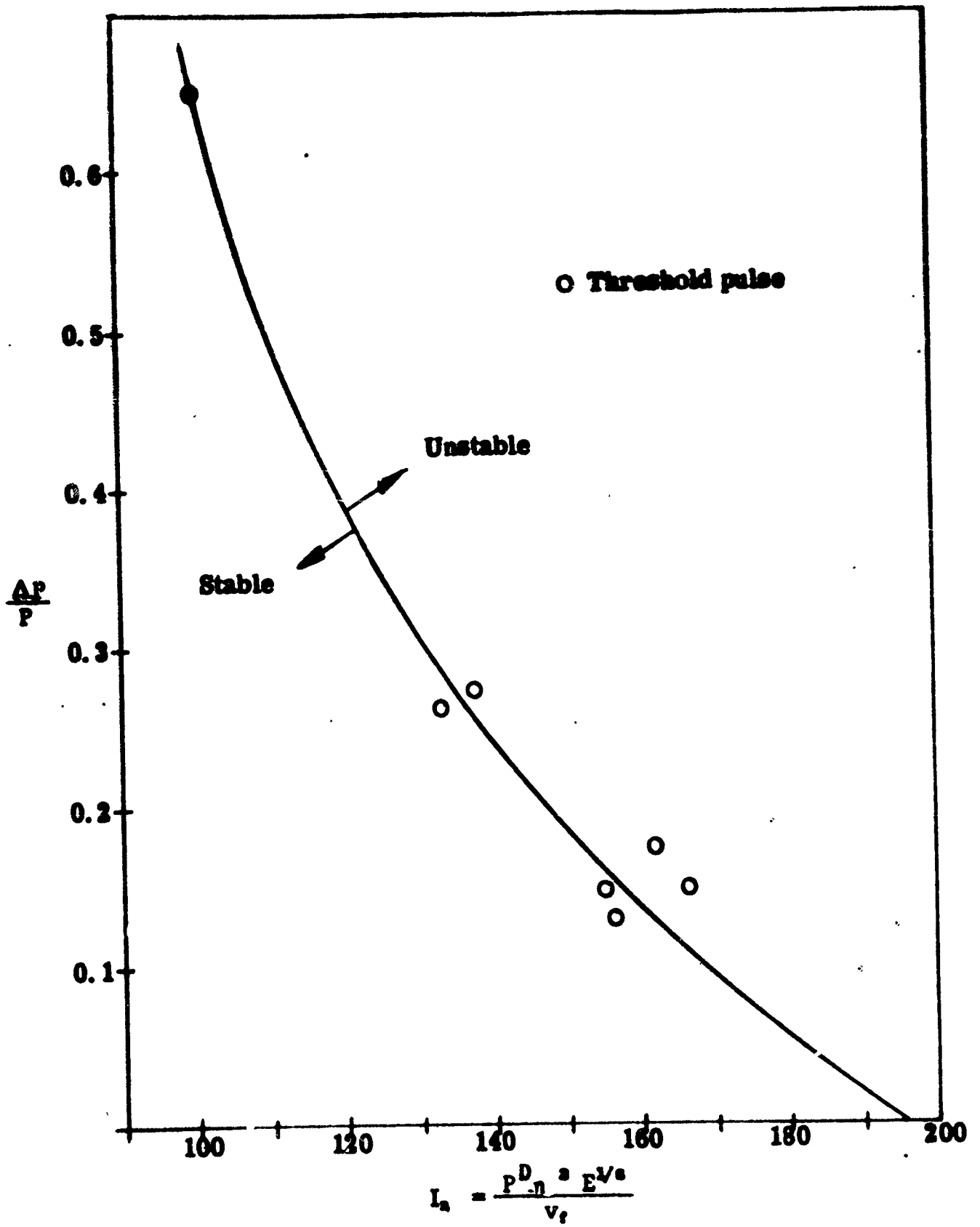


FIGURE 13. Instability Number Correlation for MMH/NTO Tests Performed by U.S. Air Force Rocket Propulsion Laboratory

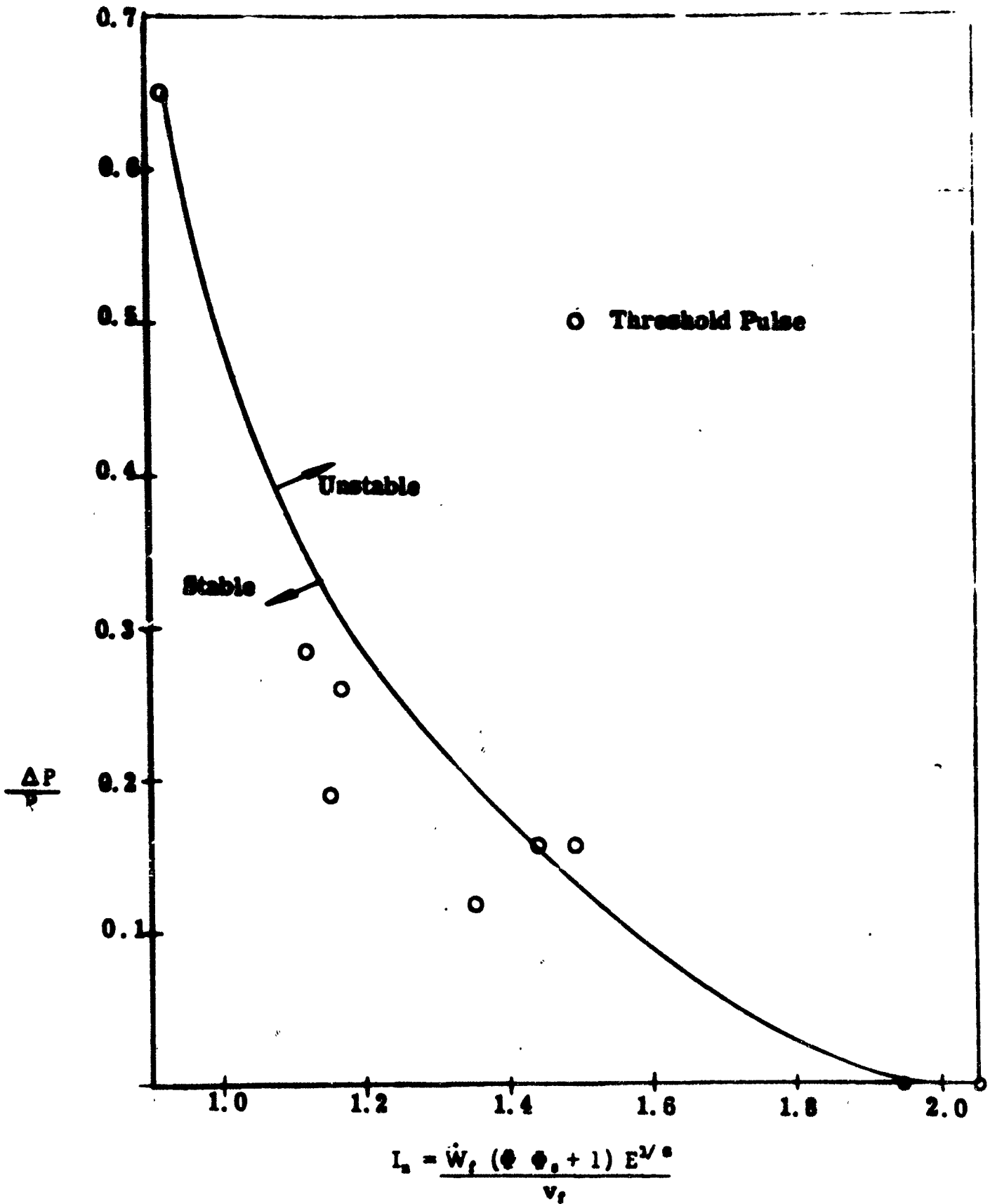


FIGURE 14. Instability Number Correlation for MMH/NTO Tests Performed by U.S. Air Force Rocket Propulsion Lab.

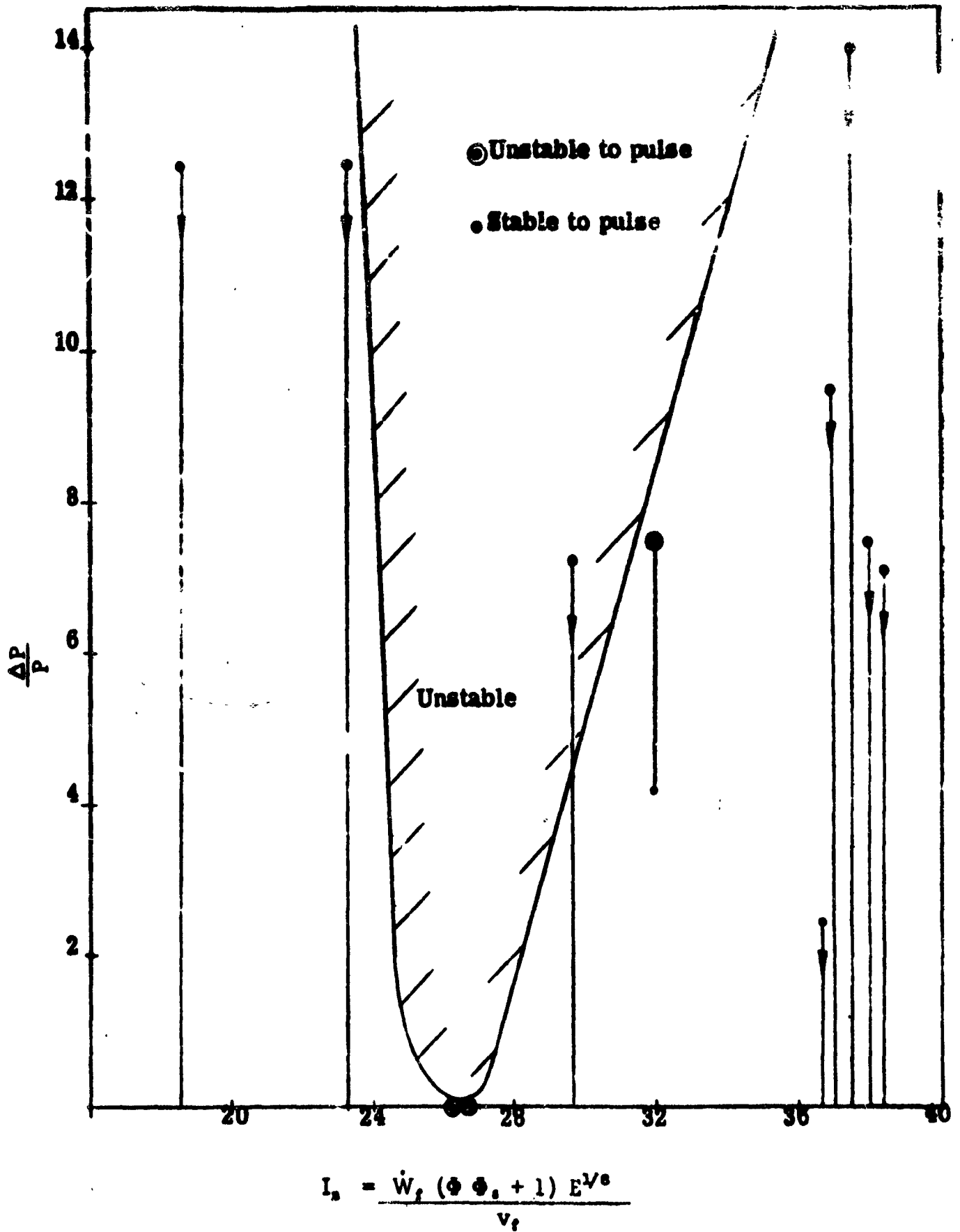


FIGURE 15. Instability Number Correlation for MON-10 and U-DETA Tests Performed by Aerojet.

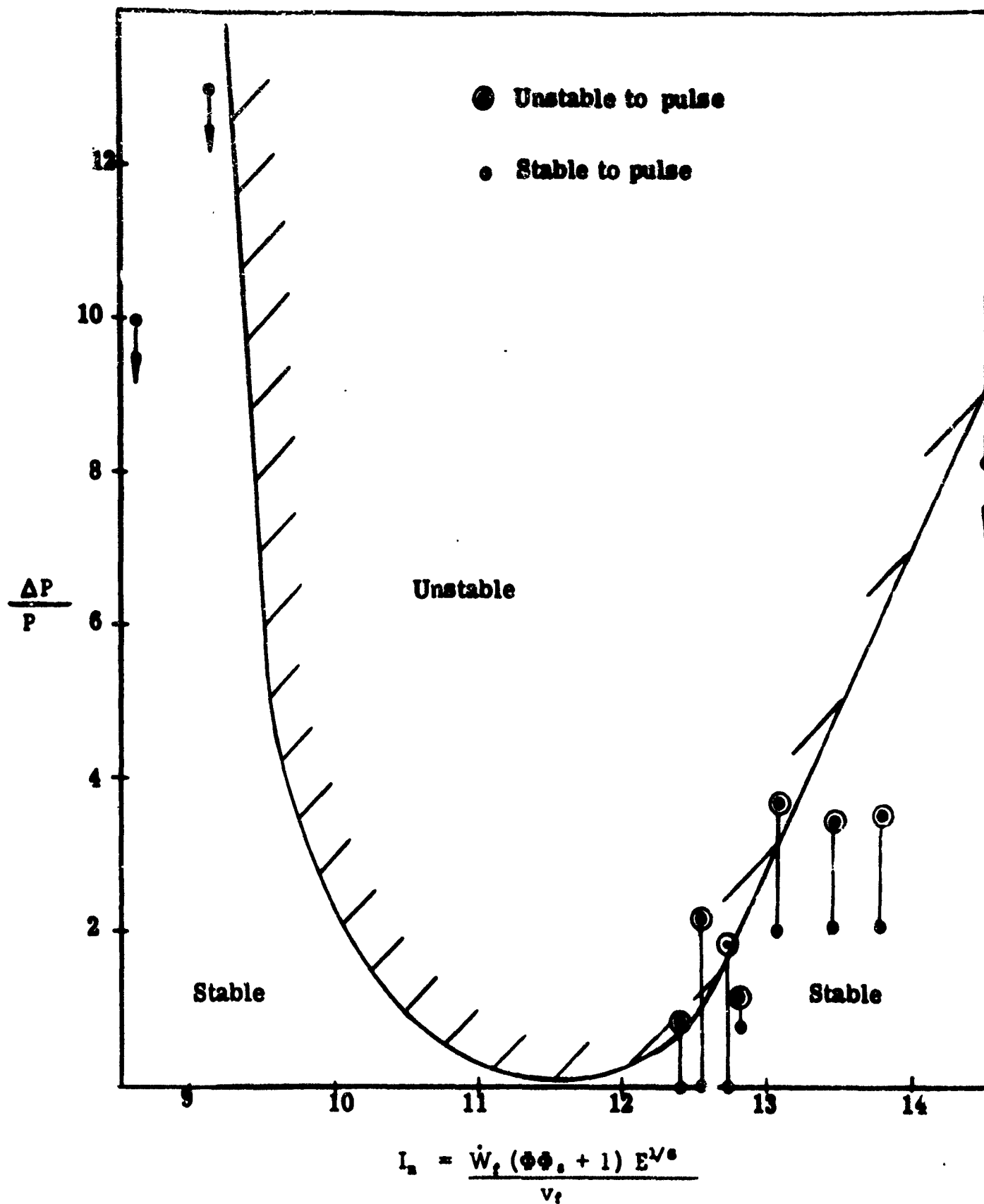


FIGURE 16. Instability Number Correlation for N_2O_4/N_2H_4 Tests Performed by Aerojet.

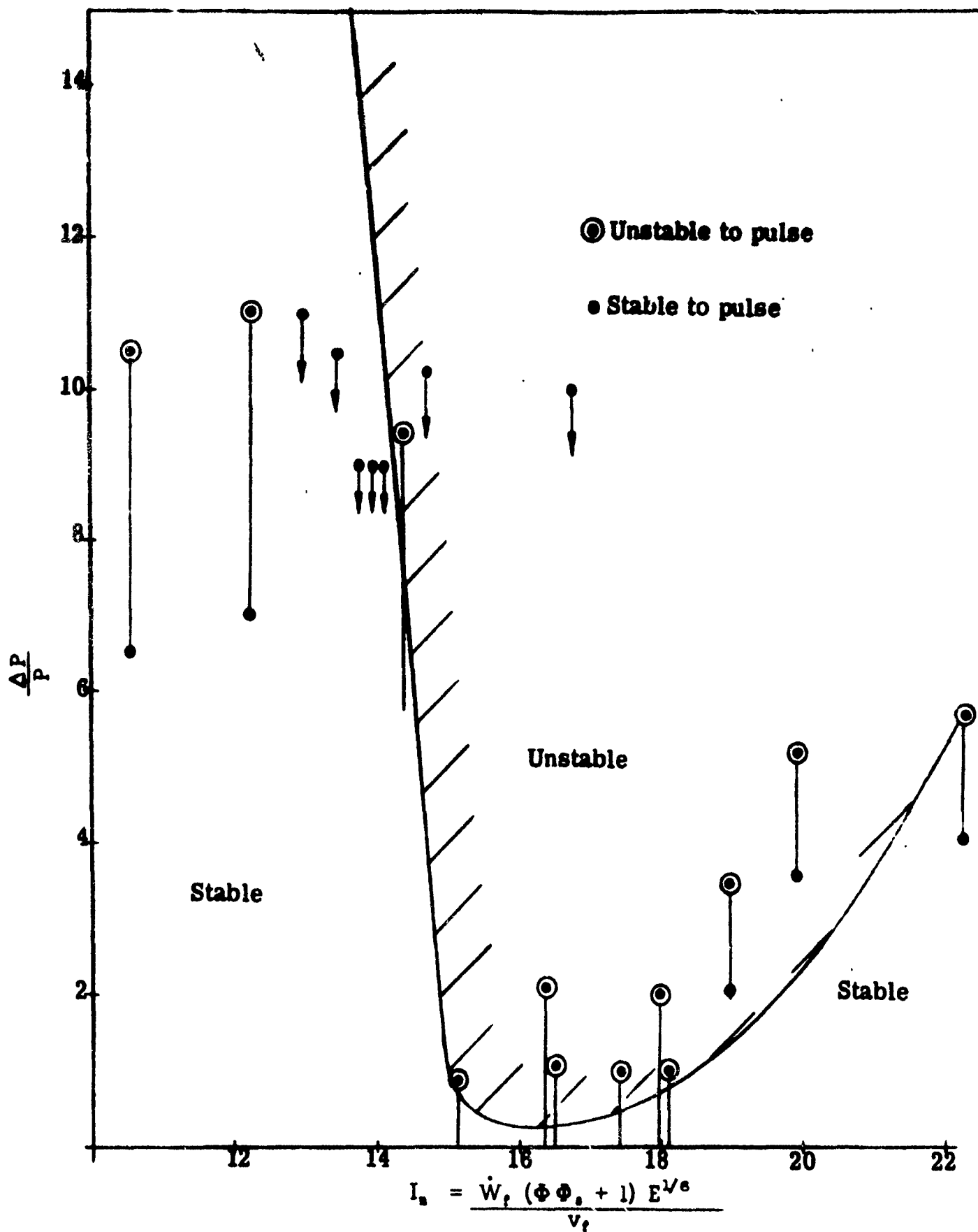


Figure 17. Instability Number Correlation for N_2O_4/N_2H_4 Tests Performed by Aerojet.

4. Droplet Atomization.

Numerous experiments directed toward the specification of size distribution of liquid droplets after atomization have been reported in the literature. Statistical distribution functions have been developed empirically by fitting experimental data. Spray distribution has been related to both physical properties and injector design variables; however, it is not possible to completely predict a realistic distribution and determine its statistical parameters based on given propellant properties and injector design.

Actual drop distributions are not uniform across the chamber but have three-dimensional spatial characteristics. The velocity of droplets is also distributed over a velocity range. The initial droplet velocity is as important as the initial size. However, information concerning droplet velocity distribution is current not available.

The distribution of droplets varies with the mechanisms of atomization. Two generalized categories may be used to describe the wide range of liquid atomization element designs. These are plain-jet injectors, and sheet atomizers. The most commonly used rocket injector, the impinging jet, combines the characteristics of the sheet and plain-jet injectors. Heidmann and Foster (Ref.4) and Bittker (Ref.5) have suggested that the impinging-jet injector produces a bimodal distribution of particles, this being consistent with the hybrid nature of the impinging-jet atomization mechanisms.

Many statistical distribution functions have been empirically fitted to experimental spray data. Bevans (Ref. 6) has examined the three most commonly used distribution functions, the Nukiyama-Tanasawa, Rosin-Rammler, and logarithmico-normal and concluded that the Rosin-Rammler expression was most successful at expressing experimental data from a pressure-atomized oil spray. However, Ingebo (Ref. 7, 8, and 9) has consistently obtained good results in fitting his excellent experimental work to a Nukiyama-Tanasawa distribution. Priem and Heidmann (Ref. 3) state that, "No criterion has been established for choosing the preferred distribution function. For convenience, therefore, the logarithmicnormal distribution function was used in this investigation...." General mathematical forms of these three distributions are:

Rosin-Rammler:

$$R = \exp(-4/r_m)^{a_R}$$

where R is the mass fraction of drops larger than r
and r_m and a_R are constants which determine the median size and dispersion of the droplets.

Logarithmico-normal:

$$\frac{dR}{dr} = \frac{a_L}{r} \exp\left\{-\frac{1}{2} \left[\frac{\ln(r/r_m)}{\ln \sigma_g}\right]^2\right\}$$

where R is the mass fraction of drops larger than r ,
and a_L is an empirical constant
while r_m and σ_g are the mass median drop radius and the standard deviation.

Nukiyama-Tanasawa:

$$\frac{dR}{dr} = \frac{a_N^6}{7.5} r^5 e^{-2a_N r}$$

where a_N is an empirical constant.

The values of the empirical constants shown in the above expressions have been determined in Refs. 4, 7, 8, and 9 for specific fuels in various injectors. All of these distributions exhibit large errors when used in the small drop size range. More experimental data are required in this range so that a preferred distribution may be determined.

Ingebo and Foster (Ref. 7) used dimensional analysis to study the effect of seven physical properties upon the volume-mean droplet radius.

$$r_{30} = \left[\frac{\Sigma n r^3}{\Sigma n} \right]^{1/3}$$

They considered the following variables as having a possible influence,

$$r_{30} = f(D_0, \rho_l, u, \sigma_l, \mu_l, \rho_g, \mu_g)$$

where: D_o = injector-orifice diameter
 u = free stream velocity
 σ = surface tension
 μ = viscosity
 ρ = density

After dimensional grouping of terms they fit their numerous data with the equation

$$\frac{r_{30}}{D_o} = 1.9 \left(\frac{\sigma_1}{D_o \rho_g u^2} \right)^{1/4} \left(\frac{\mu_1}{D_o \rho_1 u} \right)^{1/4}$$

or

$$\frac{r_{30}}{D_o} = 1.9 \left(\frac{We}{Re} \right)^{1/4}$$

where:

$$\frac{\sigma_1}{D_o \rho_g u^2} = \text{Weber Number, } We$$

and

$$\frac{D_o \rho_1 u}{\mu_1} = \text{Reynolds Number, } Re$$

This data was recorded for cross-current break-up of liquid jets in high velocity airstreams.

They also empirically determined the expression for the maximum droplet radius,

$$\frac{r_{max}}{D_o} = 11.1 \left(\frac{We}{Re} \right)^{0.29}$$

and fit their size population with the Nukiyama-Tanasawa distribution:

$$\frac{dR}{dr} = 10^6 \left(\frac{We}{Re} \right)^{.24} \frac{r^5}{r_{max}^6} \exp \left[-22.3 \left(\frac{We}{Re} \right)^{.44} \frac{r}{r_{max}} \right]$$

Priem and Heidmann (Ref. 3) used these results (Ref. 7) in the form

$$r_{30} \propto r_m \propto \frac{\sigma_1^{.4} \mu_1}{\rho_1}$$

where r_m is the mass median droplet.

However, if the standard deviation changes, the volume-mean drop r_{20} , is not proportional to r_m , the mass-median drop. Priem and Heidmann used this relation although there is no experimental proof of its validity. Using this form they compared the median size for various propellants with the data of Ingebo (Ref. 8) for n-heptane impinging-jet break-up in airstreams simulating the velocity conditions in rocket combustors. The comparison equation was - where: x is the unknown propellant
h is heptane

$$r_{m,x} = r_{m,h} \left(\frac{\rho_h}{\rho_x} \frac{\sigma_x}{\sigma_h} \frac{\mu_x}{\mu_h} \right)^{1/4}$$

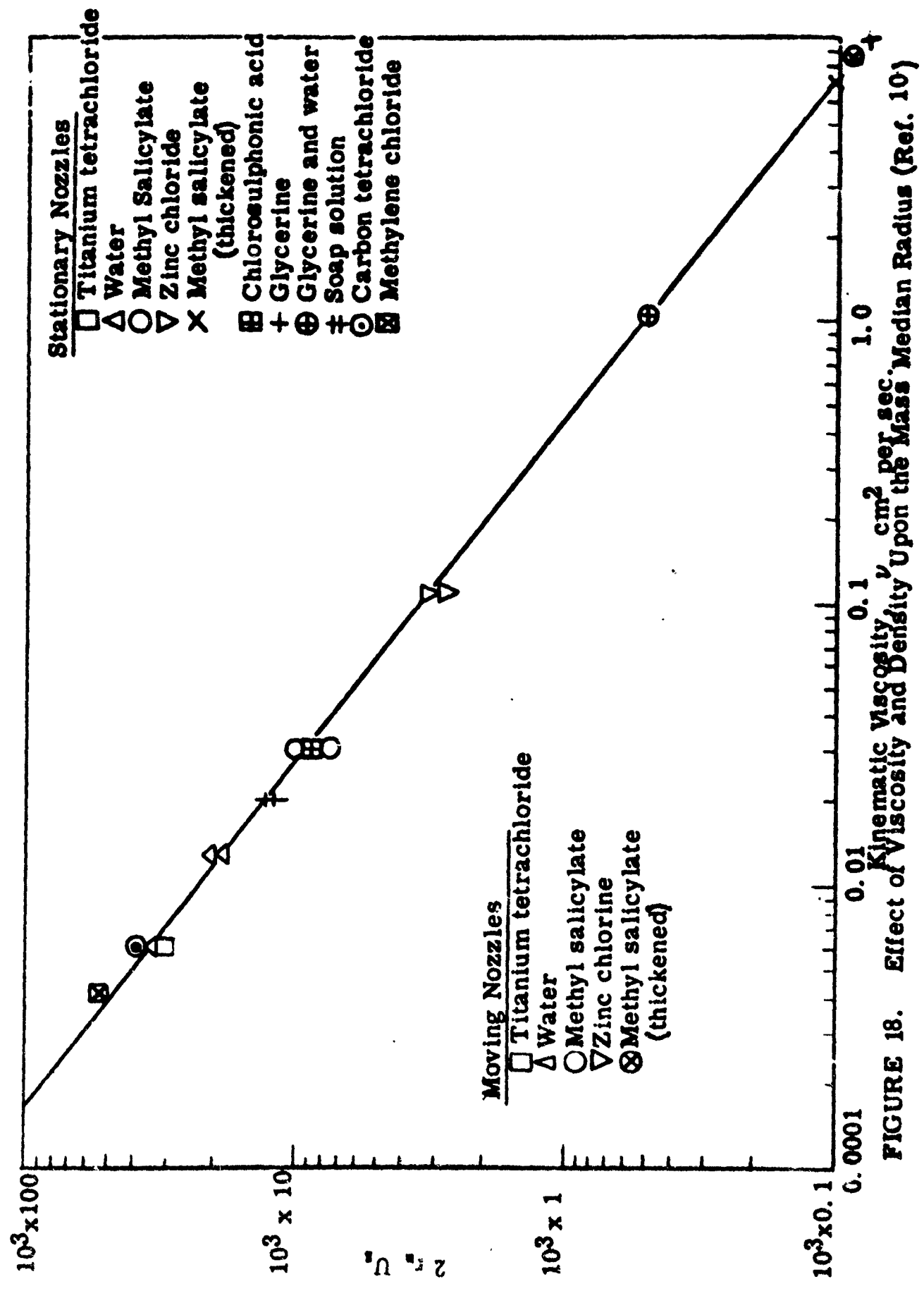
Merrington and Richardson (Ref. 10) plotted data showing a variation of four orders of magnitude in μ/ρ . These data, shown in Figure 18, determine that $r_m \propto (\mu/\rho)^{0.2}$; this is very close to the 0.25 power of Ref. 8 and can be used with confidence. The surface tension of most of the liquids of Figure 18 was 30 dynes/cm except for water and glycerine which have values of 73 and 63 respectively. These two liquids produced mean drop sizes expected from their respective kinematic viscosities, and showed no surface tension effects. Thus, the effect of surface tension on mean drop size is not fully understood.

Griffen and Lamb (Ref. 11) studied the dependence of mean drop-size on ambient gas density. They determined that the maximum droplet size was reduced with increasing ambient gas density according to the relation

$$r_{max} \propto \rho_g^{-0.2}$$

They comment that the apparent improvement in atomization (mean drop-size) with increasing pressure is mainly due to a reduction in the number of large drops and is probably caused by subdivision of these big droplets.

$(2r_0 U_0) / \nu_1 = 500; \nu_1 = 10^{-4} \text{ cm}^2 / \text{sec}$



Ingebo (Ref. 8) correlated data obtained for heptane sprays produced by pairs of 90° impinging jets over wide ranges of orifice diameter, D_o ; liquid-jet velocity, v_j ; and jet-airstream velocity difference, Δv ; according to the equation

$$\frac{D_o}{r_{30}} = 5.28 \left[D_o v_j \right]^{1/2} + 1.94 D_o \Delta v$$

Heidmann and Foster (Ref. 4) studied the effects of impingement angles of 10° to 90° and jet velocities of 30 to 74 feet per second. All their distributions showed bimodal characteristics. The most significant effect of impingement angle and jet velocity was a change in the relative number of drops in each mode. This is consistent with the hybrid nature of impinging jets (i.e., drag instability break-up) and the fact that they determined that sheet thickness, t , varied according to

$$t \propto (P v_j)^{1/2}$$

This data (Ref. 4) could be further analyzed, using an instability model to relate sheet thickness to drop size distribution. Thus a single model and semi-empirical equation would be developed, using injector parameters to predict sheet thickness, and physical properties to predict instability break-up and final size distribution.

In the absence of any general theoretical treatment of the effect of mass flow rate and velocity upon r_{30} , several purely empirical relations have been determined for different atomizer designs. Radcliffe (Ref. 12) determined the surface mean radius, r_{20} , of the spray produced by a simple swirl atomizer. He developed the relation

$$r_{20} \propto \dot{W}^{0.318} / \Delta P^{0.530}$$

where \dot{W} = fuel flow rate

and ΔP = injector pressure drop.

Fraser and Eisenklam (Ref. 13) obtained the following correlation for a fan spray nozzle

$$r_{20} \propto \dot{W}^{0.203} / \Delta P^{0.349}$$

For a somewhat different type fan spray (Ref. 14 and 15) it was determined that

$$r_{20} \propto \dot{W}^{0.25} / \Delta P^{0.305}$$

It can be concluded that while there are empirical correlations for some special injectors, it is not possible to use data obtained on one type for calculation of the operation of another type. A complete understanding of the influence of propellant variables on drop spray has not yet been realized.

An experimental program was proposed in the Semiannual Report (Ref. 2), in order to supply needed atomization data. The objective is to relate propellant properties and design parameters to droplet spray distribution. Propellant properties which influence droplet distribution are density, ρ_1 ; viscosity, μ_1 ; and surface tension, σ . Design parameters of importance to impinging atomizers are injection velocity, v_j ; surrounding gas velocity, u ; impingement angle, θ ; and the injector characteristics (diameter, D_0 ; length ratio, L/D_0 ; and outlet configuration, i.e., burrs or rounded).

5. Solid Particle Effects on Stability.

The stabilization of combustion in solid rocket propellants containing powdered metals has stimulated a great deal of research in an effort to determine the mechanisms of the stabilization process. Some of the more important observations concerning the effects of metal powders in solid propellants and solid exhaust particles are summarized in Reference 2. The principle objective of this review of solid particle effects on combustion instability is to determine possible applications of the same principles to liquid propellant systems. The basic equation for the calculation of the energy dissipation for conditions applicable to liquid systems is given by the equation of Epstein and Carhart (Ref. 16).

$$\beta = \frac{6\gamma c r v}{g} (1+z) \frac{16z^4}{16Z^4 + 72\gamma Z^3 + 81\gamma^2 (1+2z+2z^2)}$$

The actual values for energy loss due to particle attenuation can be presented in several ways. The quantity β represents the quantity $\frac{1}{E} \frac{dE}{dl}$ which corresponds to the fractional energy loss per foot of wave travel. Division of this quantity by the wave length provides the energy loss per cycle.

In an analagous manner, the quantity, $\beta x q$ represents $\frac{1}{E} \frac{dE}{dt}$ or the fractional energy loss per second and division by the angular frequency represents the energy loss per cycle.

In order to simplify the presentation of results the quantity β/c is presented. This quantity represents the energy loss per particle. The total energy loss can be obtained by multiplication by the number of particles per cubic foot of volume. For a distribution of particles, the total attenuation can be obtained from the following:

$$\beta = \sum_i \beta_i$$

The results for particles corresponding to aluminum, aluminum oxide, hydrazine and mixtures of aluminum and hydrazine are presented in figures 19 and 20 where $\beta/c\omega$ is plotted as a function of ω with particle radius as a parameter. When multiplied by, q , the velocity of sound in the gas, the quantity $\beta/c\omega$ represents the energy loss due to attenuation, $\frac{1}{E} \frac{dE}{dt}$ per particle per cycle. It is evident that the actual attenuation per particle increases in the frequency

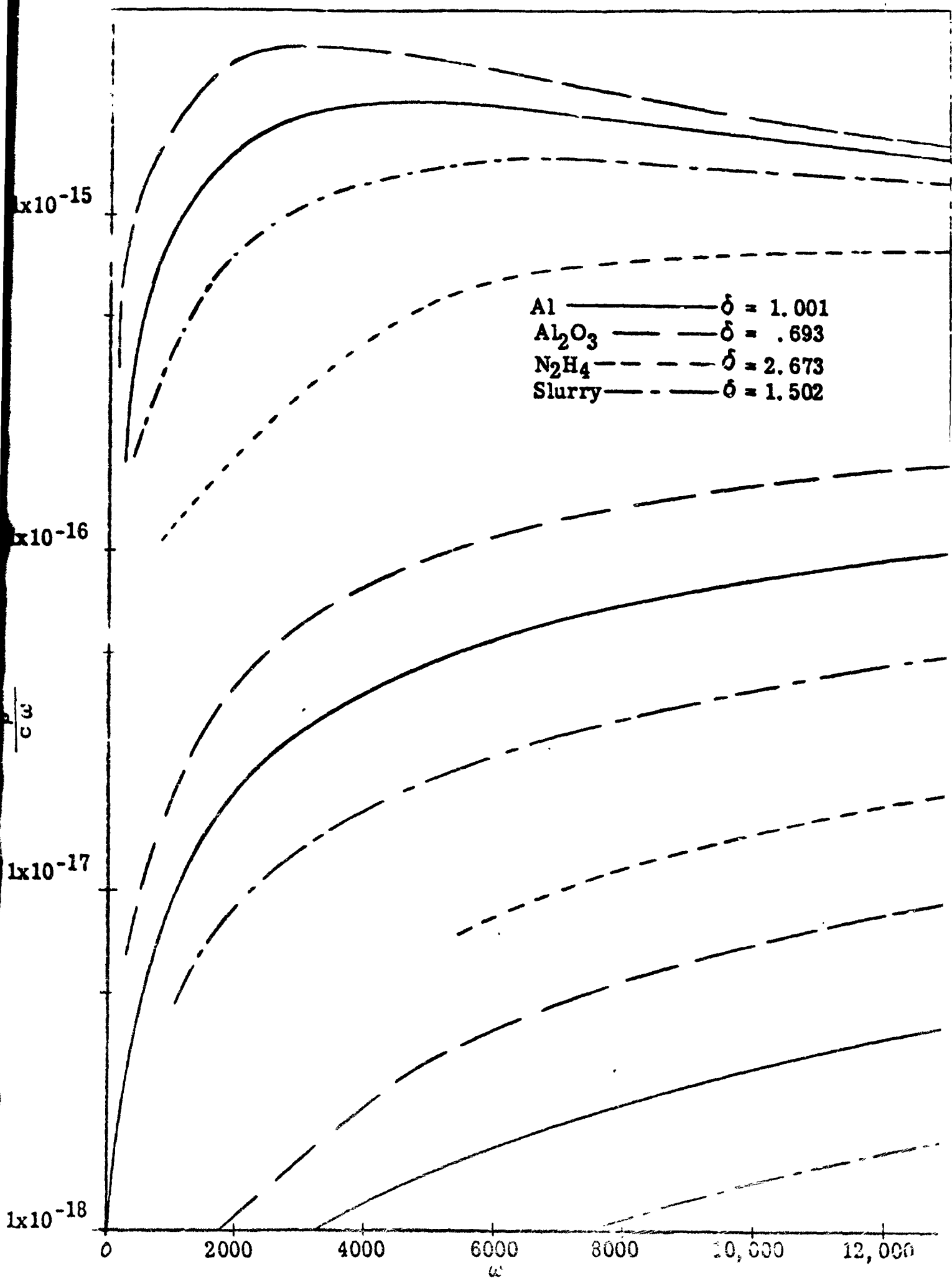


FIGURE 19. VISCIOUS ATTENUATION PER CYCLE PER PARTICLE

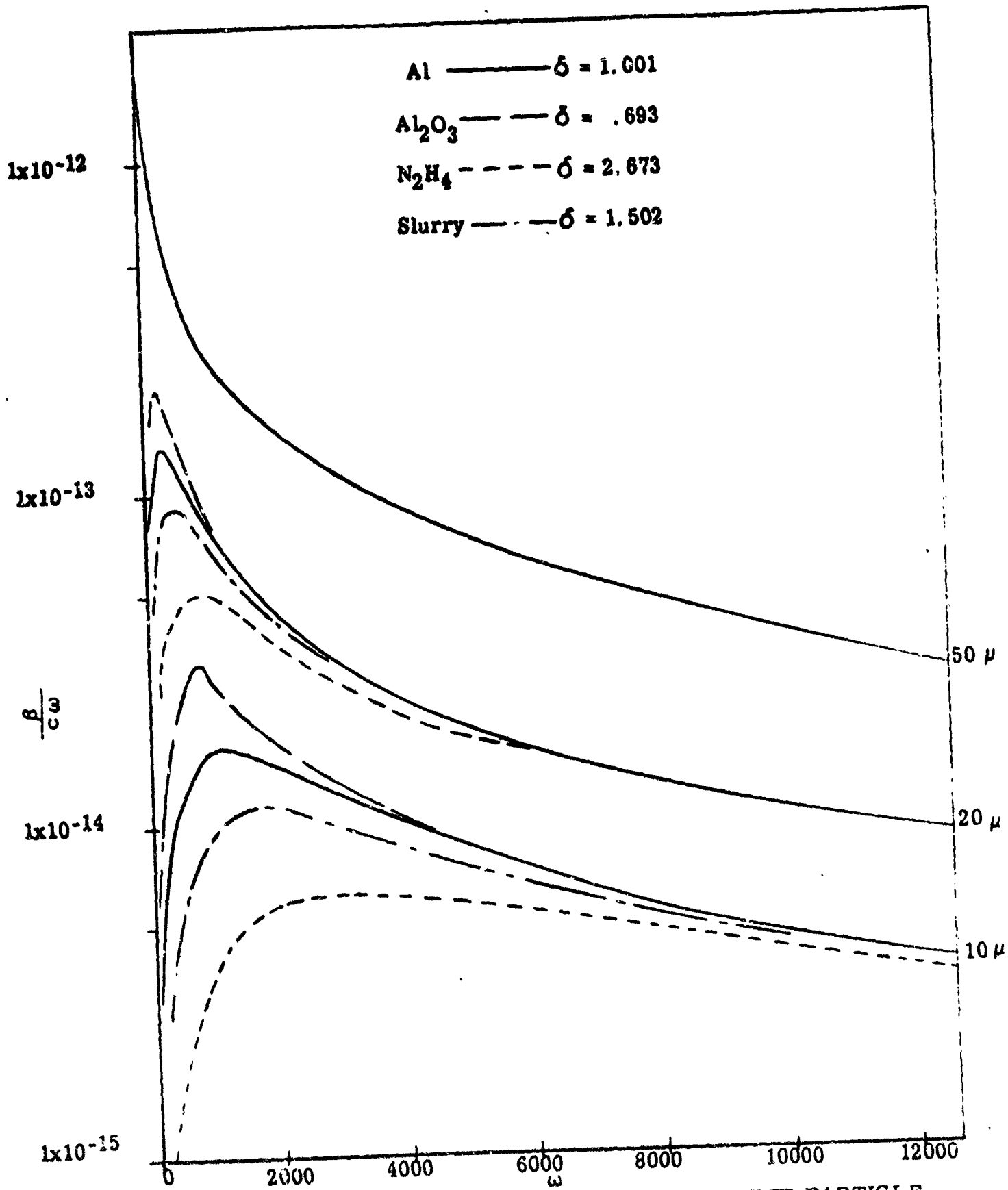


FIGURE 20. VISCOUS ATTENUATION PER CYCLE PER PARTICLE

range considered as the particle size increases. Particle density also has an effect, the heavier particles giving more attenuation. This is illustrated in Figure 21 for 10 micron particles. The effect of particle density is appreciable in the range 0 to 5000 and becomes negligible at frequencies above 15,000.

The results illustrated in Figures 19, 20 and 21 apply for a comparison when the same number of particles of each size or type are involved. This can be misleading, however, since the factor which is generally held constant is the weight of solid materials. For a given weight of a specified material, there are more small particles than large particles. To convert the data per particle to data per unit weight, the values should be divided by $\frac{4}{3} \pi r^3$. In Figure 22, data for aluminum are compared on the basis of $\frac{8}{c \omega r^3}$ which is proportional to the attenuation per cycle per unit weight. Multiplication of the factor plotted in Figure 22, by $\frac{3}{4} \frac{q}{\rho_p}$ would give the actual attenuation per

cycle per unit weight of aluminum. Above a frequency of 2300, 5 μ particles show more attenuation than 10 μ particles simply because there are 8 times as many 5 μ particles.

In order to compare the attenuation per unit weight for particles of different density, the density terms should be included. A relative comparison is given in Figure 23 where $(\frac{8}{c \omega r^3}) \delta$ is plotted against frequency. On this basis, the maximum attenuation is almost independent of density although the maximum occurs at different frequencies.

For the frequency range of interest in most liquid systems, particle sizes of the order of 2-20 microns appear to be of most interest. Although particle density affects the actual value of the energy loss due to particles, the differences are not great so that hydrazine, aluminum, aluminum oxide and slurry particles have similar damping effects.

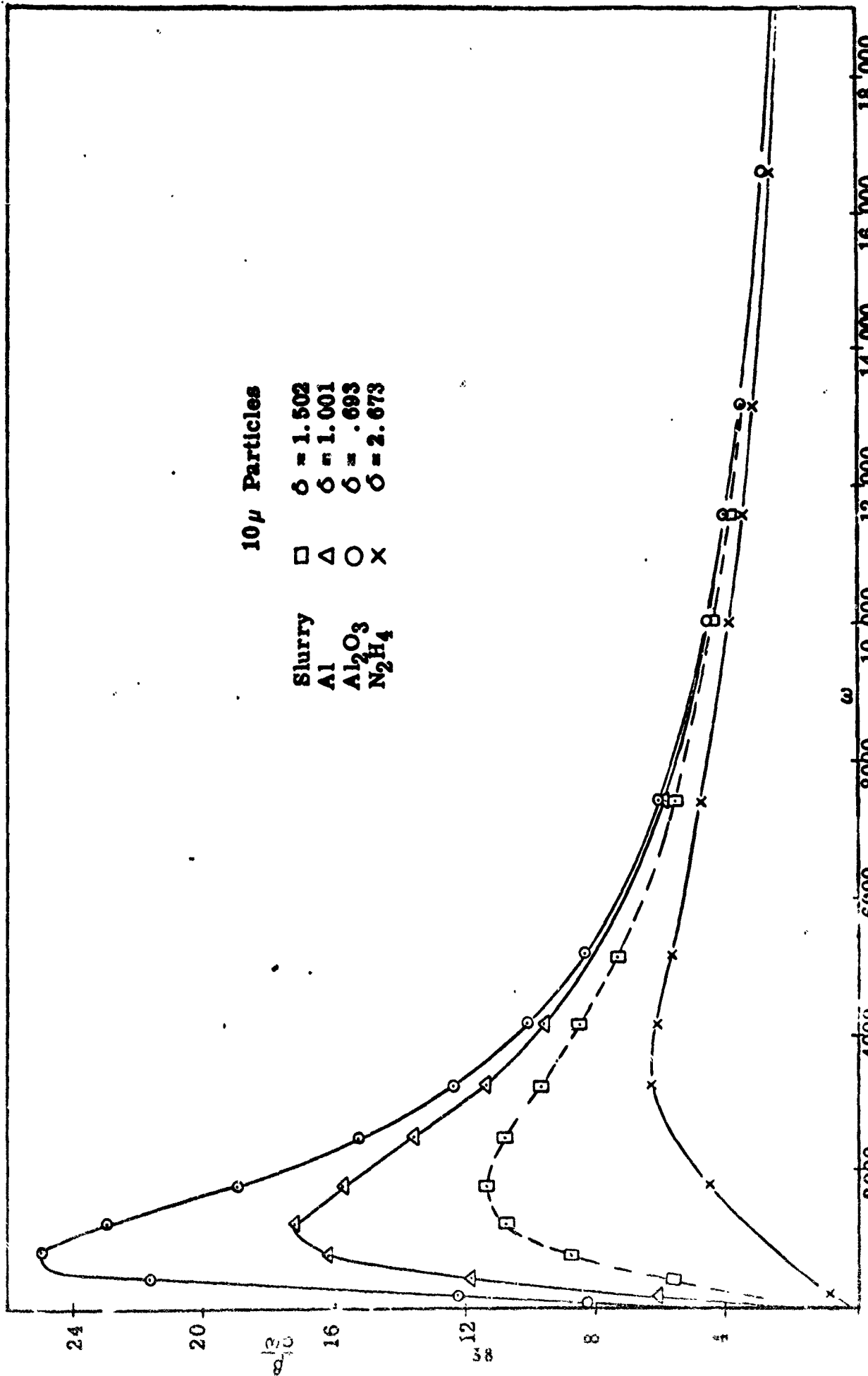


FIGURE 21. VISCOS ATTENUATION PER CYCLE PER PARTICLE, 4 Type Particles, 10 Micron Dia.

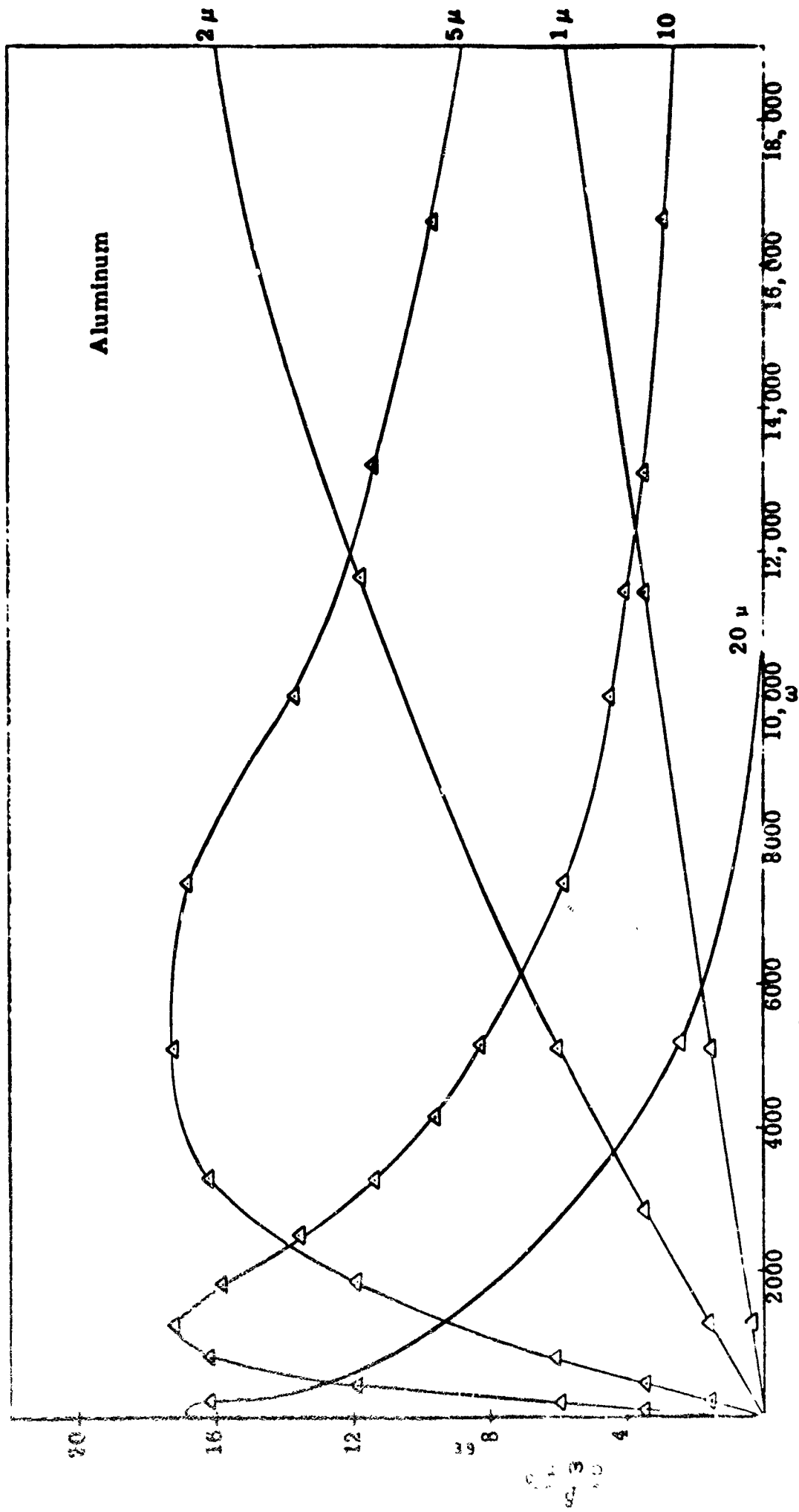


FIGURE 22. VISCIOUS ATTENUATION PER CYCLE PER UNIT MASS.

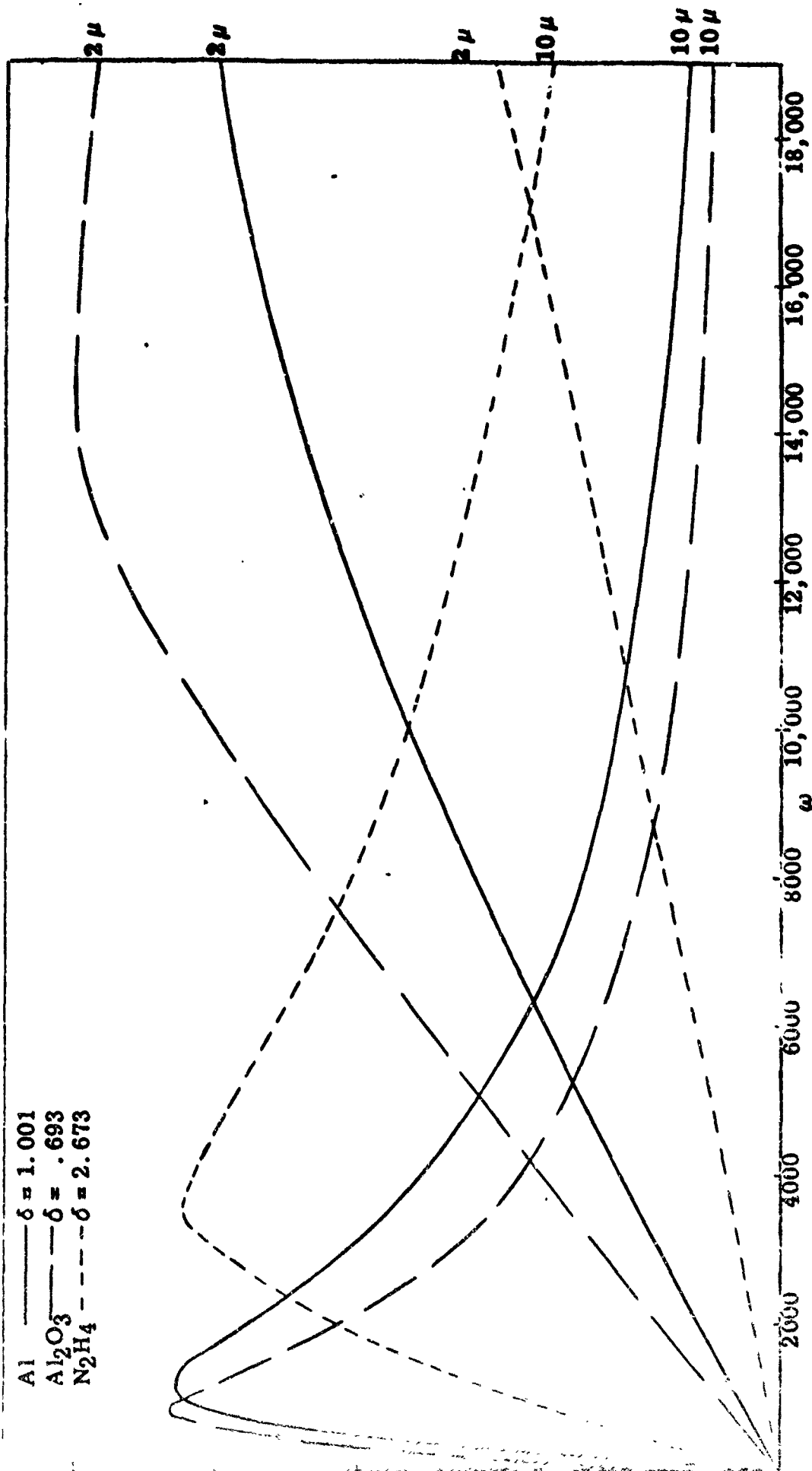


FIGURE 23. VISCOUS ATTENUATION PER CYCLE PER UNIT MASS FOR 3 Type Particles, 10 micron dia.

III. PARAMETRIC STUDY OF COMBUSTION INSTABILITY

This section reports the results of a parametric study of the influence of liquid rocket engine parameters on combustion instability. A basic configuration was chosen with a similar geometry as the Transtage. Results are based on a mono-methylhydrazine and nitrogen tetroxide propellant combination. This study investigates the influences of propellant mixture ratio, injection velocity, droplet size and distribution, and chamber pressure on the minimum pulse strength required to trigger instability.

Results of this section are obtained by a method using a nonlinear model for determining the zones of a liquid rocket engine in which a tangential mode of high frequency instability is most easily initiated. A method for determining these zones was developed by Beltran, et al (Ref. 1). A rocket engine is analyzed by incrementally dividing the combustion chamber into annular nodes in the r and z directions. Steady-state properties at each annular node or position in the chamber are computed from the propellant vaporization program. These steady-state properties and the stability limit curves from the instability model are used to determine the stability of the node. This process is repeated for each node to determine a stability map of the entire engine.

1. Steady-State Analysis

The steady-state performance of a storable propellant liquid rocket engine of Transtage configuration has been investigated. Injector parameters were varied in a computer parametric study which utilized the Dynamic Science Corporation steady-state spray combustion computer program. This program (Ref. 1) includes a dissociation flame model for hydrazine type fuels. The propellant combination examined was MMH and N_2O_4 . The fuel and oxidizer drop sprays are characterized by a logarithmic normal distribution of drop radii about a specified mean drop size. The spray is divided into five groups of equal mass. The group of smallest radius, however, is divided into five groups again, making a total of nine groups used to define the spray. This was done to obtain more definition in the region of smallest drop size. The mean drop size, standard deviation of the spray, number of drop groups, and mass flow rate are the parameters used to define the spray distribution. Table I shows the initial drop radii and number of drops in each of the groups for the base engine spray (spray around which the injection parameters were varied). The values in Table I correspond to a mass mean drop radius of 75μ ($.03$ in) a standard

TABLE I

OXIDIZER SPRAY DISTRIBUTION

$r_m = 75\mu$ (.003 in), $\sigma = 2.3$, $\dot{m} = 18$. lb/sec

Group	Radius (mil)*	Number
1	0.5420	1.641×10^{10}
2	0.8221	4.700×10^9
3	1.0329	2.370×10^9
4	1.220	1.431×10^9
5	1.4024	9.470×10^8
6	1.9428	1.781×10^9
7	3.0000	4.837×10^8
8	4.6324	1.314×10^8
9	8.7134	1.974×10^7

FUEL SPRAY DISTRIBUTION

$r_m = 75\mu$ (.003 in), $\sigma = 2.3$, $\dot{m} = 9$. lb/sec

Group	Radius (mil)	Number
1	0.5420	1.039×10^{10}
2	0.8221	2.976×10^9
3	1.0329	1.500×10^9
4	1.2220	9.062×10^8
5	1.4024	5.995×10^8
6	1.9428	1.127×10^9
7	3.0000	3.062×10^8
8	4.6324	8.317×10^8
9	8.7132	1.250×10^7

* 1 mil = 25.4 μ

deviation of 2.3, total flow rate of 27.0 lb/sec and a 2:1 mixture ratio.

The chamber distance [x] along which the governing equations were integrated has its origin at the atomization point of the impinging streams. Figure 24 shows a water flow simulation of the stream breakup. The impingement diameter of the streams is .0625 inches and its velocity is approximately 1200 in/sec. The breakup into drops is seen to occur within 0.50 inches of the impingement point. Therefore, the assumption of an atomized spray vaporization model close to the injector face appears justified.

The parameters were varied around values selected as typical of a Transtage type engine. These typical values will be denoted as base engine values. (Shown in Table II)

Base parameters used for this study were:

Propellant	N ₂ O ₄ and MMH
Injection Velocity*	1000 in/sec
Chamber Pressure (initial value)	100 lb/in ²
Initial Temperature*	530° R
Total Mass Flow	27.0 lb/sec
Mixture Ratio	2.0:1
Specific Heat Ratio of Combustion Gases	1.20
Mass Mean Drop Radius*	.003 in
Standard Deviation*	2.3
Number of Groups*	9

The chamber configuration was specified as conical with a taper from 107 in² to 44 in² in a 17 in. distance.

A series of computer runs were made with specified parameters varied around the base engine values shown above. Each parameter was varied independently of the others, that is, the others were held constant at base engine values. This was done to determine the significance of the parameters varied and pinpoint quantities that require accurate determination.

The first two runs were made with the base engine quantities. The runs were identical with the exception that the dissociation flame was suppressed on the second. The variation of the vaporization rate [fraction/inch] of the MMH spray with distance

*Both propellants.

WATER FLOW SIMULATION OF STREAM IMPINGEMENT

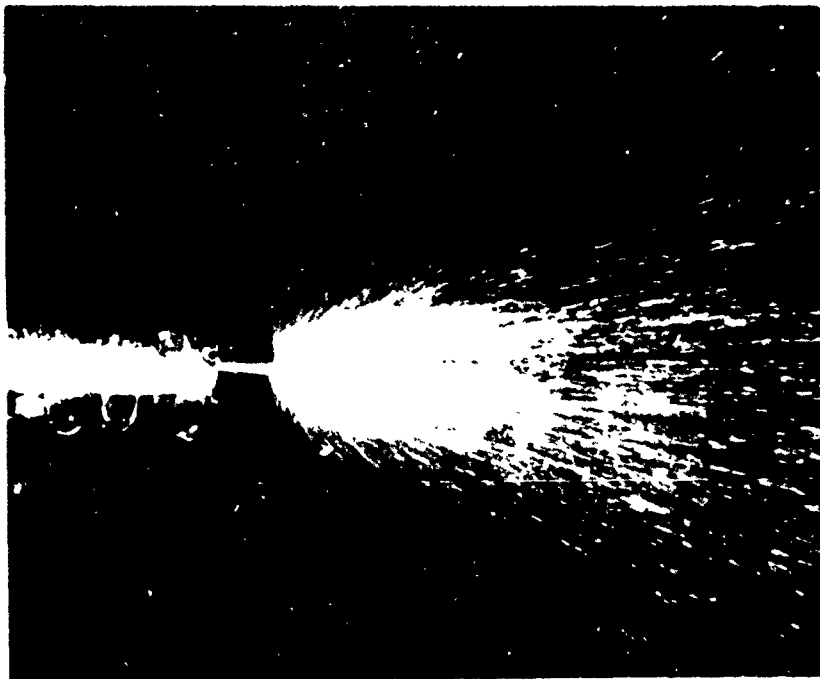


FIGURE 24. Water Stream Impinging at 90°.
Stream Diameter .0625 inch
Injection Velocity Approximately 1200 in/sec.

TABLE II
STEADY-STATE and INSTABILITY PARAMETERS

Comp. Run	Varied Parameters	Controlling Propellant	Minimum ΔV Inches	r_s Mils	Re_d	L	$\Delta P/P$
1	Base Engine	OX	0.24	0.94	320	0.40	0.032
2	Without TF	Fuel	0.75	0.75	379	0.19	0.050
3	25 μ	OX	0.03	0.30	105	4.62	0.080
4	225 μ	OX	1.43	3.04	1021	0.05	0.099
5	1 σ	OX	0.76	2.95	1234	0.10	0.037
6	1 σ	OX	0.03	0.24	93	3.24	0.087
7	300 psi	OX	0.75	1.27	1361	0.12	0.032
8	500 psi	Fuel	1.53	1.68	3270	0.05	0.052
9	500 in/sec	OX	0.07	0.88	305	0.75	0.032
10	2000 in/sec	OX	0.89	1.01	352	0.23	0.040
11	O/F 1.6/1	OX	0.28	0.95	431	0.31	0.030
12	O/F 2.5/1	OX	0.25	0.93	316	0.48	0.031

down the chamber from the point of atomization is shown in Figure 25. Including the exothermic dissociation flame produces approximately a 300-400% increase in the initial vaporization rate. After 2.5 inches the rates are seen to cross as the higher initial rate has caused the loss of the smaller drops from the distribution leaving only the slower vaporizing larger size drops. At the cross-over point ($x=2.5$ inches), the inclusion of the two flame model has raised the total fraction of the fuel spray vaporized from 20% to 42%.

The variation of the oxidizer vaporization rate with chamber distance for these two runs is shown in Figure 26. The change is rather slight, however, there is some variation since:

a. The higher fuel vaporization rate causes the chamber gas velocity to increase more rapidly affecting the heat and mass transfer coefficients to the drop.

b. The local O/F ratio is altered by the high fuel vaporization rate. This affects the adiabatic flame temperature [driving potential for heat transfer] as well as the partial pressures of the species in the combustion gases [driving potential for mass transfer].

c. The change in local O/F ratio between these runs also causes changes in the transport properties of the diffusion mantle by altering the equilibrium composition of the combustion gases. Note: Thus the fuel vaporization rate is increased significantly by the two flame model and this effect, in turn, causes an increase in the oxidizer vaporization rate; the two being interrelated. Of particular interest is the change in the local O/F ratio with the inclusion of the two flames. The calculated values of O/F are shown in Figure 27 for these two runs. The two flame model has caused the combustion process to switch from fuel controlling [$O/F > 2.5$] to oxidizer controlling [$O/F < 2.5$]. For reference, the machine plots of fraction vaporized, gas Mach number, fuel and oxidizer drops radii, and fuel and oxidizer drop velocities for the runs with and without the two flame burning regime are shown in Figure 28-33 and 34-39 respectively. It was noted that the fuel drops were at all times within the two flame regime for the base engine run.

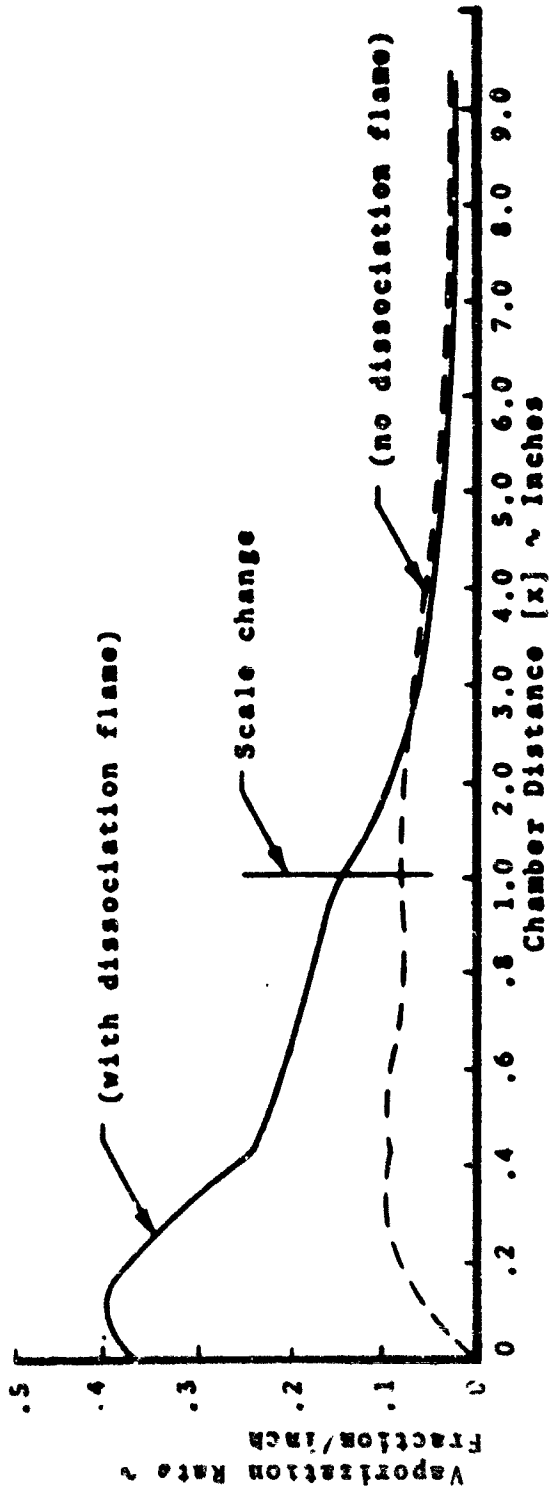


FIGURE 25. Effect of Dissociation Flame on Fuel Vaporization Rate.....

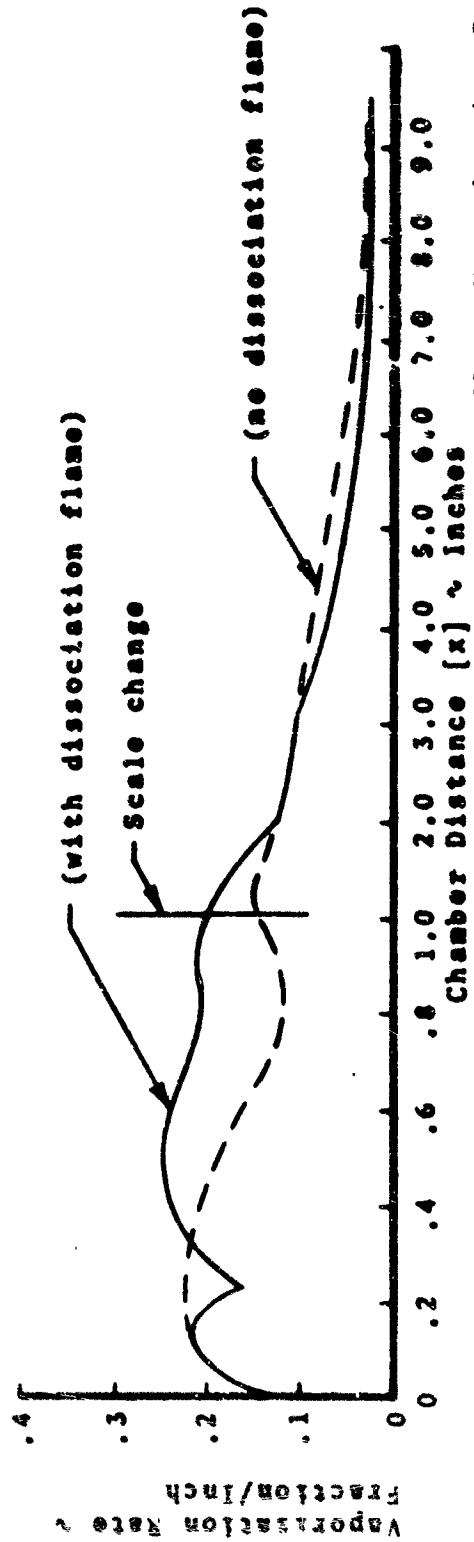


FIGURE 26. Effect of Fuel Dissociation Flame on Oxidizer Vaporization Rate

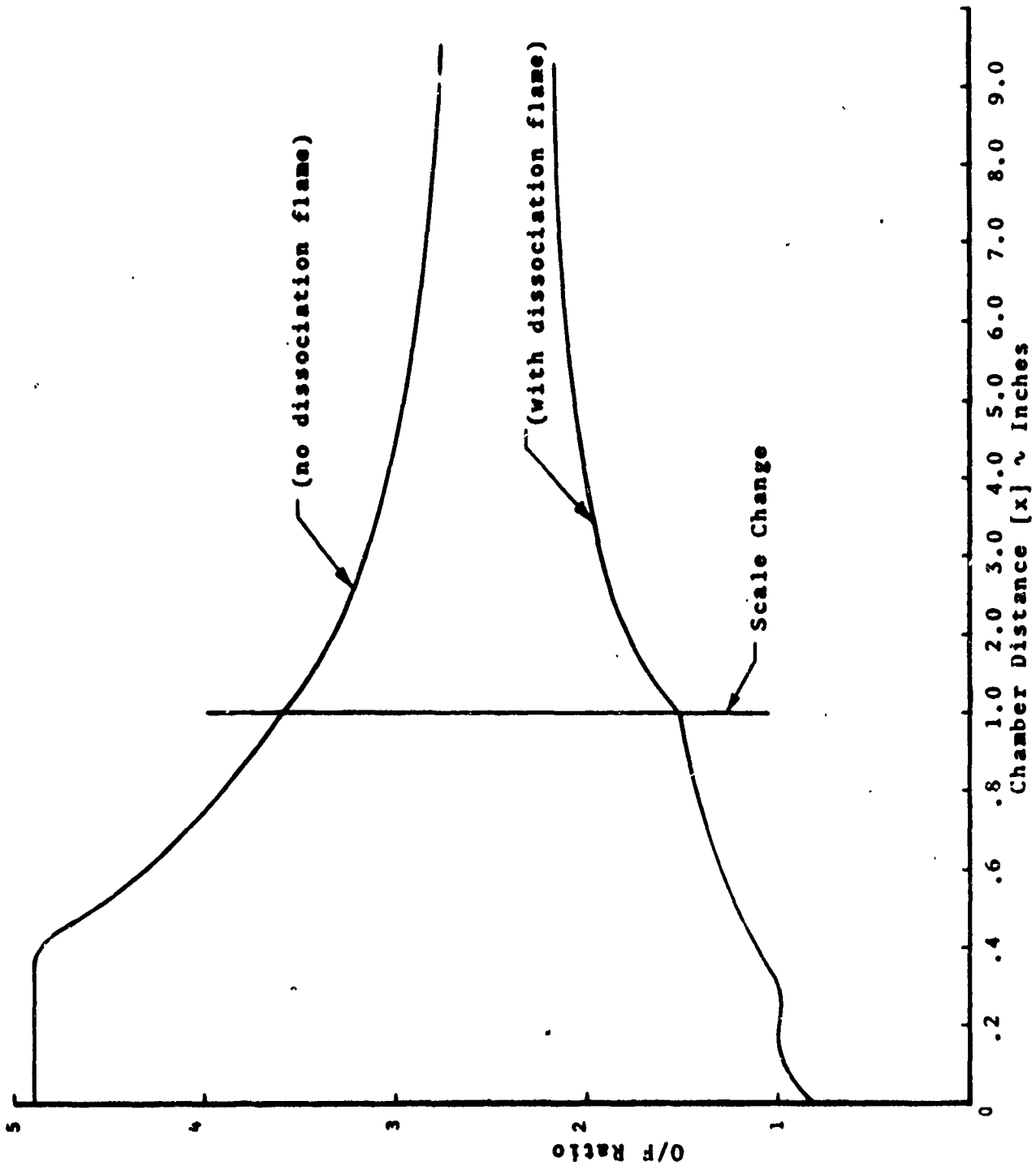


FIGURE 27. Effect of Fuel Dissociation Flame on Local O/F Ratio.

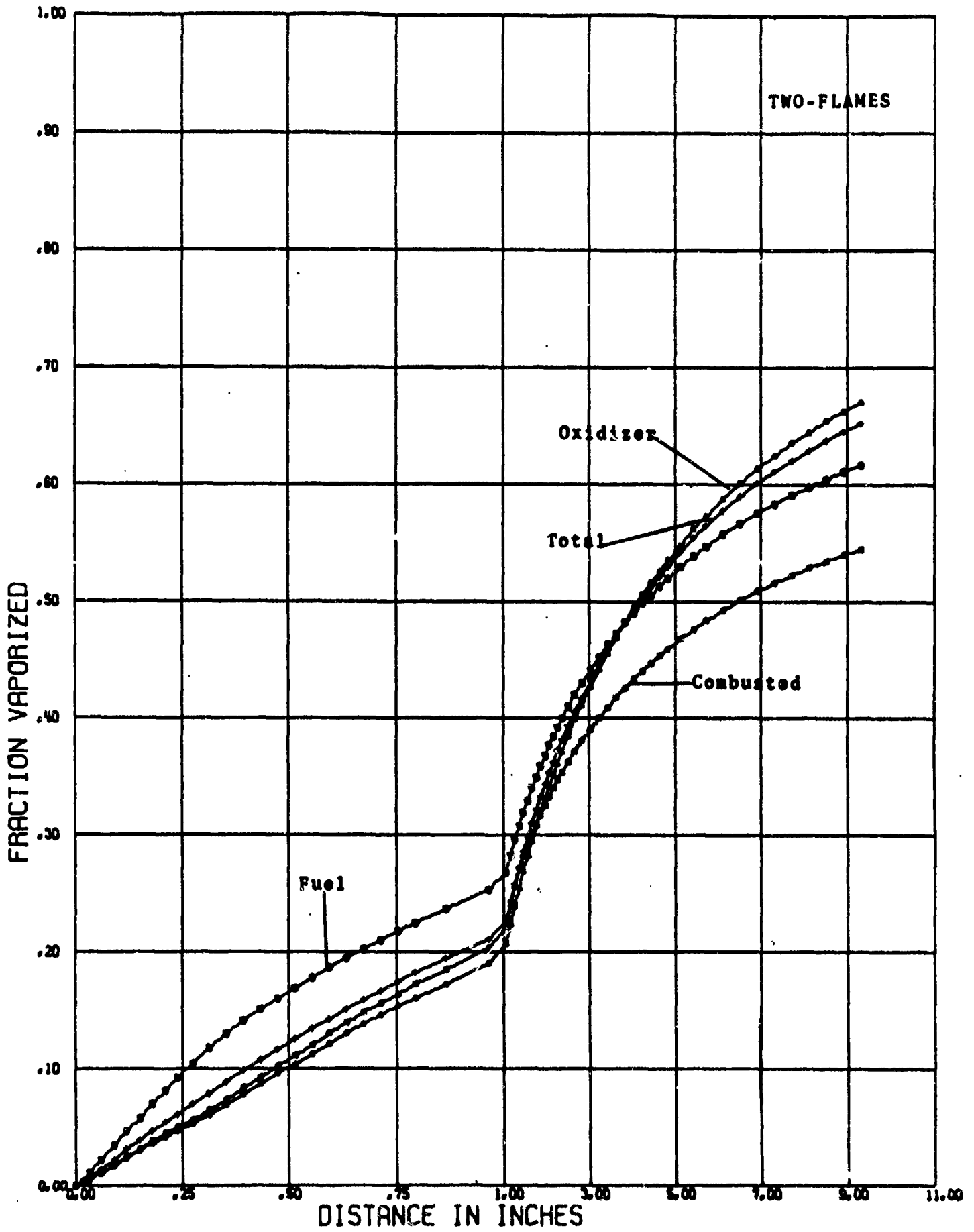


FIGURE 28. Vaporization Profile (using dissociation flame model)

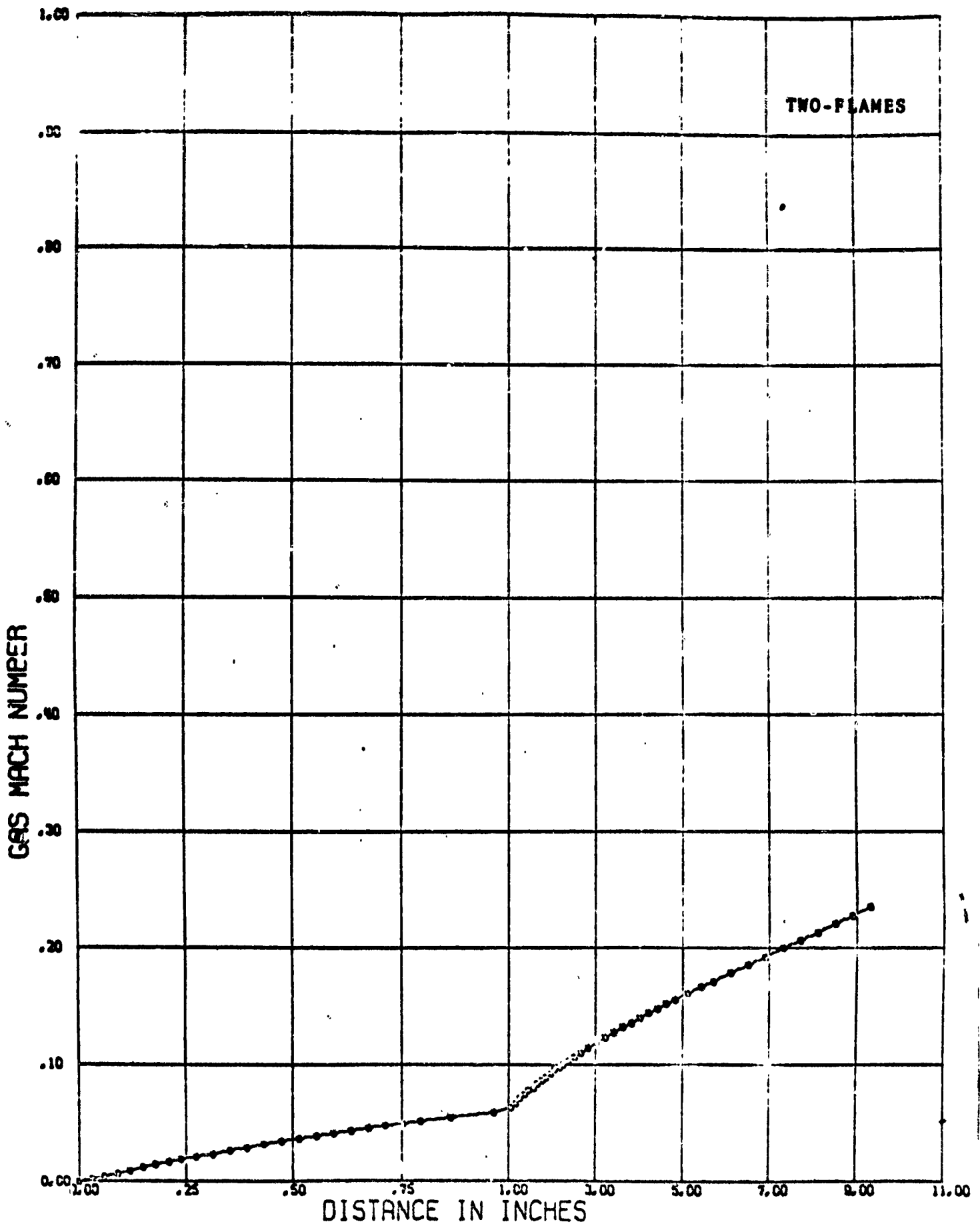


FIGURE 29. Gas Velocity (using dissociation flame model)

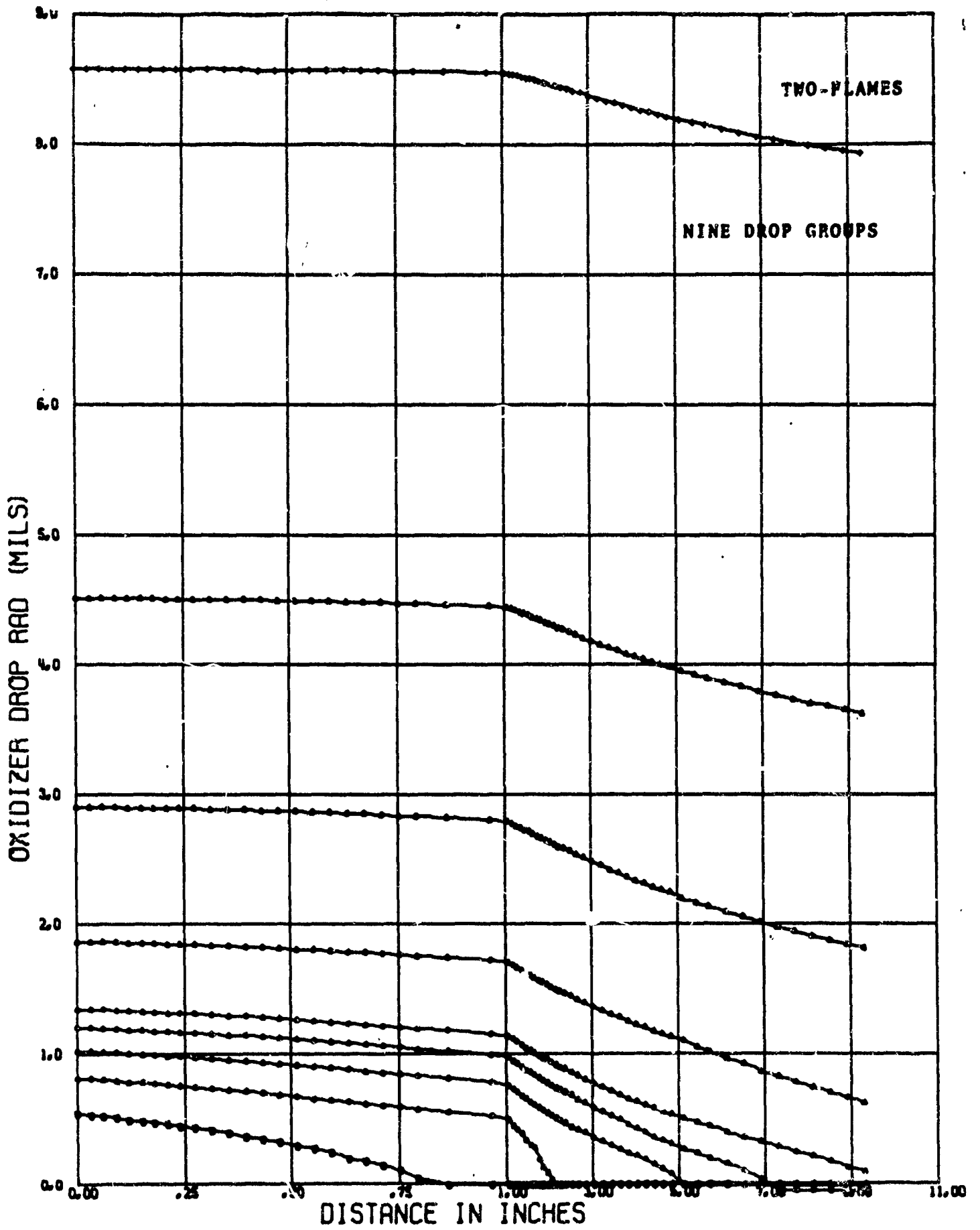


FIGURE 30. Fuel Drop Radius (using dissociation flame model)

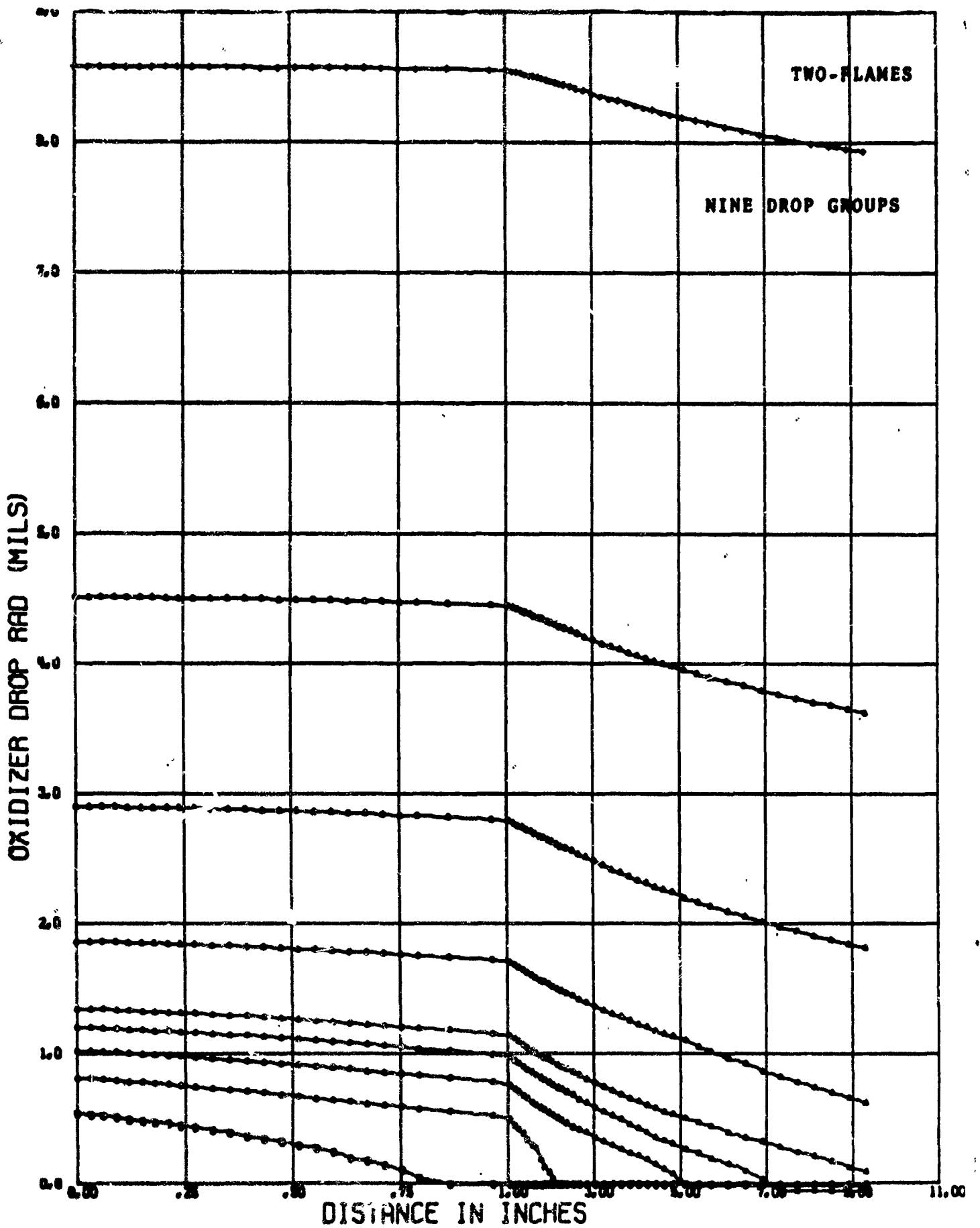


FIGURE 31. Oxidizer Drop Radius (using dissociation flame model)

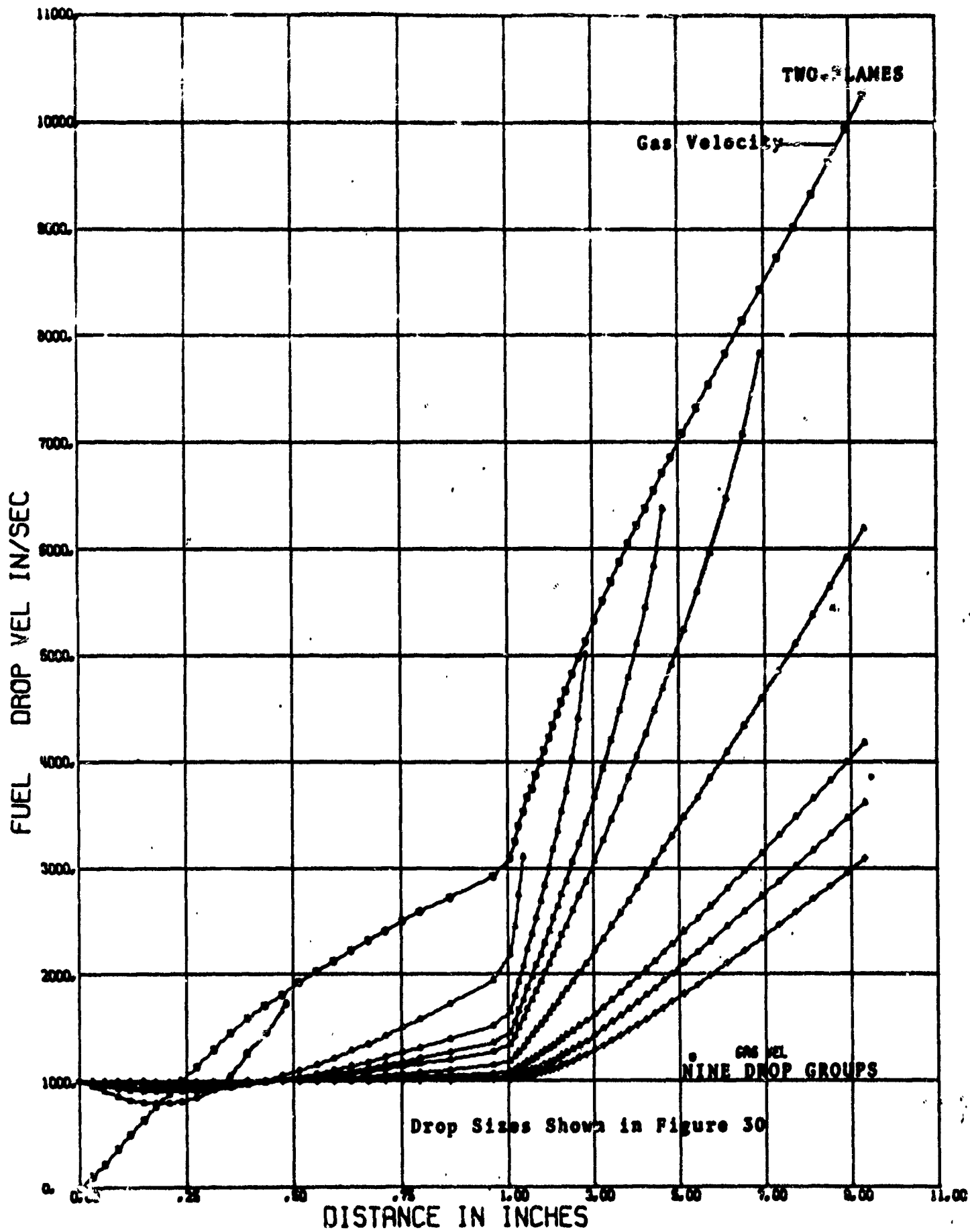


FIGURE 32. Fuel Drop Velocities (with dissociation flame)

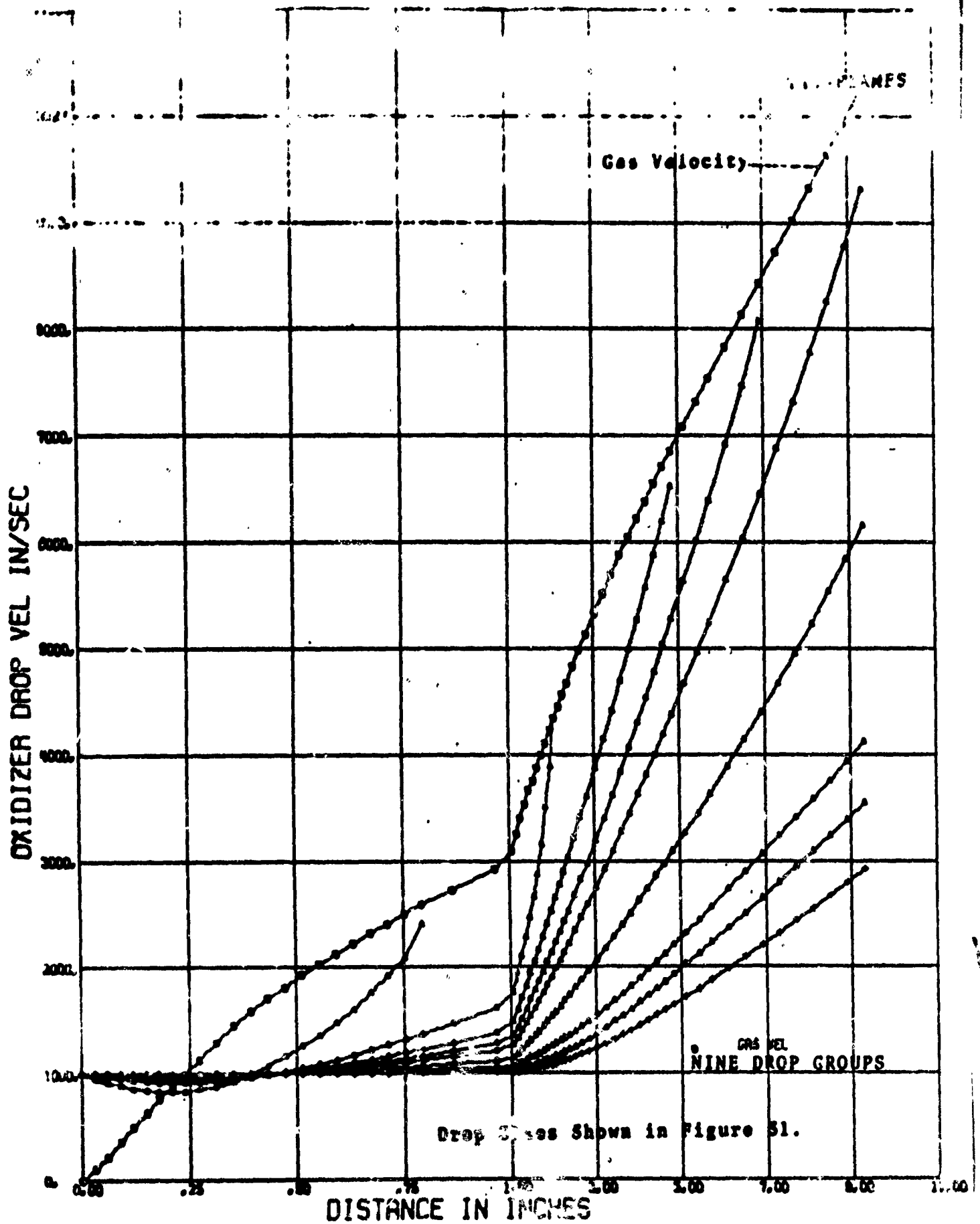


FIGURE 33. Oxidizer Drop Velocities (using decomposition flame model)

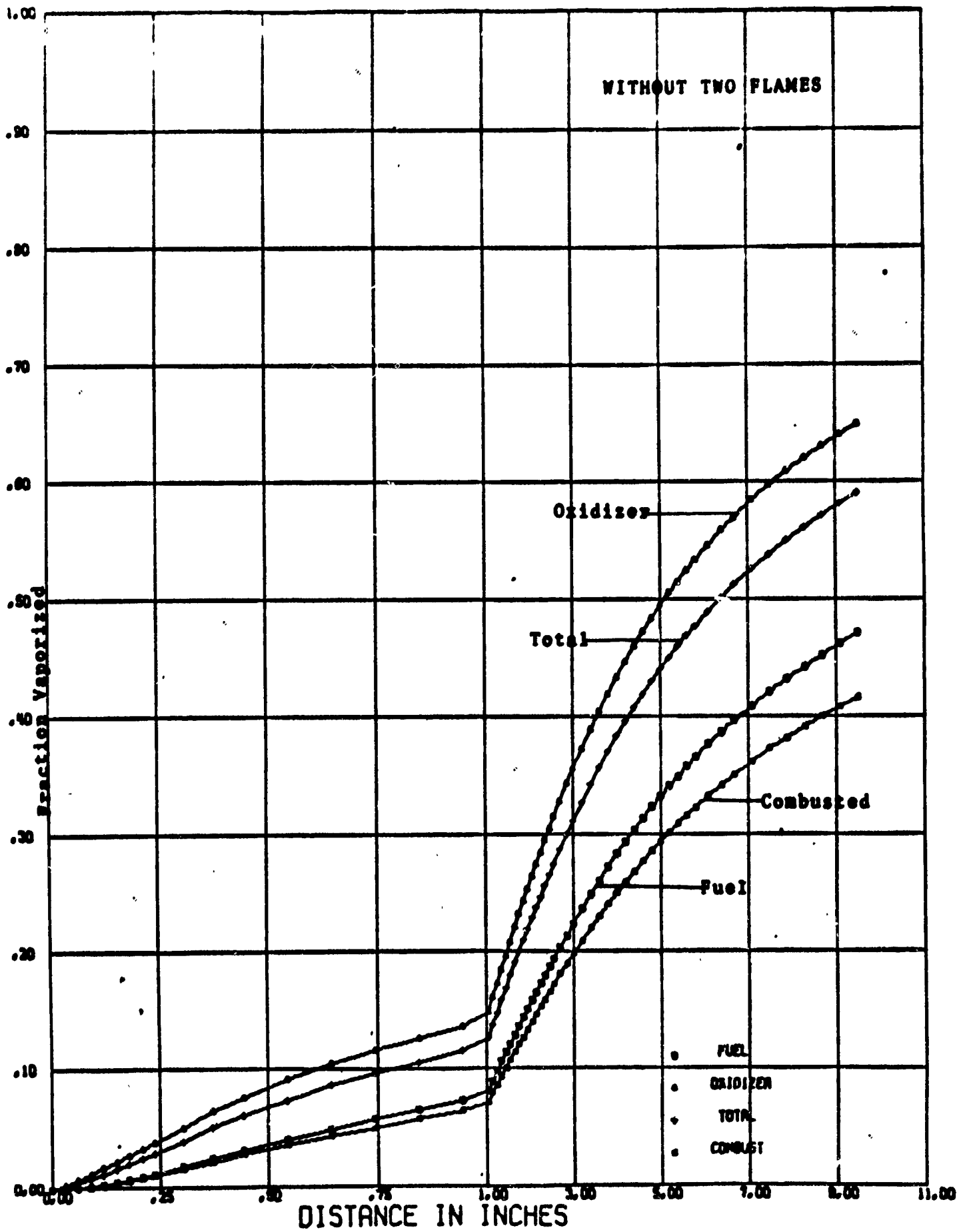


FIGURE 34. Vaporization Profile (no decomposition flame)

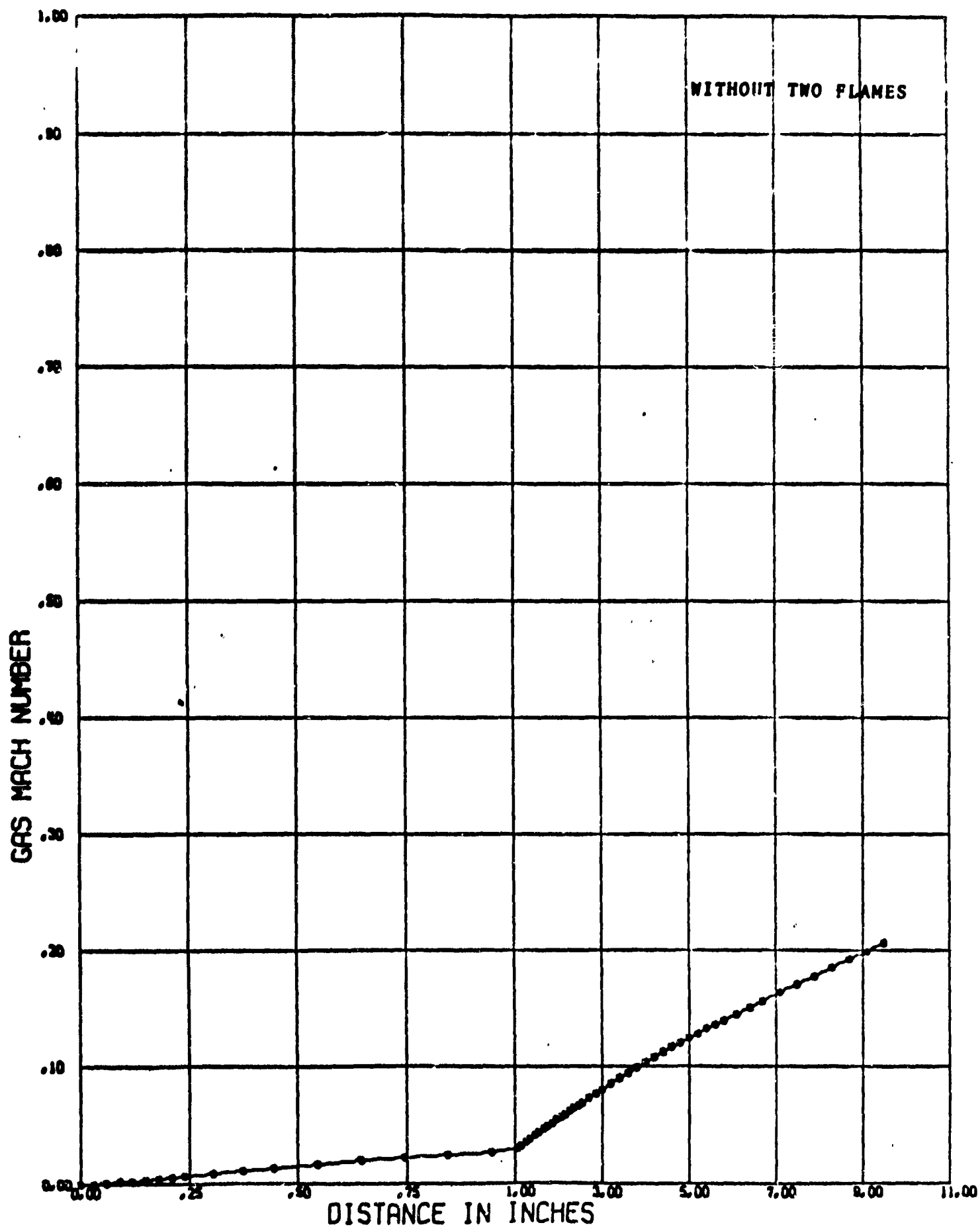


FIGURE 35. Gas Velocity (no decomposition flame)

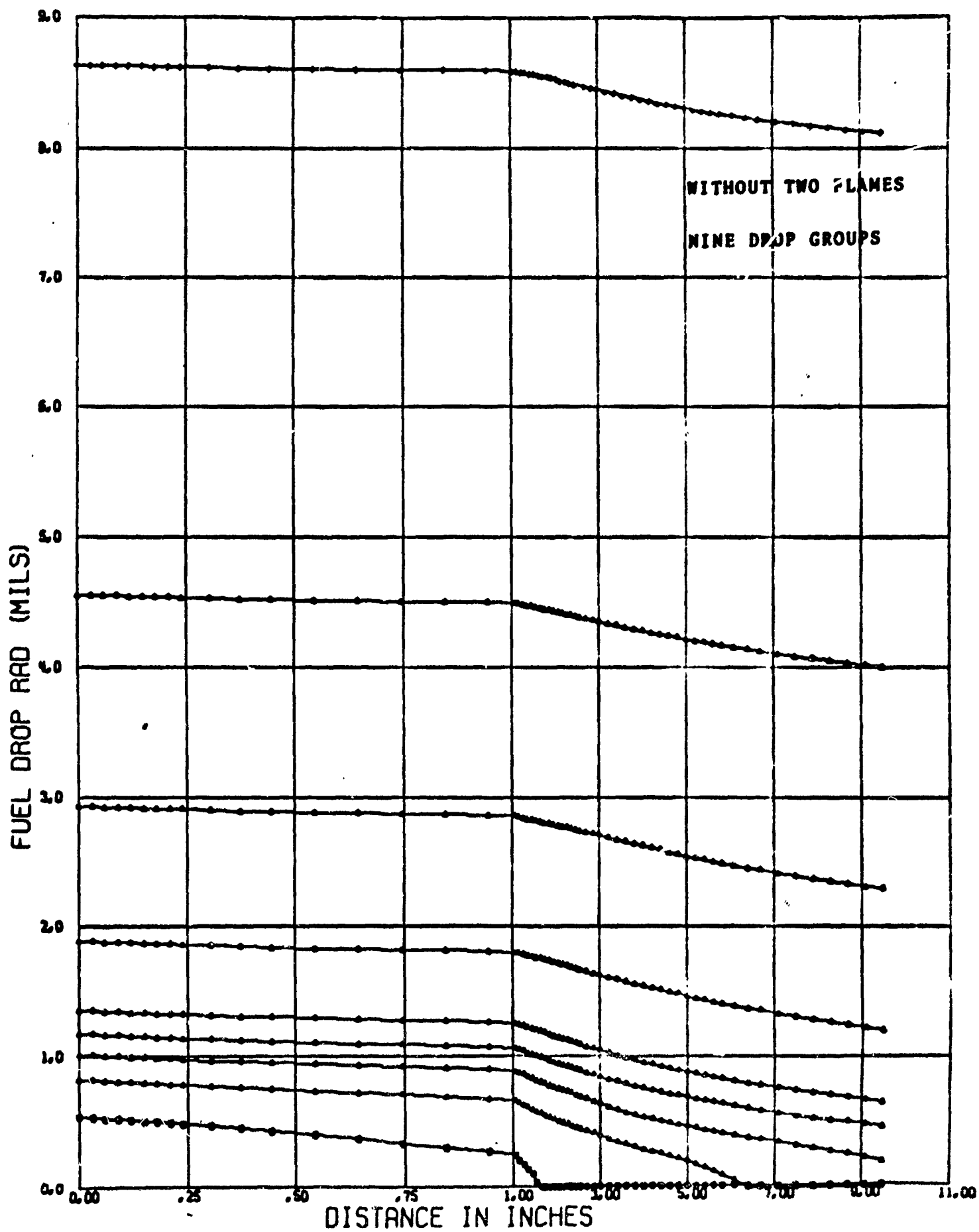


FIGURE 36. Fuel Drop Radius (no decomposition flame)

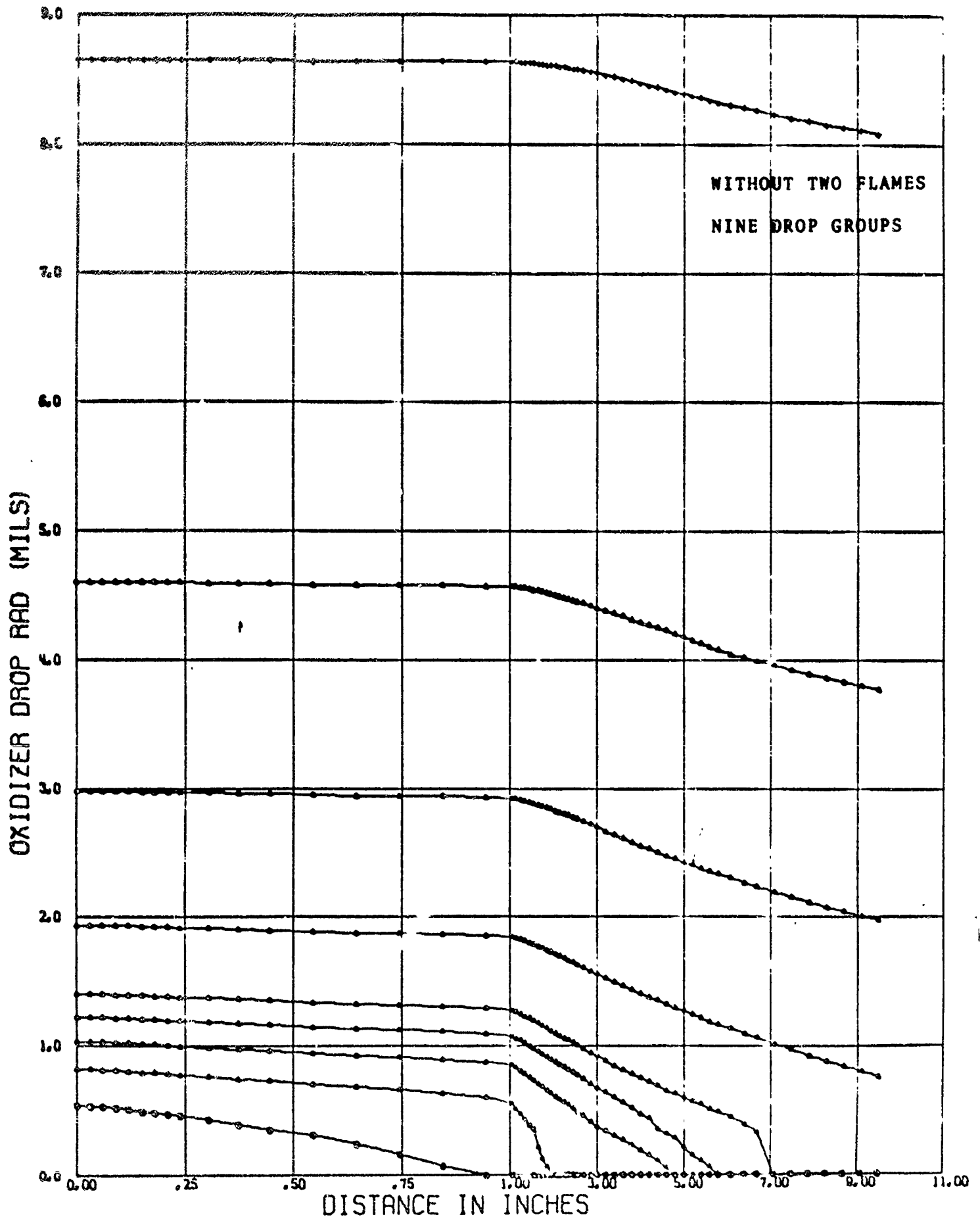


FIGURE 37. Oxidizer Drop Radius (no decomposition flame)

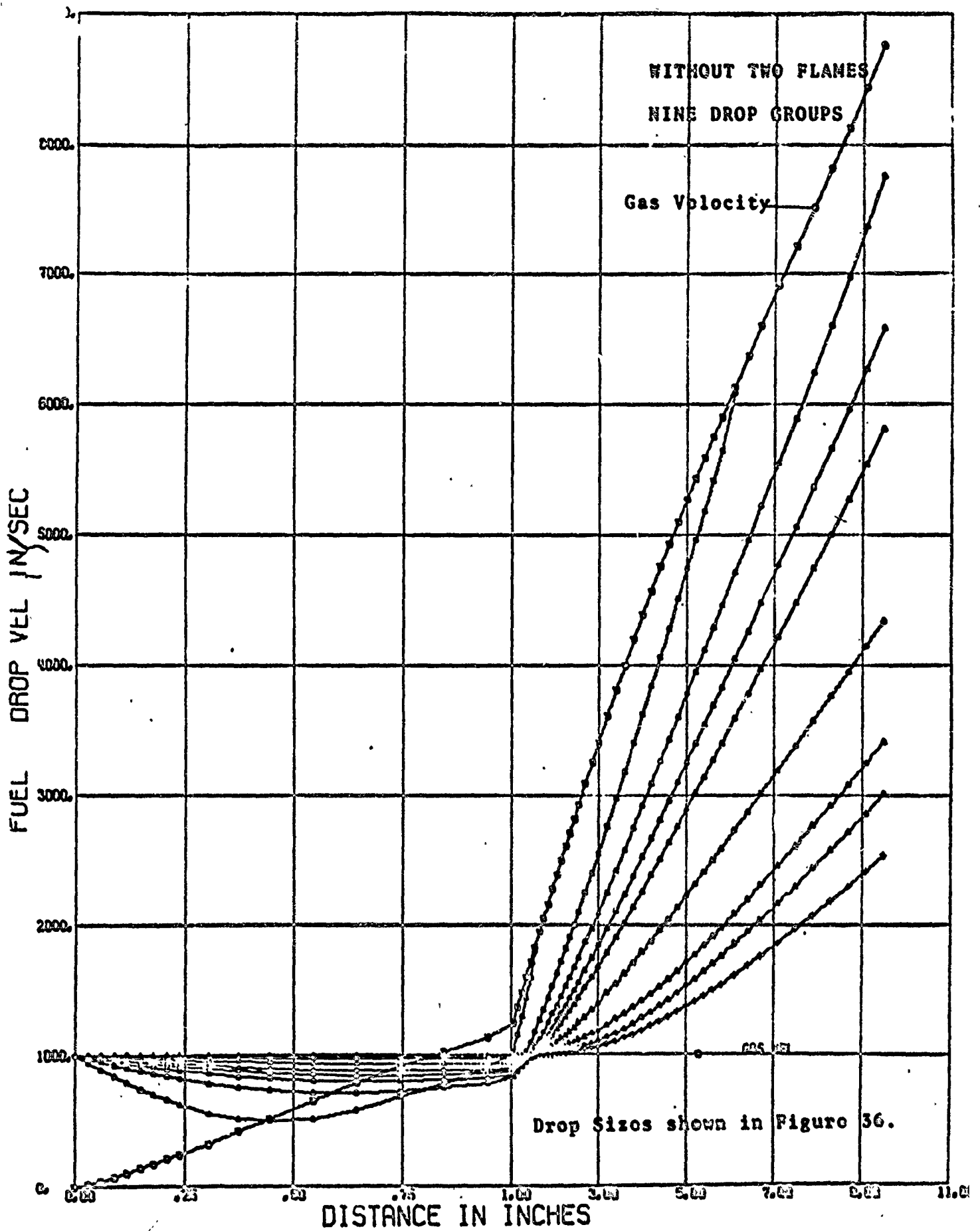


FIGURE 38. Fuel Drop Velocities (no decomposition flame)

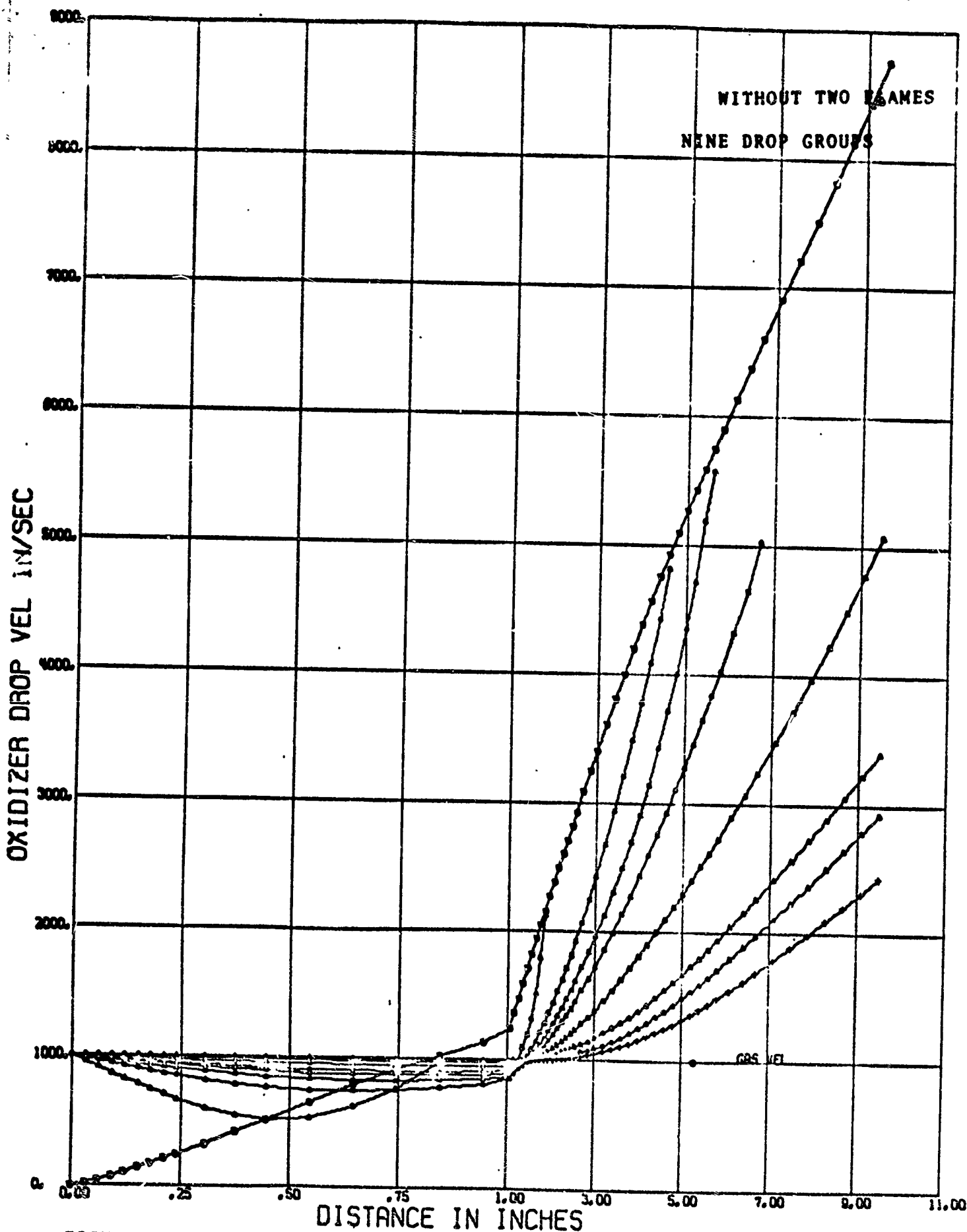


FIGURE C9. Oxidizer Drop Velocities (using decomposition flame model)

Chamber pressure was varied from the base value of 100 psia to 300 and 500 psia. The effects on the fuel and oxidizer vaporization rates are shown in Figures 40 and 41. Increasing the chamber pressure from 100 to 300 psia increases the vaporization rate of the fuel and the oxidizer with the greatest effect being felt by the oxidizer. This can be seen in the plot of O/F ratio shown in Figure 42. Through the sensitive zone (zero relative velocity) the O/F ratio at 100 psia is about 1.0 while at 300 psia it is 1.5. Raising the chamber pressure to 500 psia causes the oxidizer vaporization rate to further increase. At 500 psia the boundary layer thickness over the three smallest drop groups is sufficiently small so that the oxidation and dissociation flames occur at the same position. This means the fastest vaporizing drops are out of the two flame regime and will vaporize correspondingly slower. In Figure 40 the fuel vaporization rate at 500 psia is seen to be lower than at 100 and 300 psia until the smallest drop group [the group controlling the initial vaporization] is consumed. At this distance [$x=0.35$] the drops are in the two flame regime since the boundary layer thickness approaches infinity as the relative velocity approaches zero. Therefore, the fuel vaporization rate undergoes almost a step change, decreasing rapidly at $x=0.40$, as the controlling drop group is consumed. The O/F ratio undergoes large excursions in this region as can be seen in Figure 42. Of particular interest is the fact that the fuel has become the controlling propellant at the sensitive zone. Therefore, increasing operating pressure of the engine can switch control of the combustion process to the fuel.

Varying the mass mean drop size has a large effect on the vaporization rate of both the fuel and the oxidizer. Figures 43 and 44 show the fuel and oxidizer vaporization rates for mass mean drop radii of 25, 75, and 225 sprays. The standard deviation of the distribution was maintained at 2.3. The drop radii and number in the groups describing the sprays are shown in Table III for the 25 μ and 225 μ sprays. The fraction vaporized of the fuel and oxidizer sprays are shown in Figures 45 and 46. The vaporization rate of the 25 μ spray is seen to be much faster than both the 75 μ and 225 μ sprays because of the large numbers of small drops. For reference the variation in the drop radii comprising the fuel spray distributions is shown in Figures 47 and 48 for the 25 μ and 225 μ fuel sprays. The equivalent plots for the oxidizer sprays are shown in Figures 49 and 50. In all three cases the O/F ratio plot [Figure 51] shows the oxidizer to be controlling the combustion process.

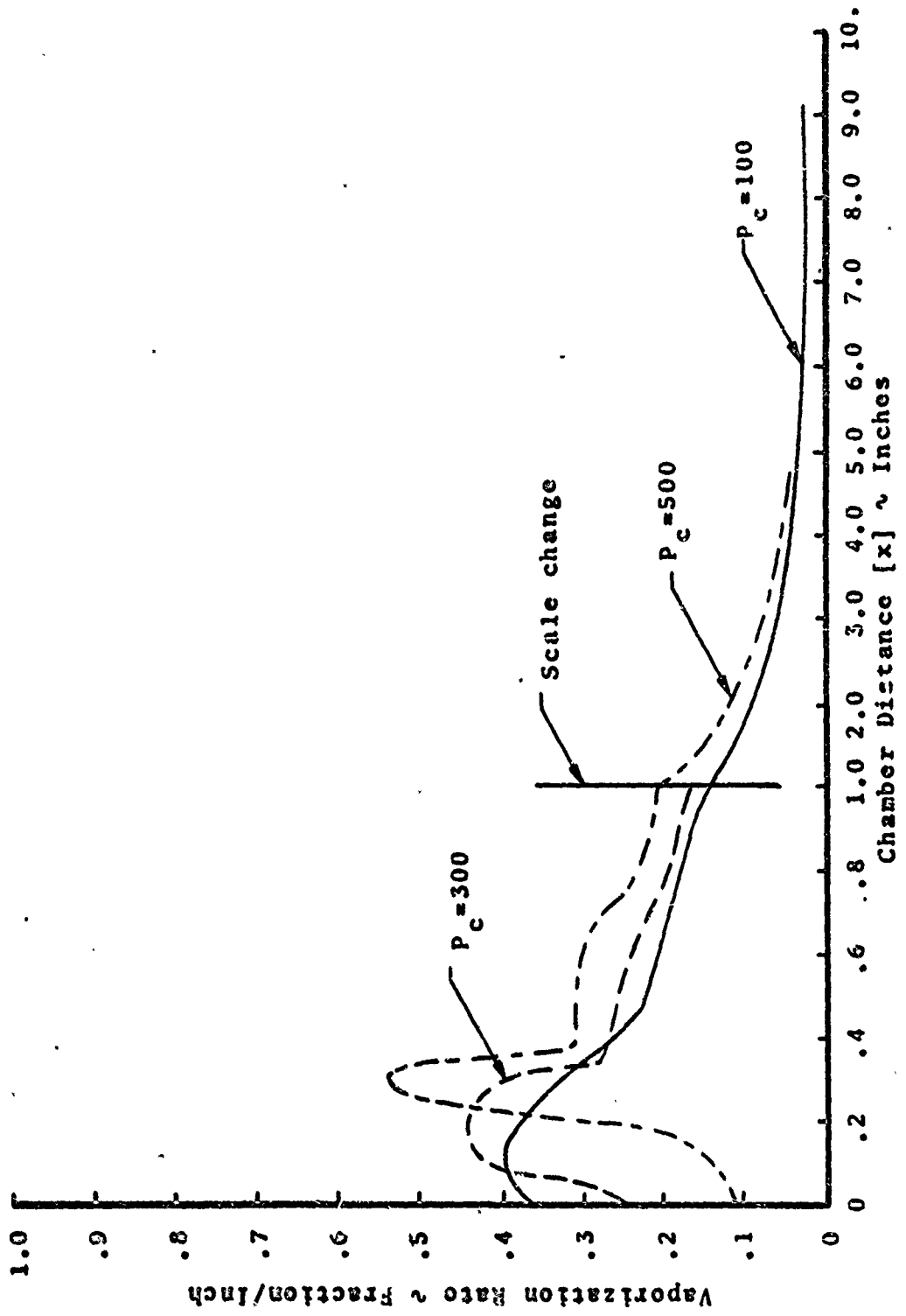


FIGURE 40. Variation of Fuel Vaporization Rate with Chamber Pressure.

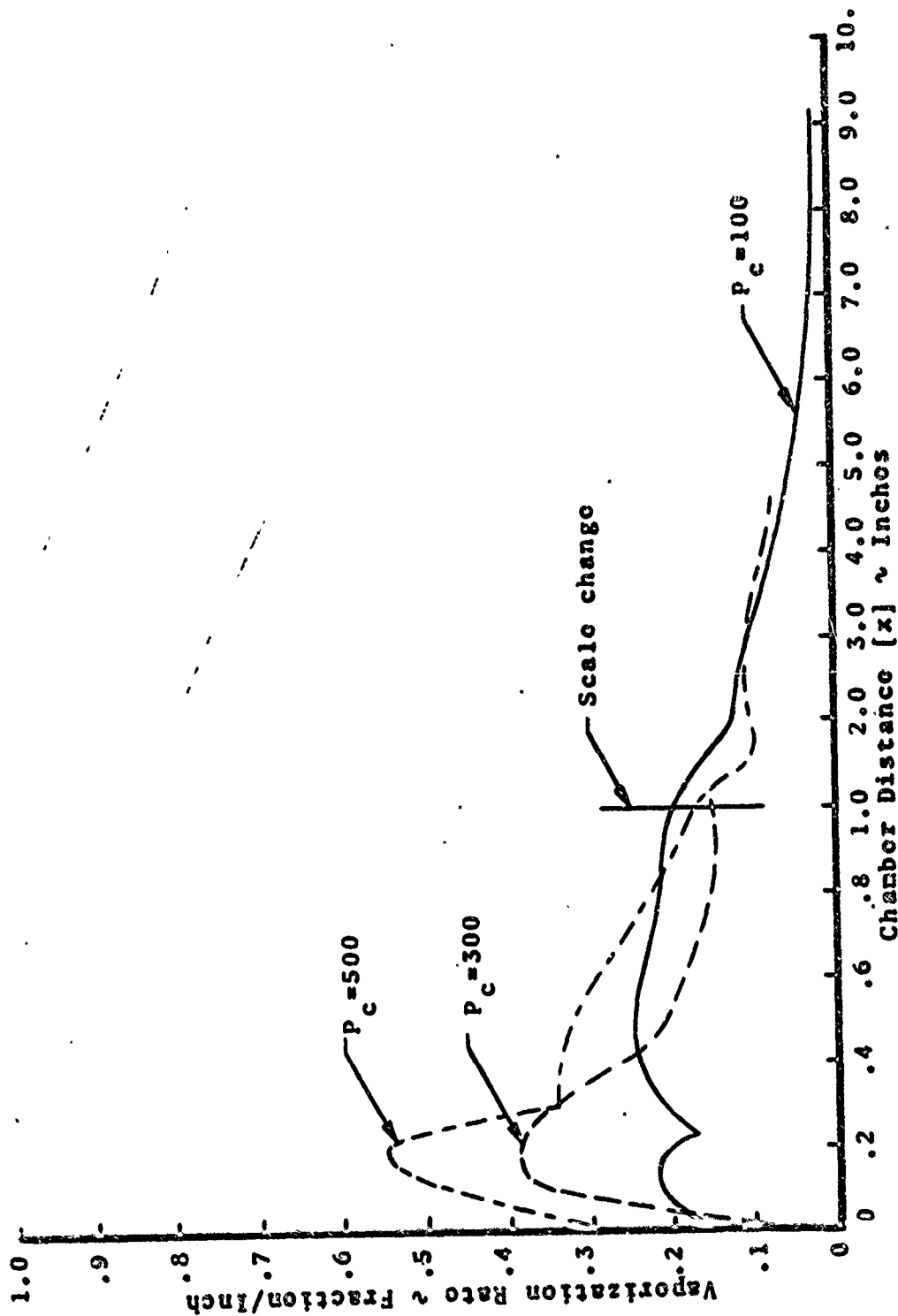


FIGURE 41. Effect of Chamber Pressure on Oxidizer Vaporization Rate.

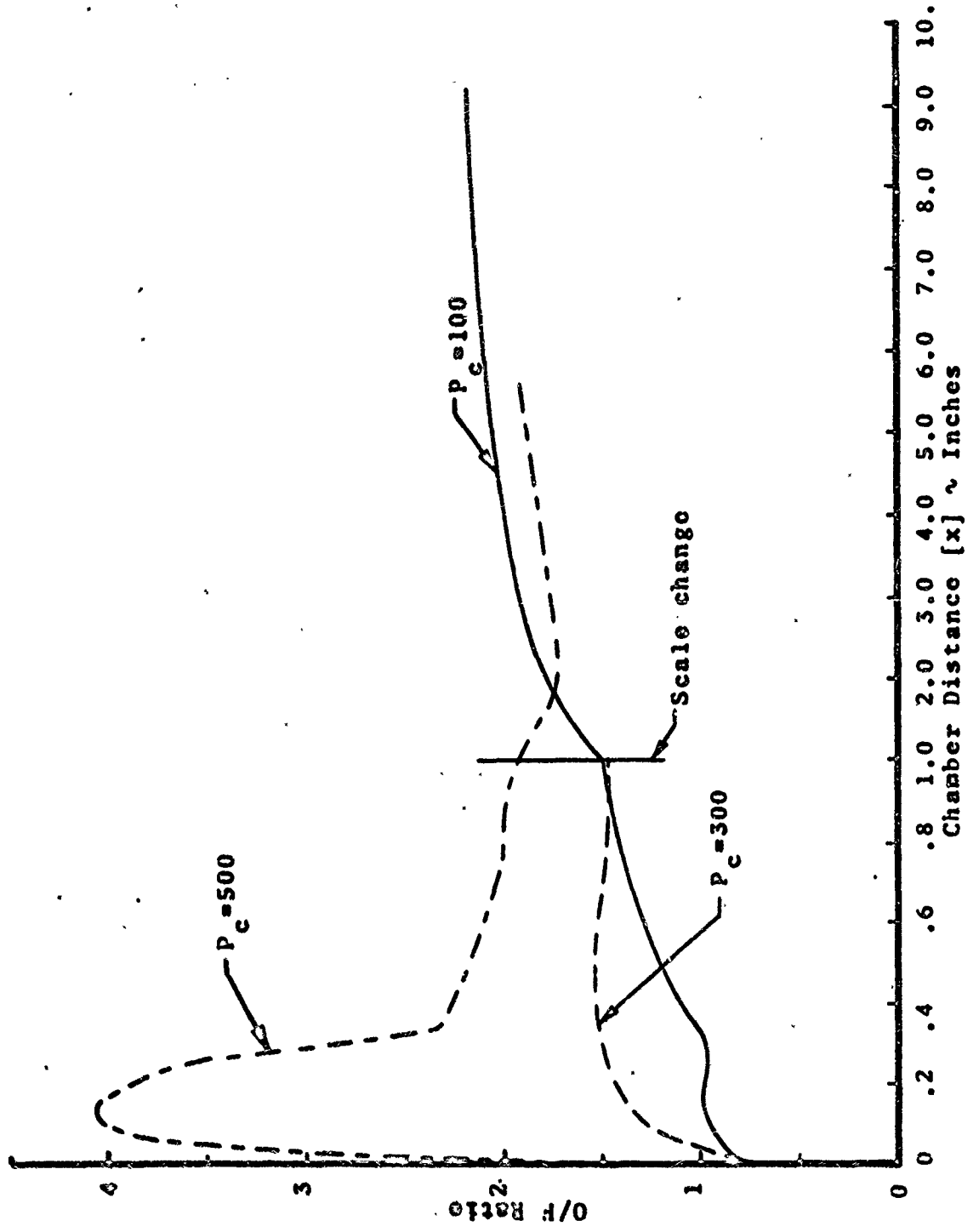


FIGURE 42. Variation of O/F Ratio with Pressure.

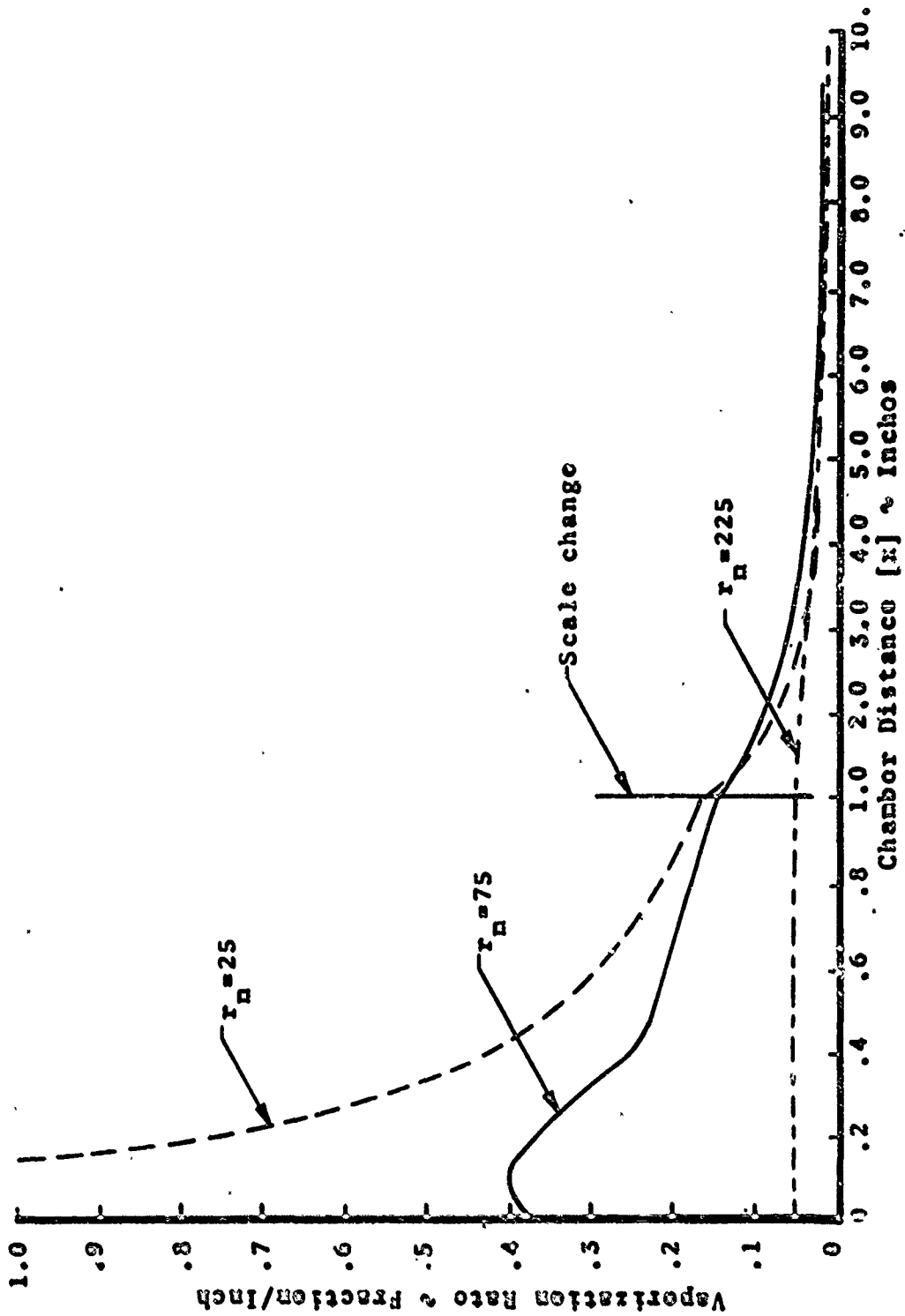


FIGURE 43. Effect of Mass Mean Drop Size on Fuel Vaporization Rate.

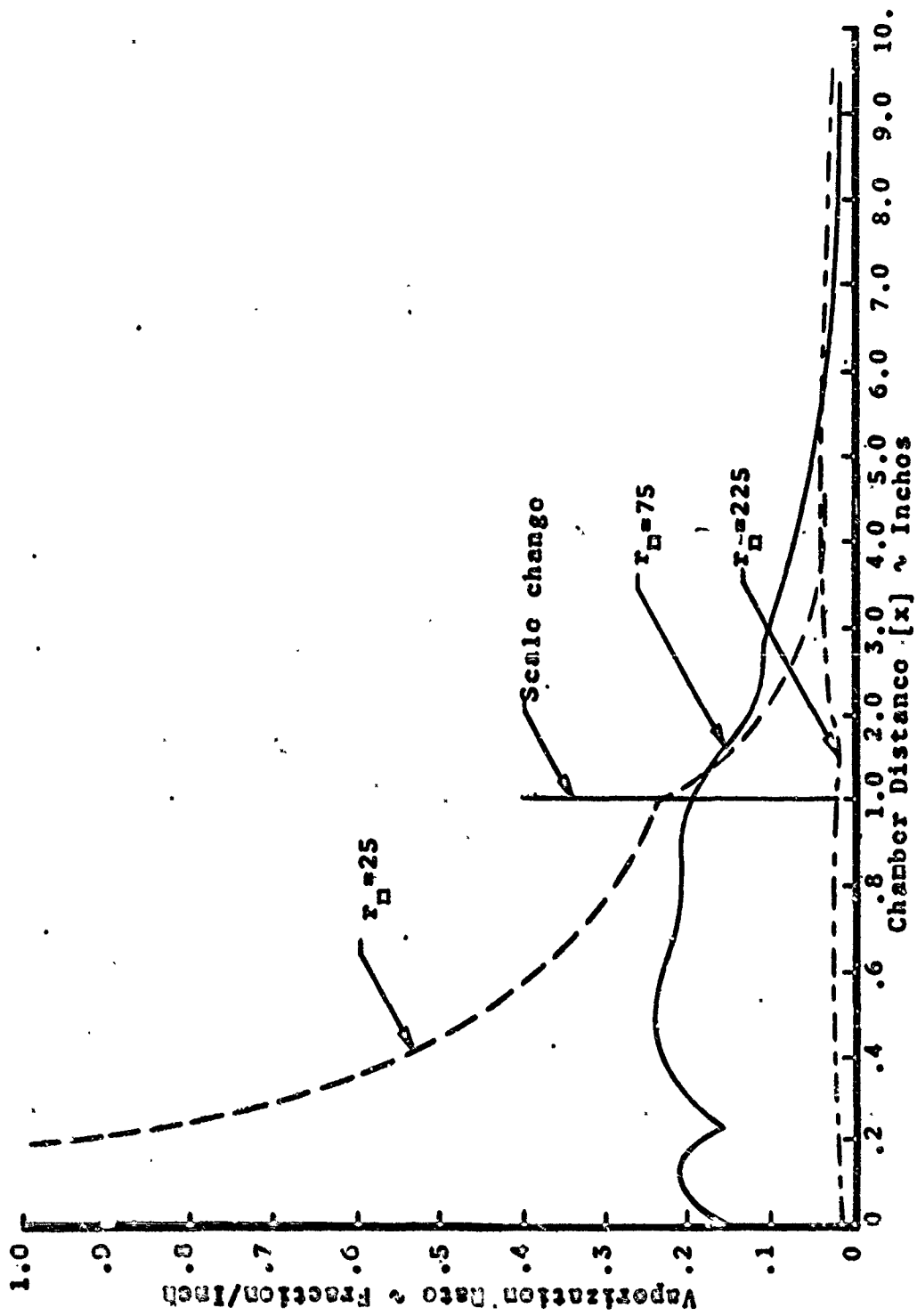


FIGURE 44. Effect of Mass Mean Drop Size on Oxidizer Vaporization Rate.

TABLE III
OXIDIZER SPRAY DISTRIBUTION
 $\sigma=2.3, \dot{m}_O=18. \text{ lb/sec.}$

Group	$r_D = 25\mu$ (.001 in)		$r_D = 225\mu$ (.009 in)	
	Radius (mil)*	Number	Radius (mil)	Number
1	0.1807	4.430×10^{11}	1.6259	6.077×10^8
2	0.2740	1.269×10^{11}	2.4664	1.741×10^8
3	0.3443	6.399×10^{10}	3.0987	8.778×10^7
4	0.4073	3.865×10^{10}	3.6659	5.302×10^7
5	0.4675	2.557×10^{10}	4.2072	3.507×10^7
6	0.6476	4.808×10^{10}	5.8285	6.596×10^7
7	1.0000	1.306×10^{10}	9.0000	1.791×10^7
8	1.5441	3.547×10^9	13.8973	4.866×10^6
9	2.9044	5.330×10^8	26.1397	7.312×10^5

FUEL SPRAY DISTRIBUTION
 $\sigma=2.3, \dot{m}_F=9.0 \text{ lb/sec.}$

Group	$r_D = 25\mu$ (.001 in)		$r_D = 225\mu$ (.009 in)	
	Radius (mil)	Number	Radius (mil)	Number
1	0.1807	2.805×10^{11}	1.6259	3.847×10^8
2	0.2746	8.034×10^{10}	2.4664	1.102×10^8
3	0.3443	4.051×10^{10}	3.0987	5.557×10^7
4	0.4073	2.447×10^{10}	3.6659	3.556×10^7
5	0.4673	1.619×10^{10}	4.2072	2.220×10^7
6	0.6476	3.044×10^{10}	5.8285	4.176×10^7
7	1.0000	8.268×10^9	9.0000	1.134×10^7
8	1.5441	2.246×10^9	13.8973	3.080×10^6
9	2.9044	3.374×10^8	26.1397	4.629×10^5

*1 mil = 25.4 μ

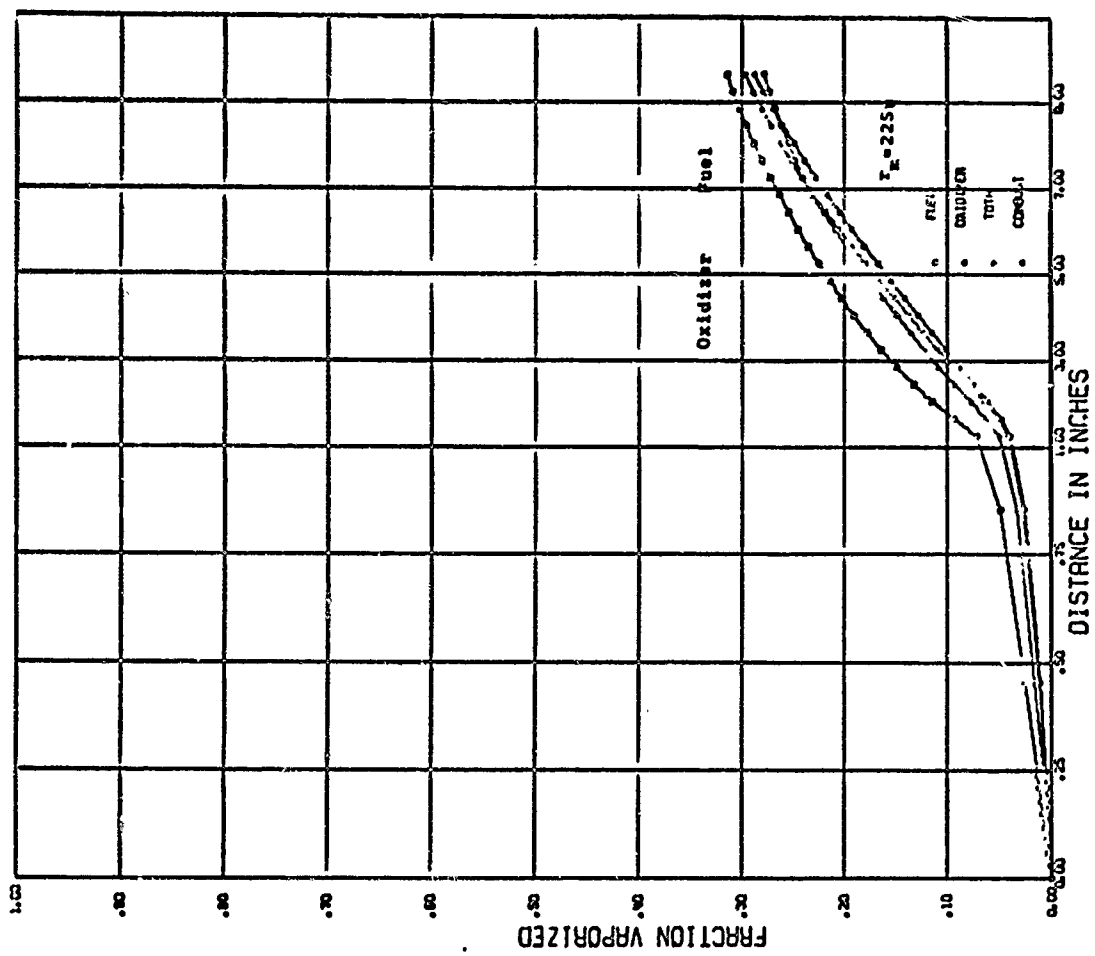


FIGURE 46. Fraction of Spray Vaporized with a Mass Median Drop Size of 225 μ

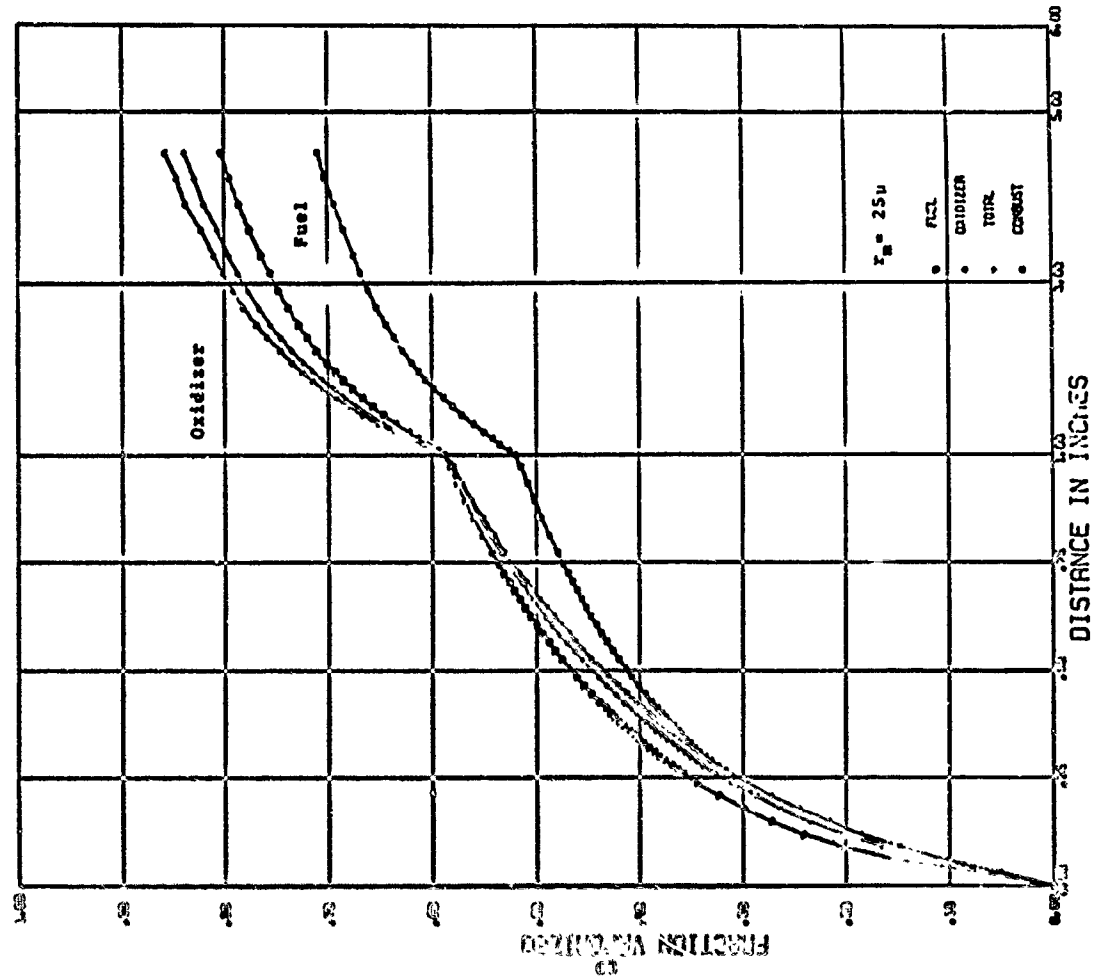


FIGURE 45. Fraction of Spray Vaporized with a Mass Median Drop Size of 25 μ

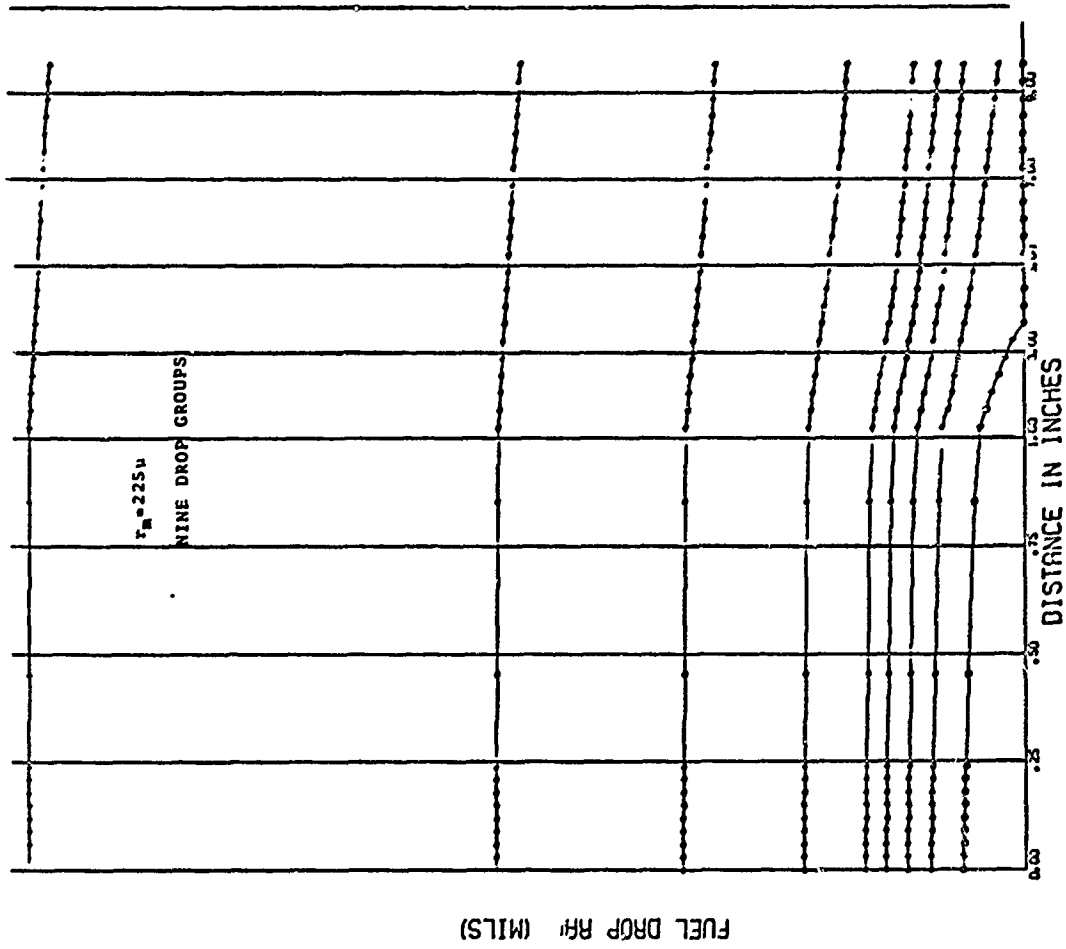


FIGURE 46. Fuel Spray Drop Radii Distribution with a Mass Median Drop Size of 225 μ

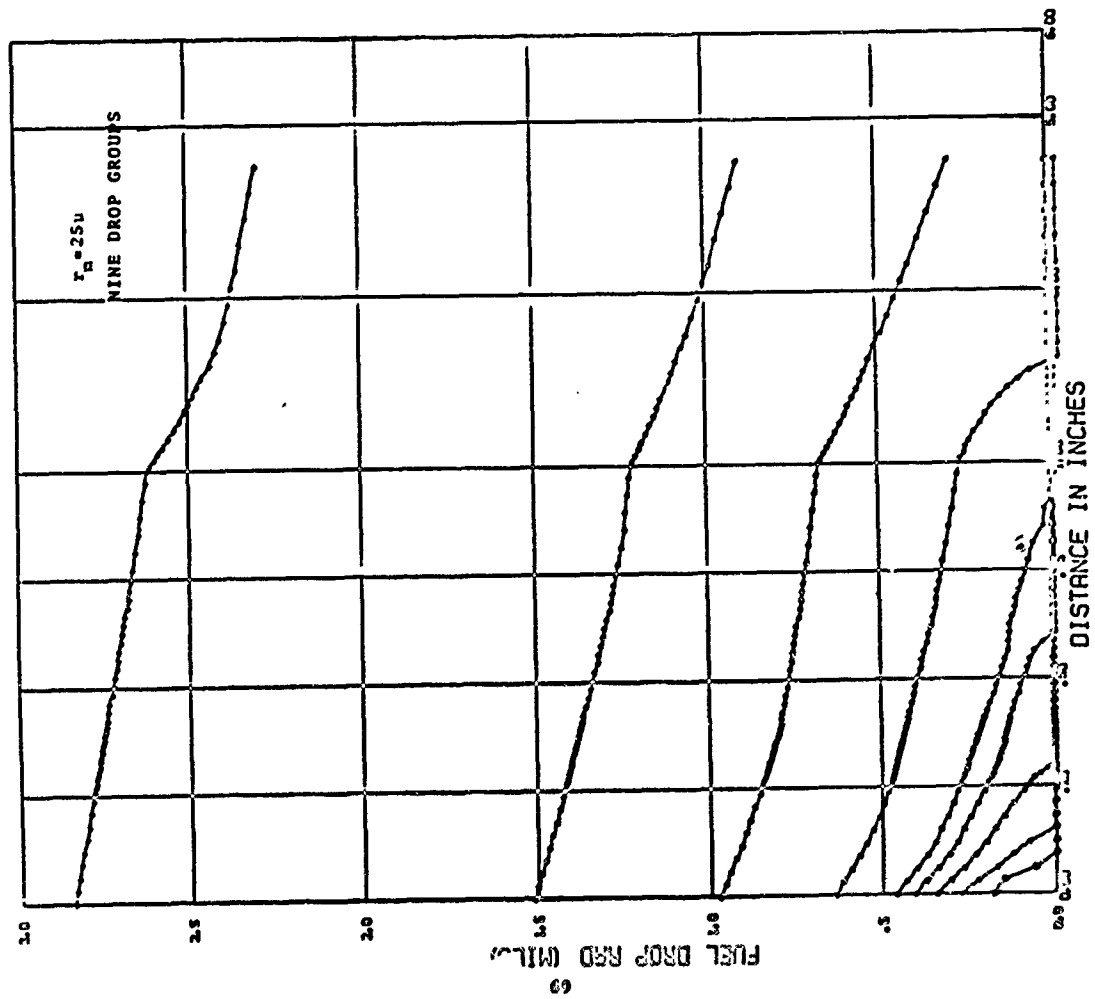


FIGURE 47. Fuel Spray Drop Radii Distribution with a Mass Median Drop Size of 25 μ

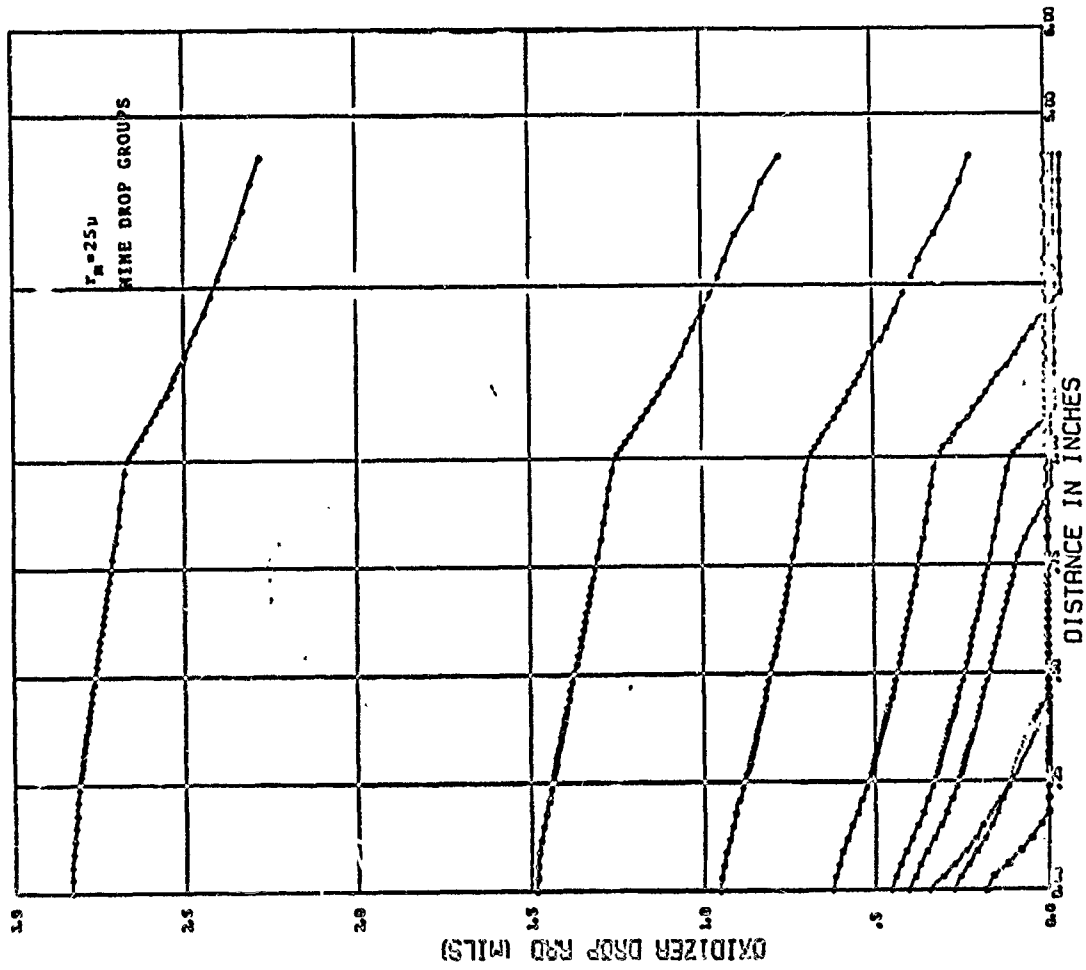


FIGURE 49 Oxidizer Drop Radii Distribution with a Mass Median Drop Size of 25u

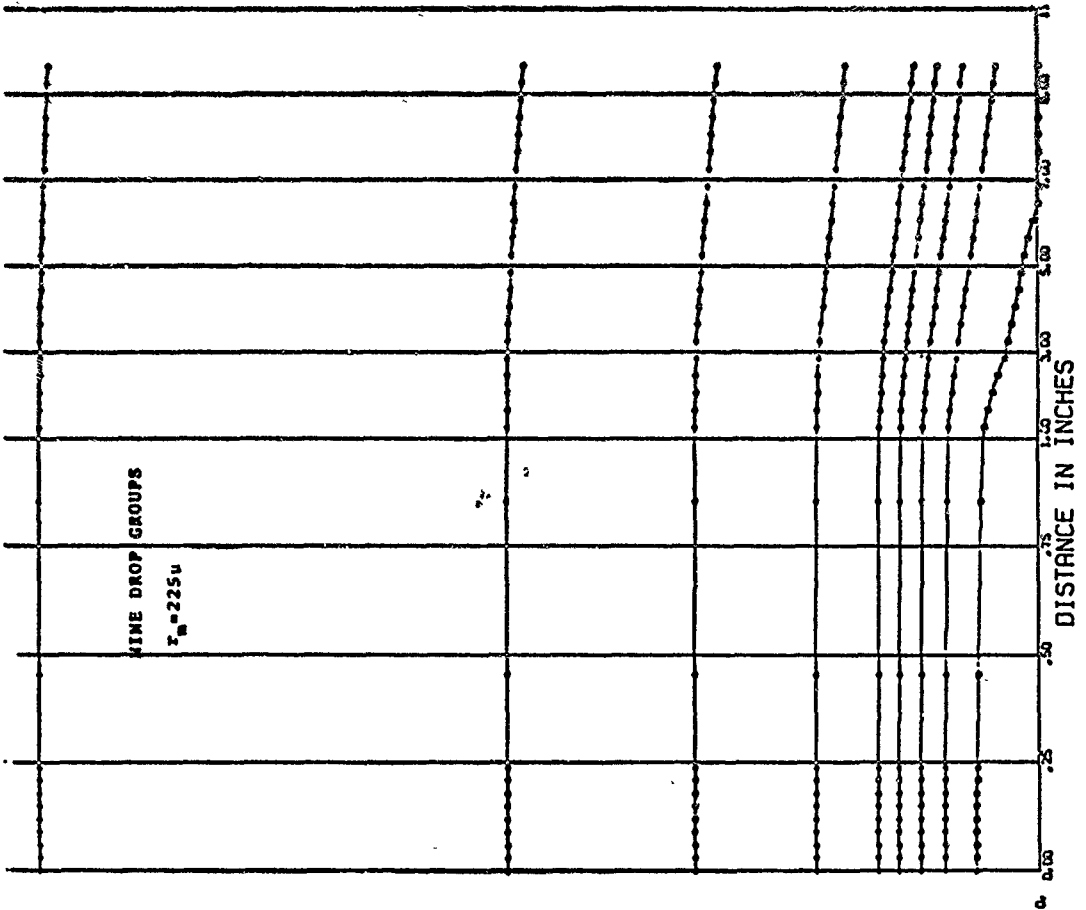


FIGURE 50. Oxidizer Drop Radii Distribution with a Mass Median Drop Size of 225u

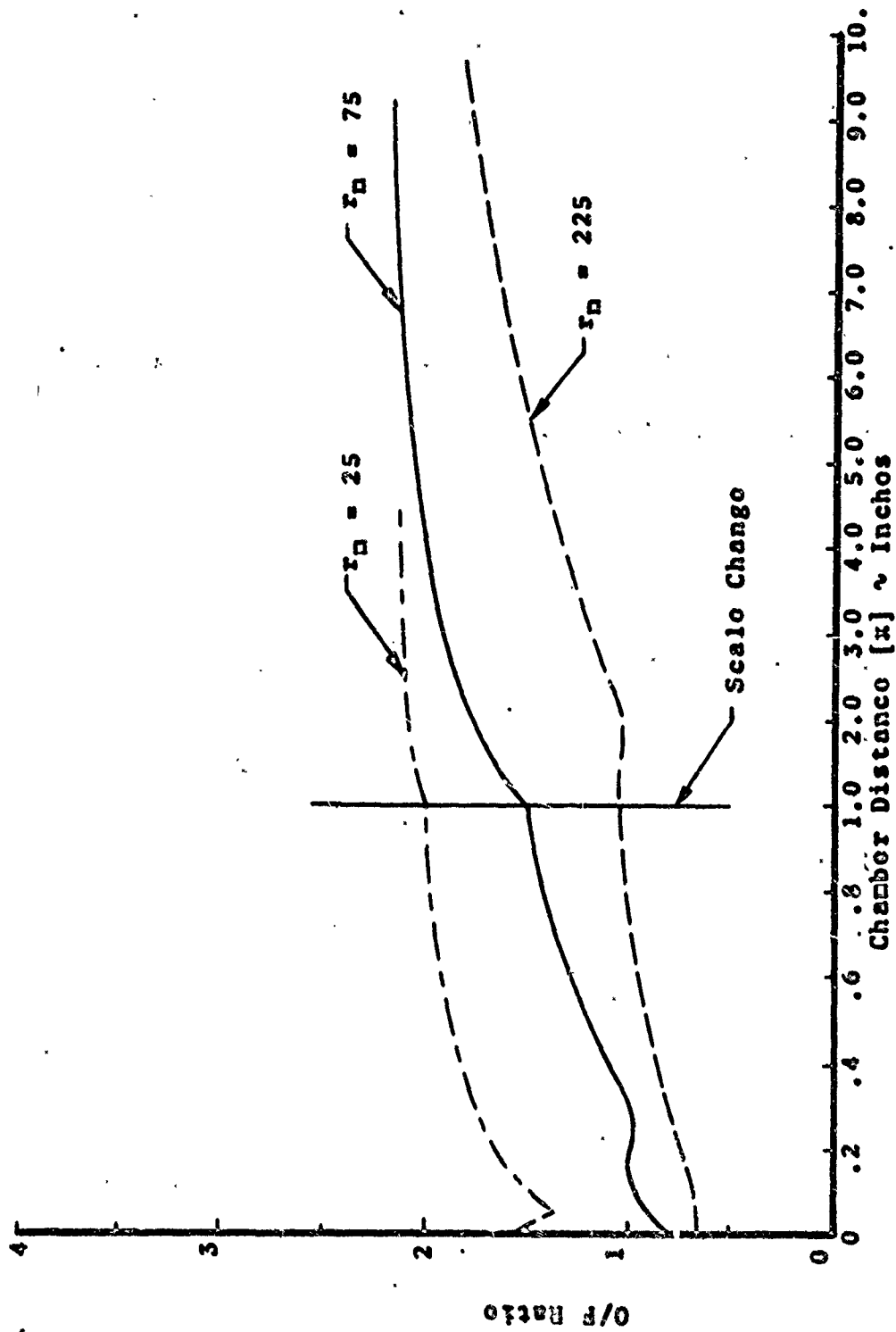


FIGURE 51. Effect of Mass Mean Drop Size of Local O/F Ratio.

The effects of initial drop velocity on the fuel and oxidizer spray vaporization rate are shown in Figures 52 and 53. The injection velocities of the sprays were varied simultaneously around the base value of 100 in/sec. The selected values were 500 and 2000 in/sec. Even at a 2000 in/sec. injection velocity all drops of the fuel distribution were in the two flame burning regime. Increasing the initial velocity causes the vaporization rate to decrease as the drop dwell time in each segment of the chamber is shorter. The machine plots of the fraction of the fuel, oxidizer, and total spray vaporized is shown in Figures 54, 55, and 56 for injection velocities of 500, 1000, and 2000 inches/sec. As an example the oxidizer fraction vaporized at 1.0 inch is .30, .20, and .12 for 500, 1000, and 2000 inch/sec. respectively. The equivalent values for the fuel spray are .34, .27, and .18. The longer dwell time in the chamber distance of 1.0 inches with the 500 inch/sec. injection velocity is reflected by the larger vaporized fraction. Another effect of variation of the injection velocity is the distribution of the zero relative velocity points as the injection velocity is increased. The machine plots of the drop velocities with gas velocity superimposed are shown in Figures 57, 58, and 59 for the oxidizer sprays injected at 500, 1000, and 2000 inch/sec. The corresponding plots for the fuel sprays are shown in Figures 60, 61, and 62. The gas velocity increases sufficiently fast so that all drops go through the zero relative velocity point at approximately 0.10 inches when injected at 500 inches/sec. At this velocity drag is relatively low and the drops go through the zero point [Figures 57 and 60] before slowing down. With an injection velocity of 1000 inches/second the drops go through the zero point [Figures 58 and 61] at 0.20 for the smallest group and 0.25 inches for the largest drops. The distribution still goes through the zero point at relatively the same point. At a 2000 inches/sec. injection velocity, however, Figures 59 and 62 show the smallest drops to go through the sensitive region at 0.60 inches while the largest reaches its zero relative velocity point at 1.0 inches. This effect of a spreading of the sensitive region complicates the calculation of combustion stability by a single drop model and necessitates the determination of an effective drop that characterizes the spray.

In the next set of runs the standard deviation of the drop radii distribution around the 75 μ mean was varied from the base value of 2.3 to values of 4.0 and 1.0. A value of 1.0 proscribes a spray of uniform drops. A summary of the drop radii and number of the groups describing this spray is shown in Table IV. Once again the first five groups of the distribution represents 20% of the mass. The effect of standard

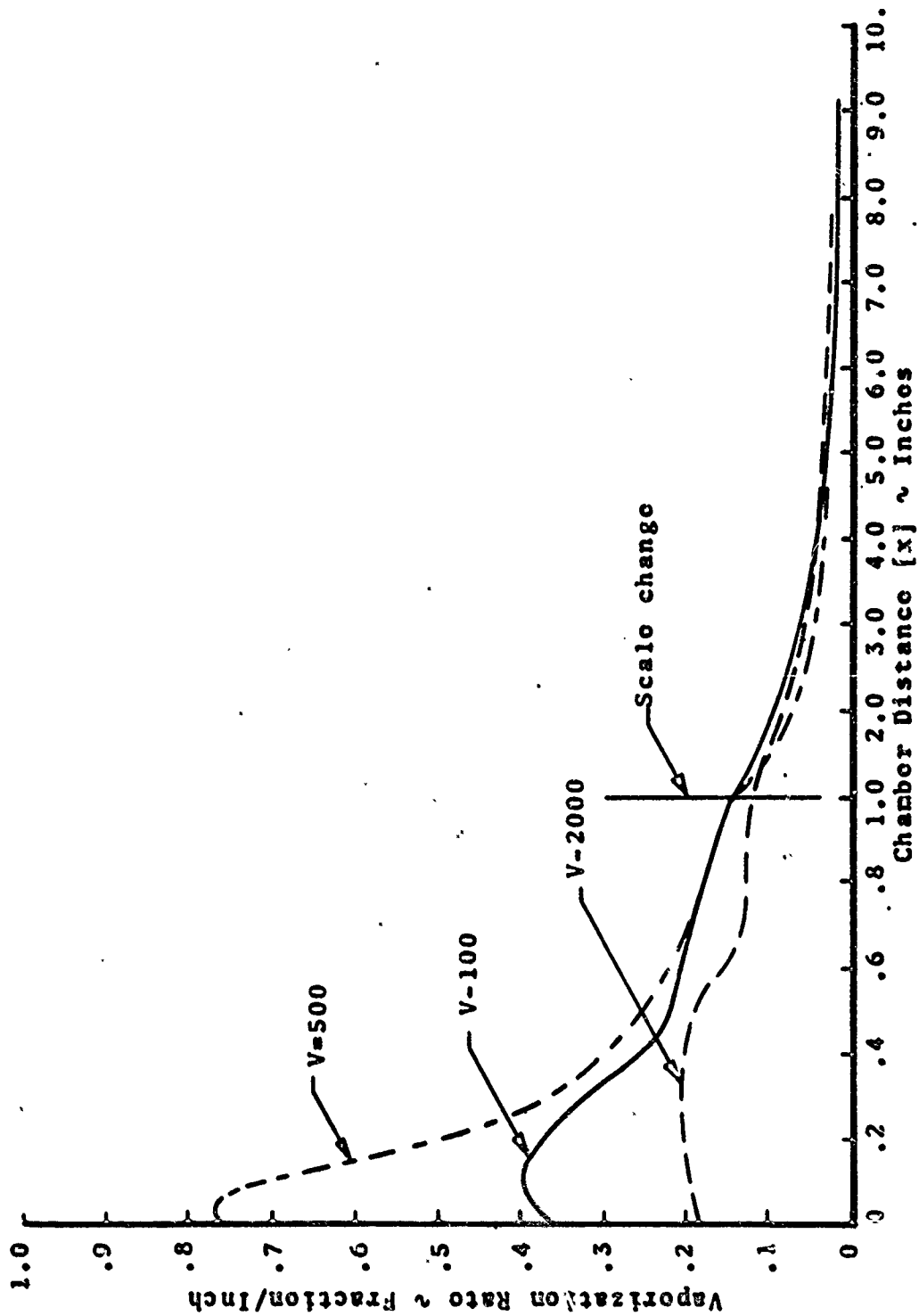


FIGURE 52. Variation of Fuel Vaporization Rate with Spray Injection Velocity.

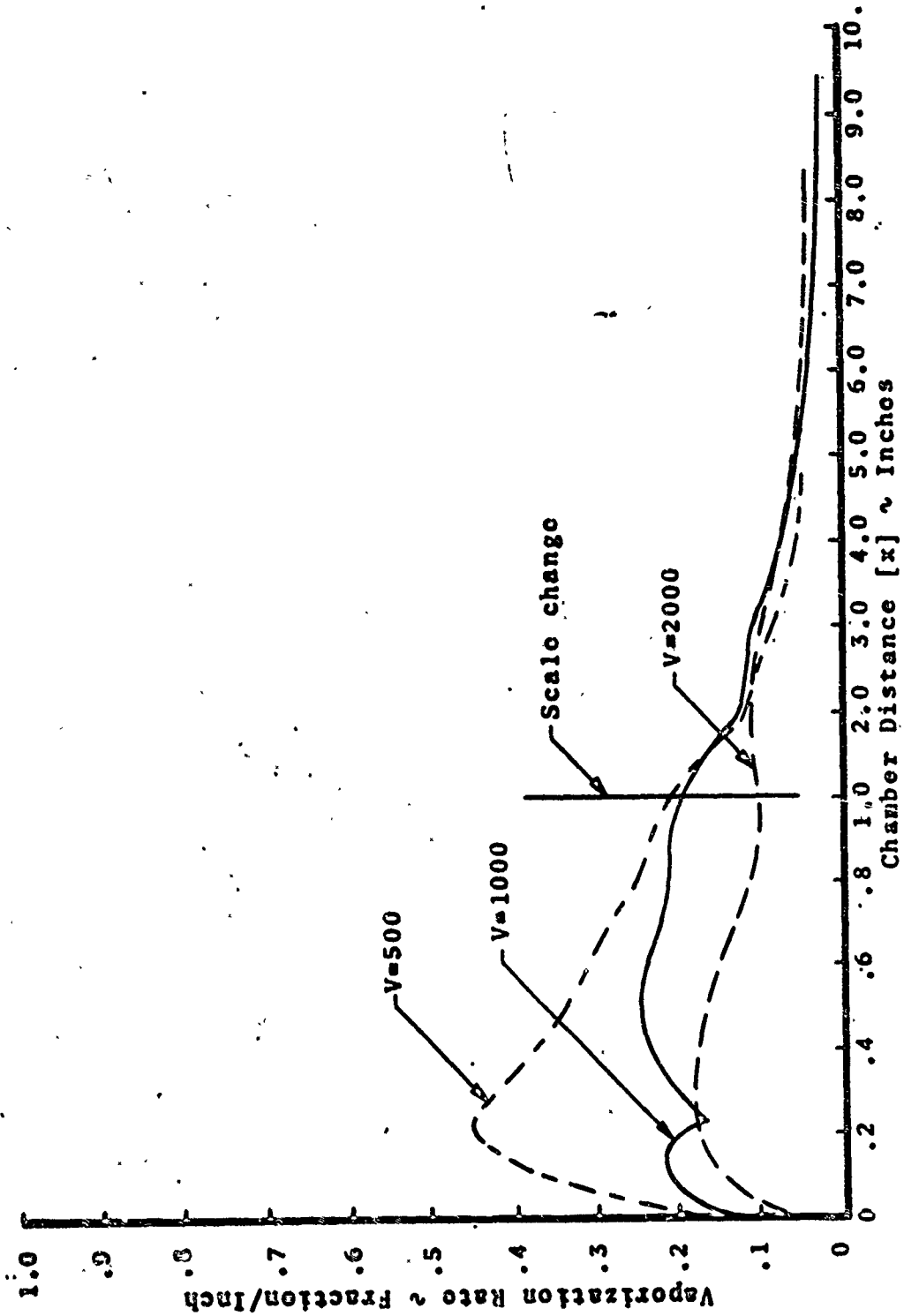


FIGURE 53. Variation of Oxidizer Vaporization Rate with Injection Velocity.

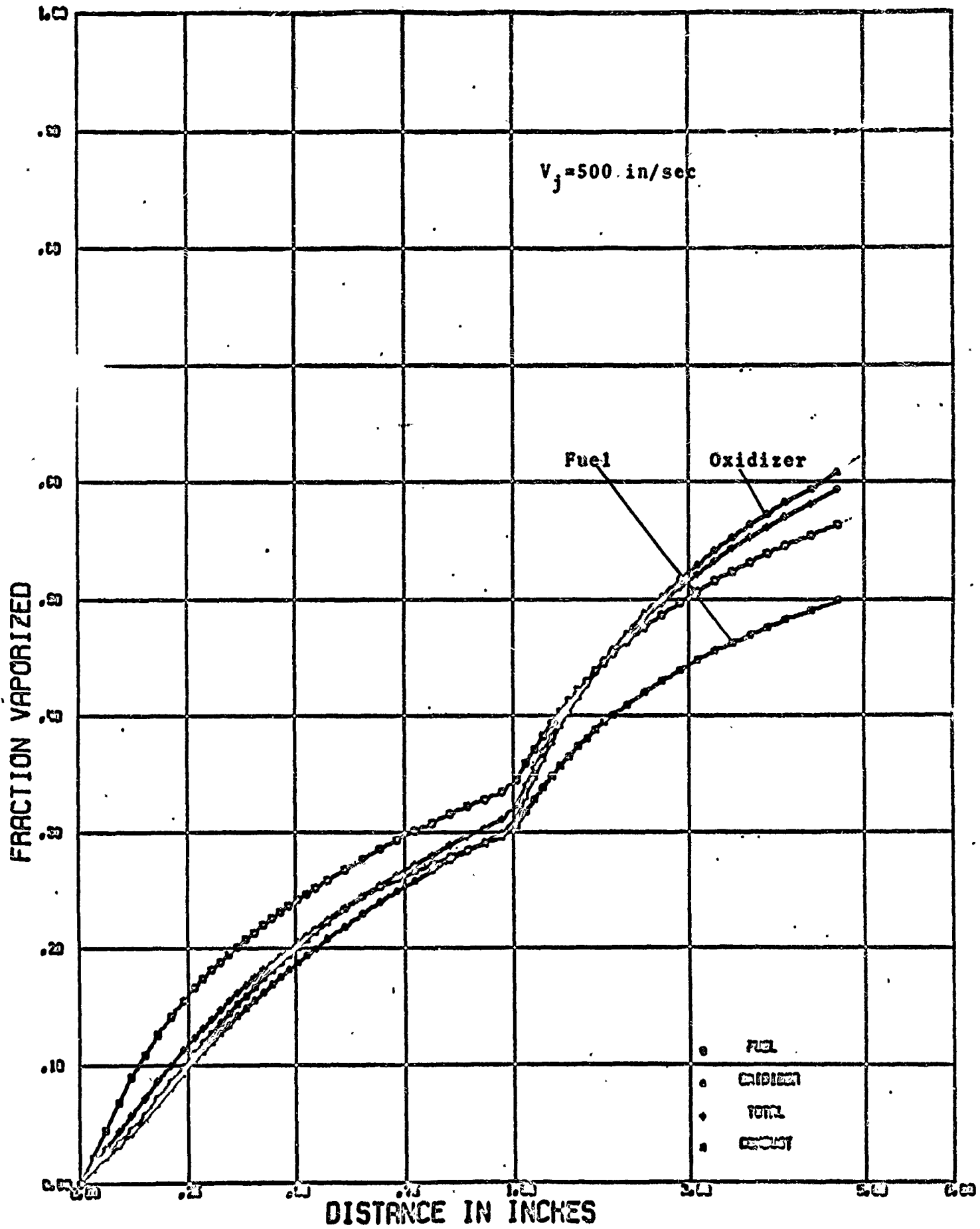


FIGURE 54. Fraction of Spray Vaporized with An Injection Velocity of 500 in/sec.

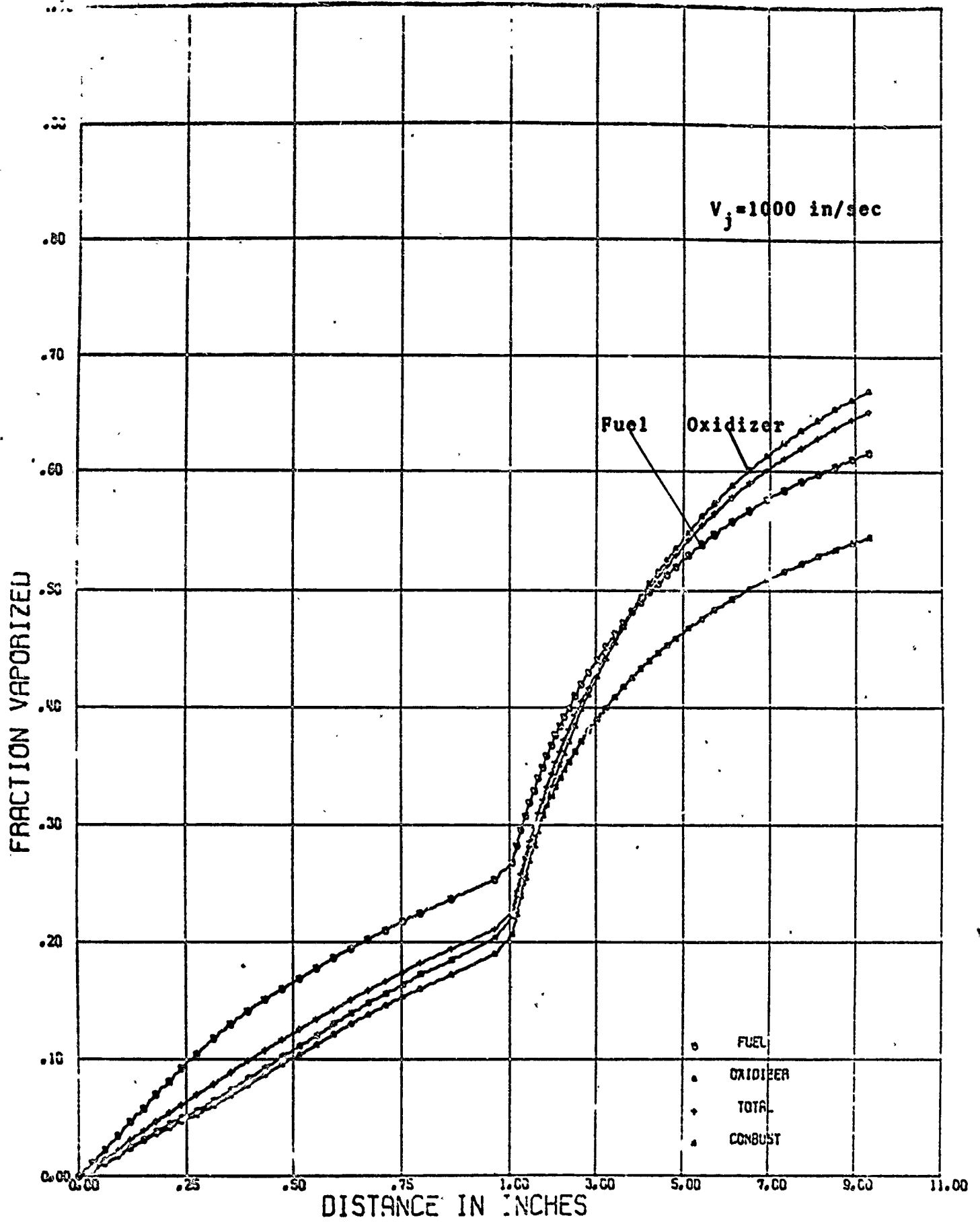


FIGURE 55. Fraction of Spray Vaporized with An Injection Velocity of 1000 in/sec

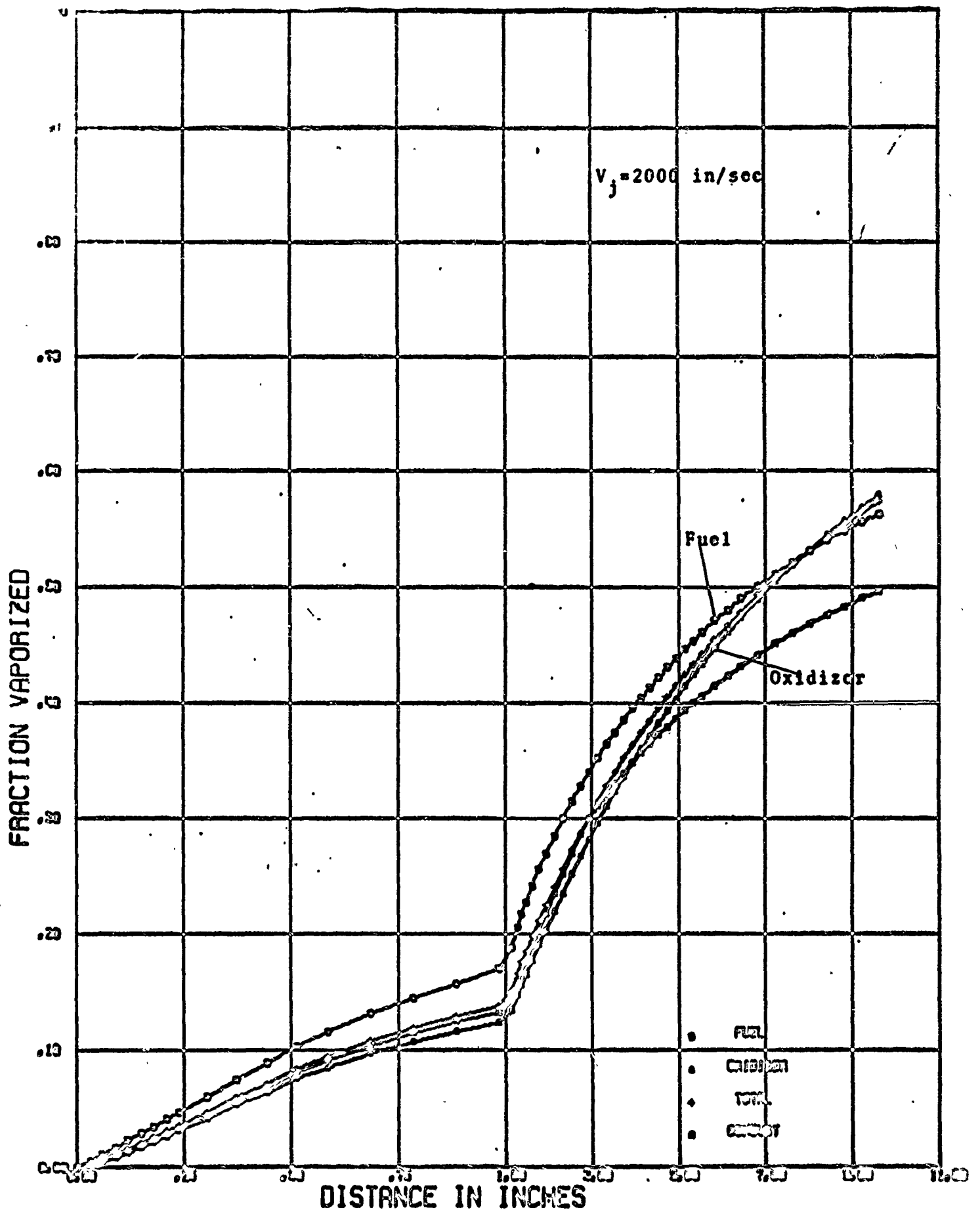


FIGURE 56. Fraction of Spray Vaporized with An Injection Velocity of 2000 in/sec

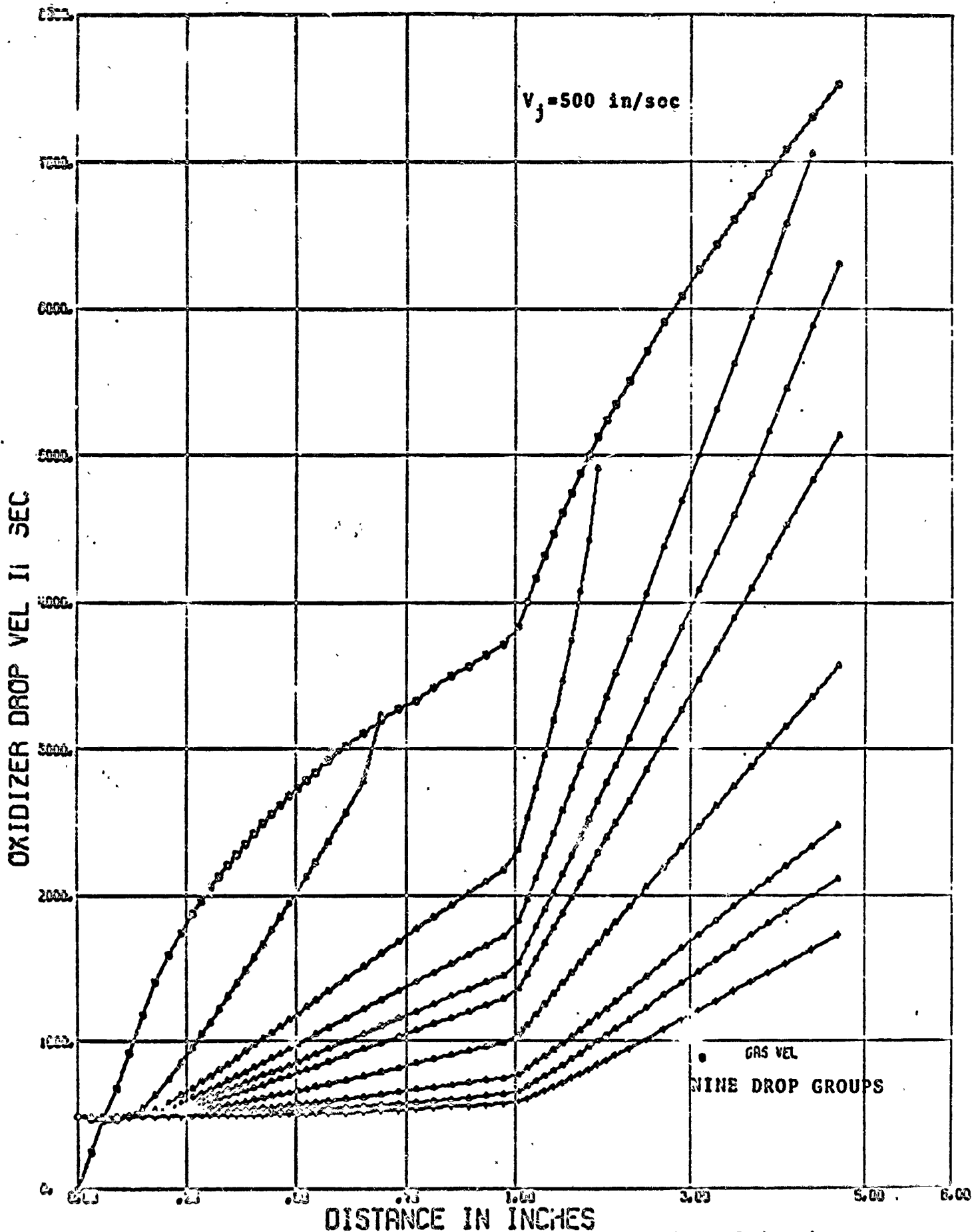


FIGURE 57. Oxidizer Spray Drop Velocities with An Injection Velocity of 500/in/sec.

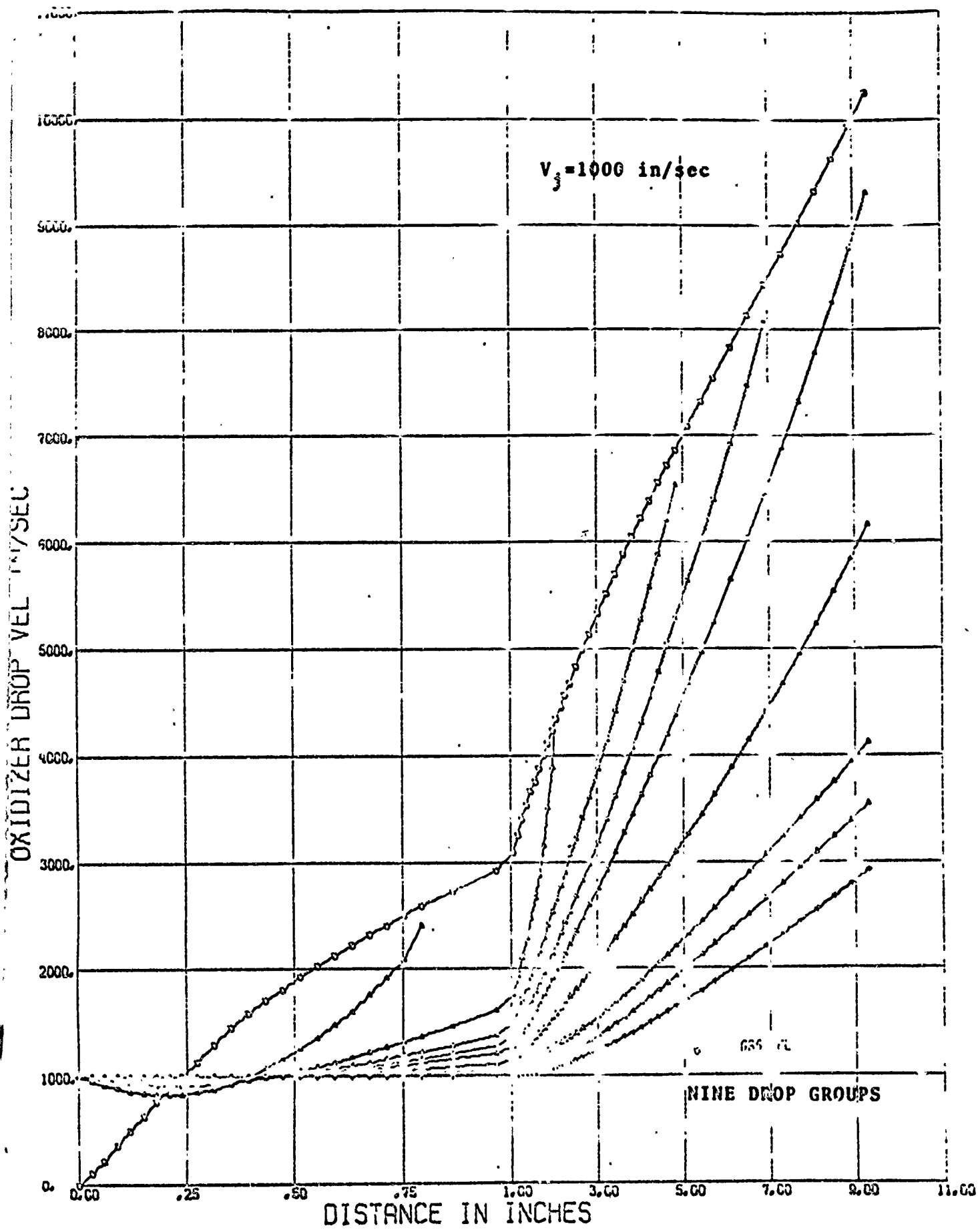


FIGURE 58. Oxidizer Spray Drop Velocities with an Injection Velocity of 1000 in/sec.

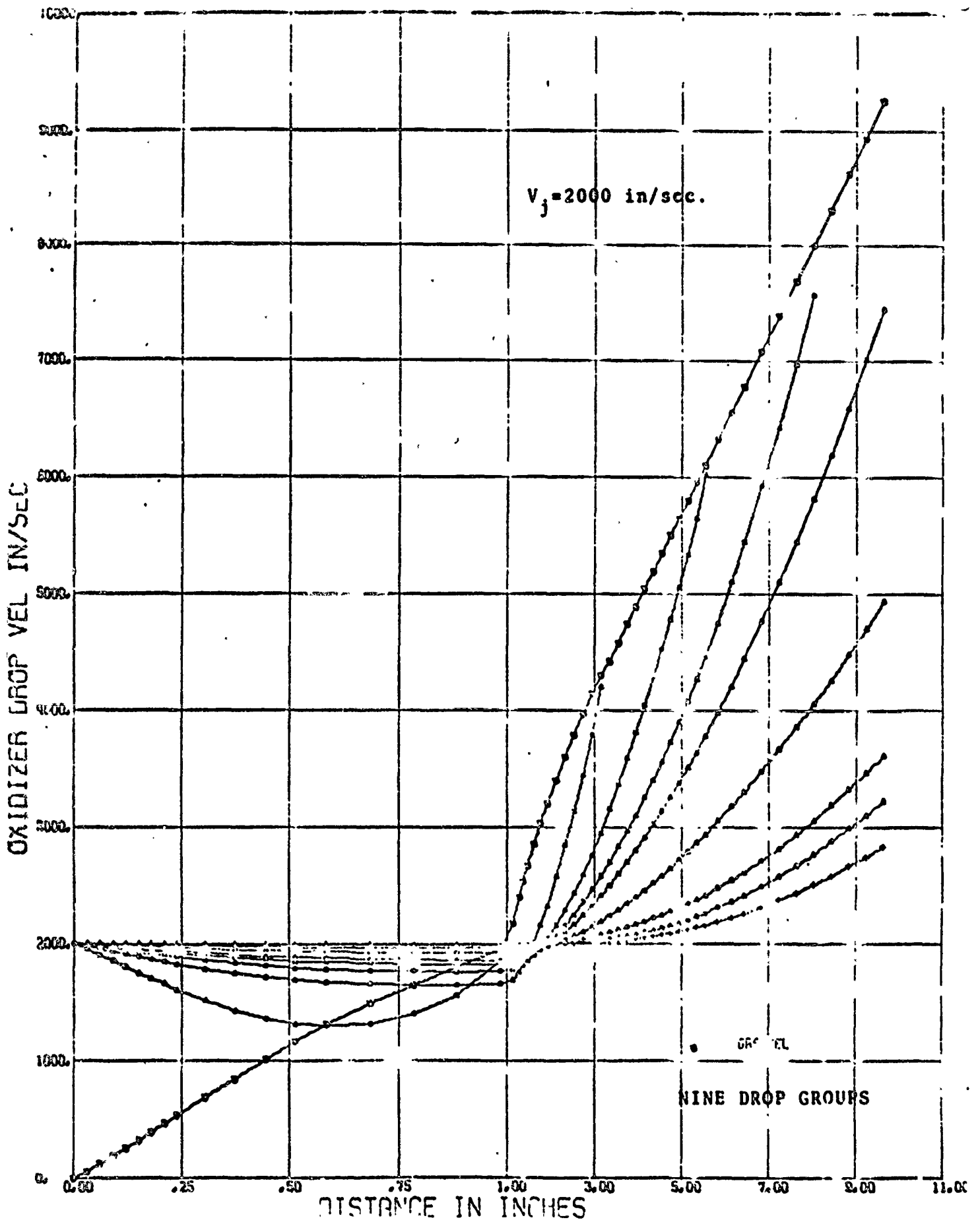


FIGURE 59. Oxidizer Spray Drop Velocities with an Injection Velocity of 2000 in/sec.

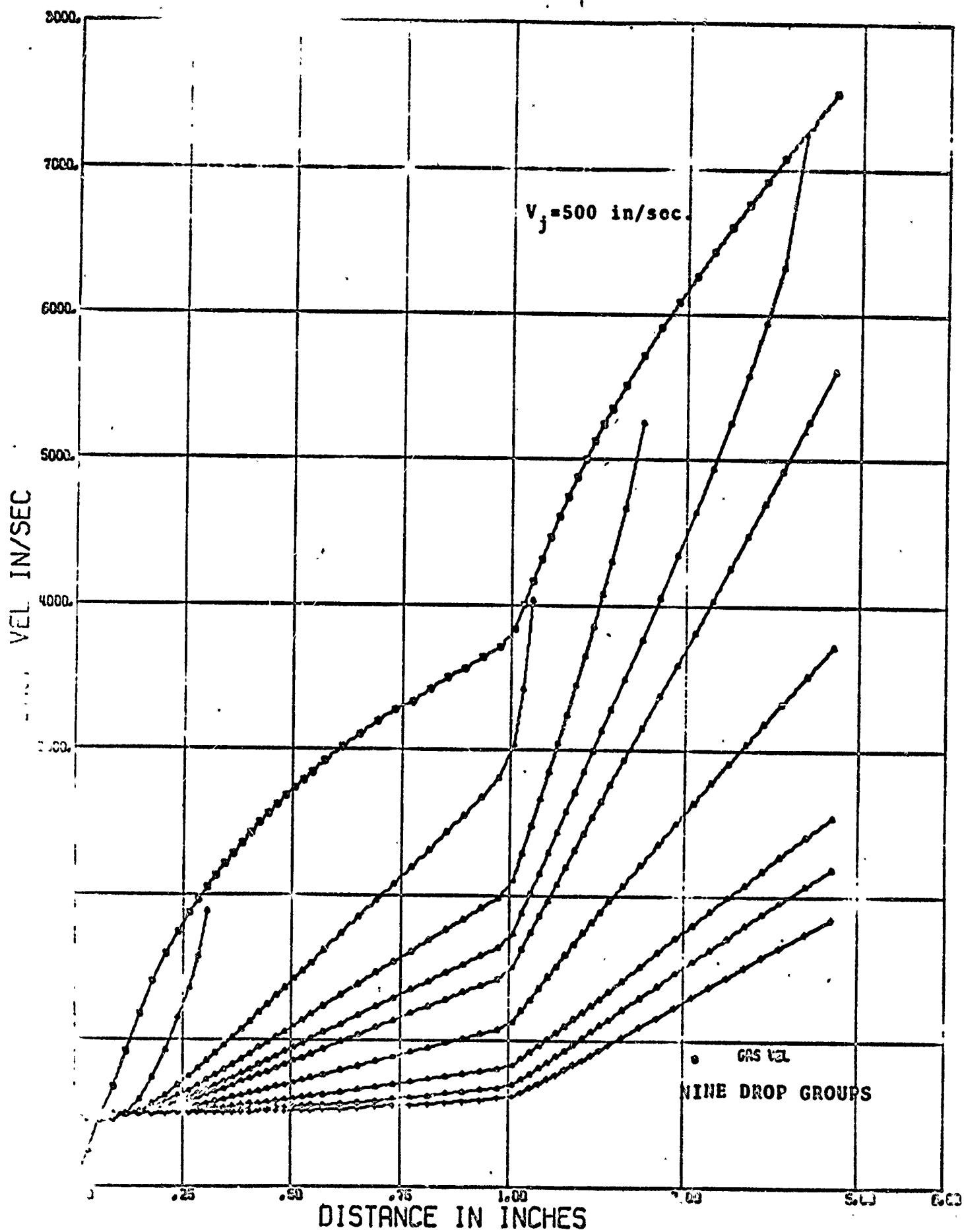


FIGURE 60. Fuel Spray Drop Velocities with an Injection Velocity of 500 in/sec.

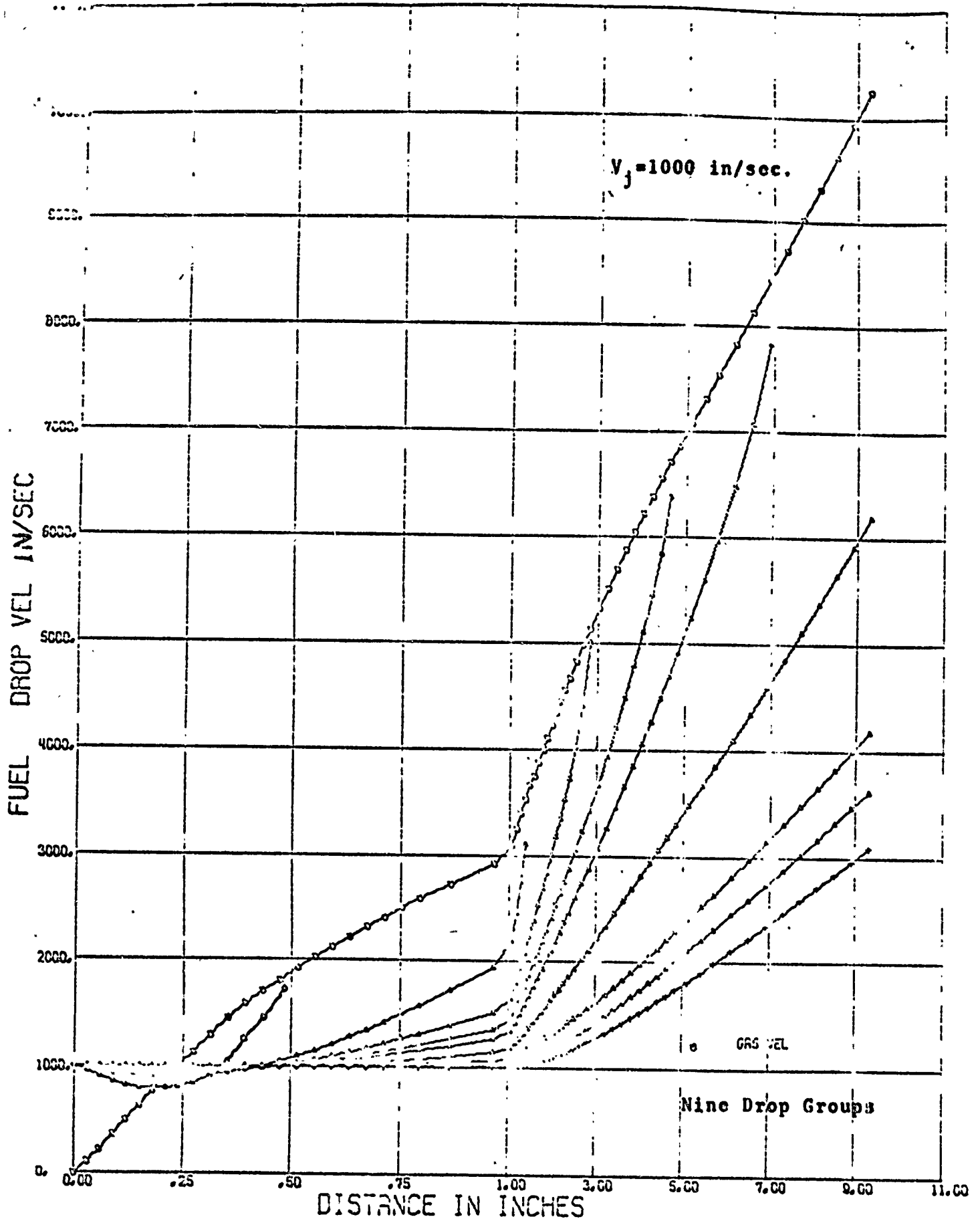


FIGURE 61. Fuel Spray Drop Velocities with an Injection Velocity of 1000 in/sec.

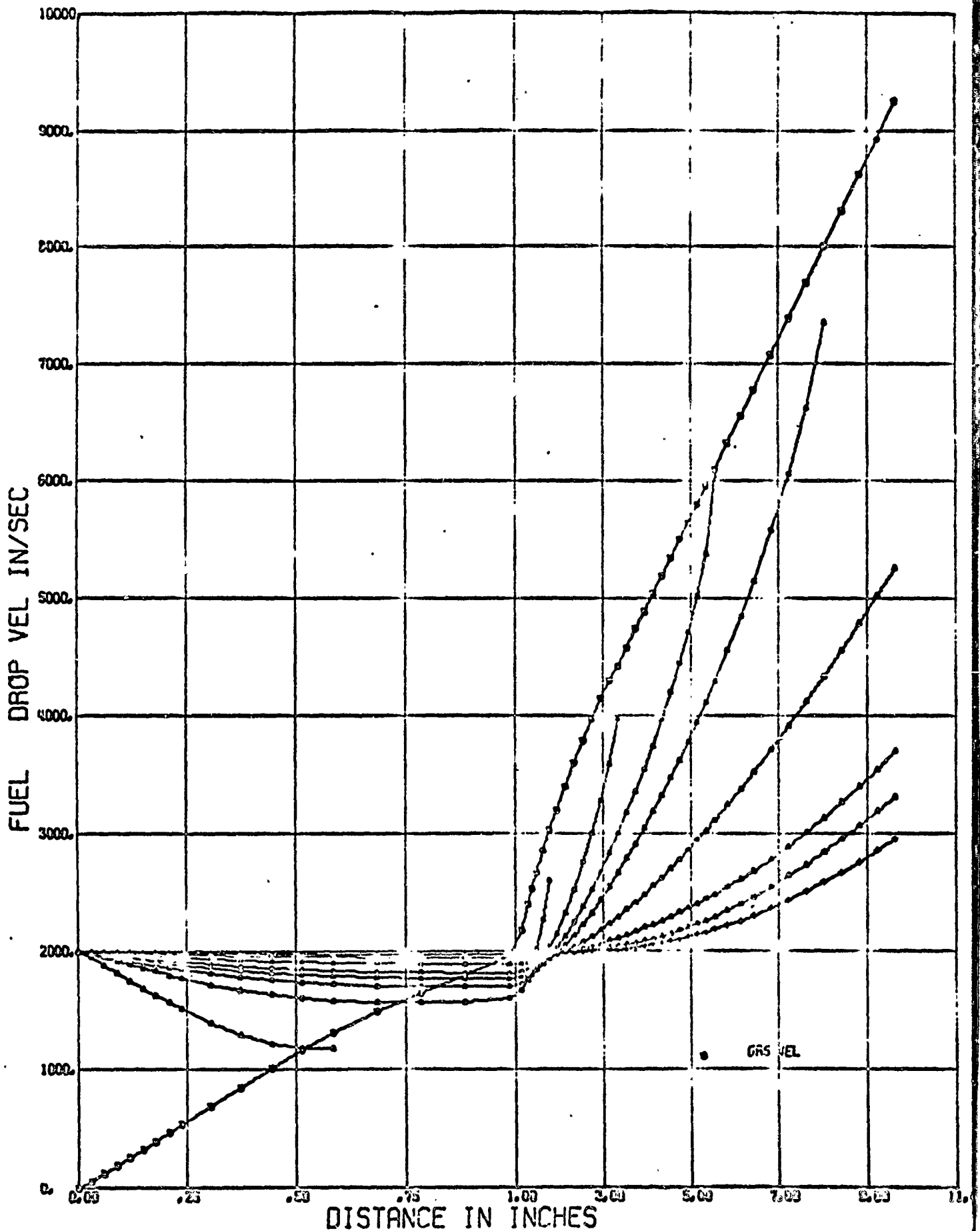


FIGURE 62. Fuel Spray Drop Velocities with an Injection Velocity of 2000 in/sec.

TABLE IV

OXIDIZER SPRAY DISTRIBUTION
 $r_D = 75\mu (.003 \text{ in}), \dot{m}_O = 18. \text{ lb/sec.}$

Group	$\sigma = 4.0$		$\sigma = 1.0$	
	Radius (mil)	Number/Sec.	Radius (mil)	Number
1	0.1739	4.970×10^{11}	3.000	9.674×10^7
2	0.3479	6.204×10^{10}	↓	↓
3	0.5086	1.985×10^9		
4	0.6728	8.575×10^9		
5	0.8462	4.311×10^9		
6	1.4557	4.234×10^9		
7	3.0000	4.837×10^8		
8	6.1827	5.526×10^7		
9	17.6943	2.357×10^6		

FUEL SPRAY DISTRIBUTION

$r_D = 75\mu (.003 \text{ in}), \dot{m}_F = 9.0 \text{ lb/sec.}$

Group	$\sigma = 4.0$		$\sigma = 1.0$	
	Radius (mil)	Number	Radius (mil)	Number
1	0.1739	3.146×10^{11}	3.000	6.124×10^7
2	0.3479	3.928×10^{10}	↓	↓
3	0.5086	1.257×10^{10}		
4	0.6728	5.429×10^9		
5	0.8462w	2.729×10^9		
6	1.4557	2.680×10^9		
7	3.0000	3.062×10^8		
8	6.1827	3.498×10^7		
9	17.6943	1.492×10^6		

deviation on the vaporization rate of the total fuel and oxidizer spray is shown in Figures 63 and 64. With a standard deviation of 4.0 the radii distribution is spread out making more small drops. Therefore, the initial vaporization rate is much higher for this case. As the smaller drops are consumed, however, the rates approach each other since the larger drops become controlling. The fuel vaporization rate with the deviation of 1.0 is relatively constant as can be seen in Figure 63. The calculated variation of the local O/F with distance down the chamber is shown in Figure 65. It is seen that the oxidizer is controlling for approximately 4.0 inches. Large differences in the spray fraction vaporized are noted between these runs out to a chamber distance of about 2 inches. After this length the standard deviation has little effect on the fraction vaporized.

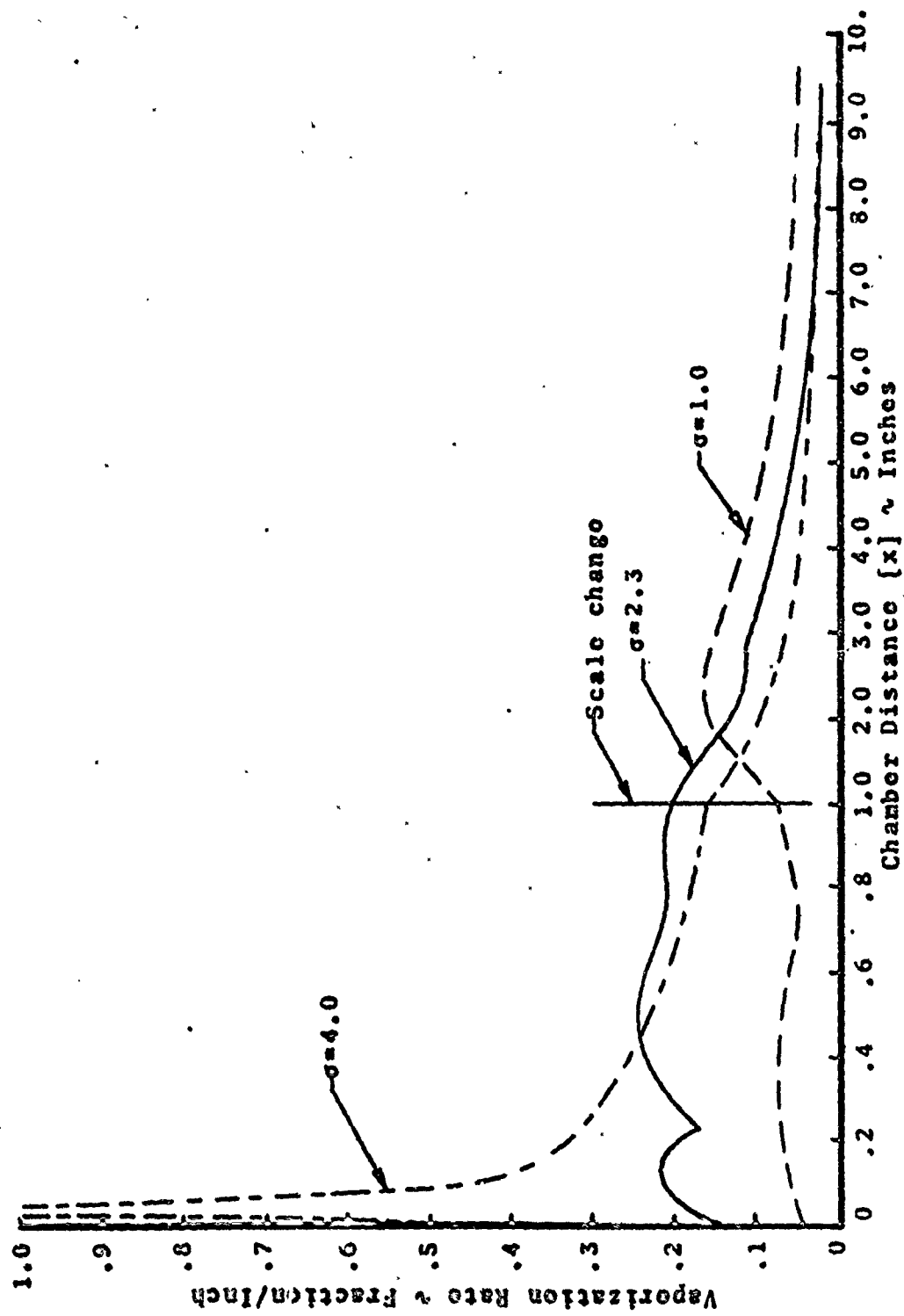


FIGURE 63. Variation of Oxidizer Vaporization Rate with Spray Standard Deviation.

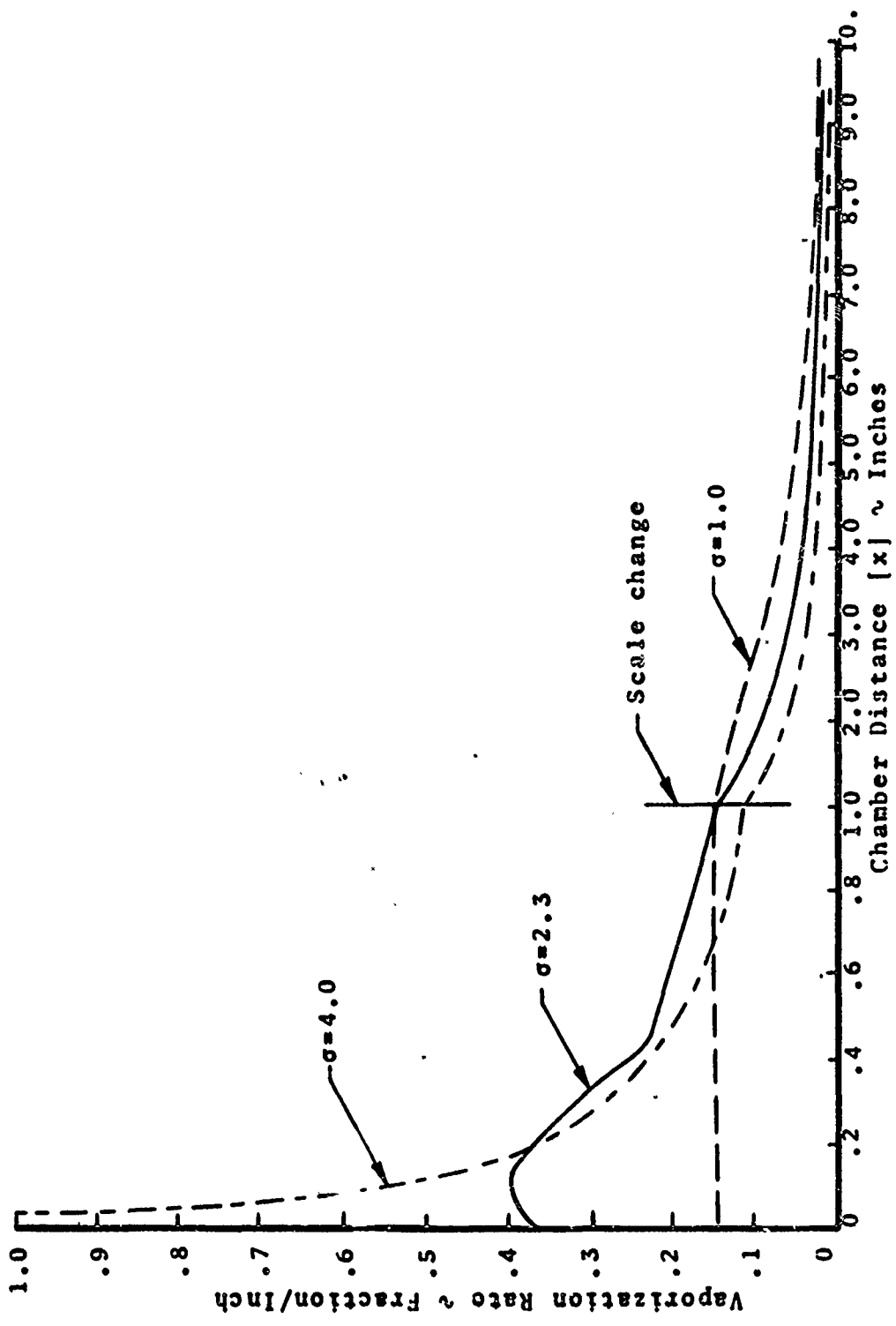


FIGURE 64. Variation of Fuel Vaporization Rate with Standard Deviation of Spray.

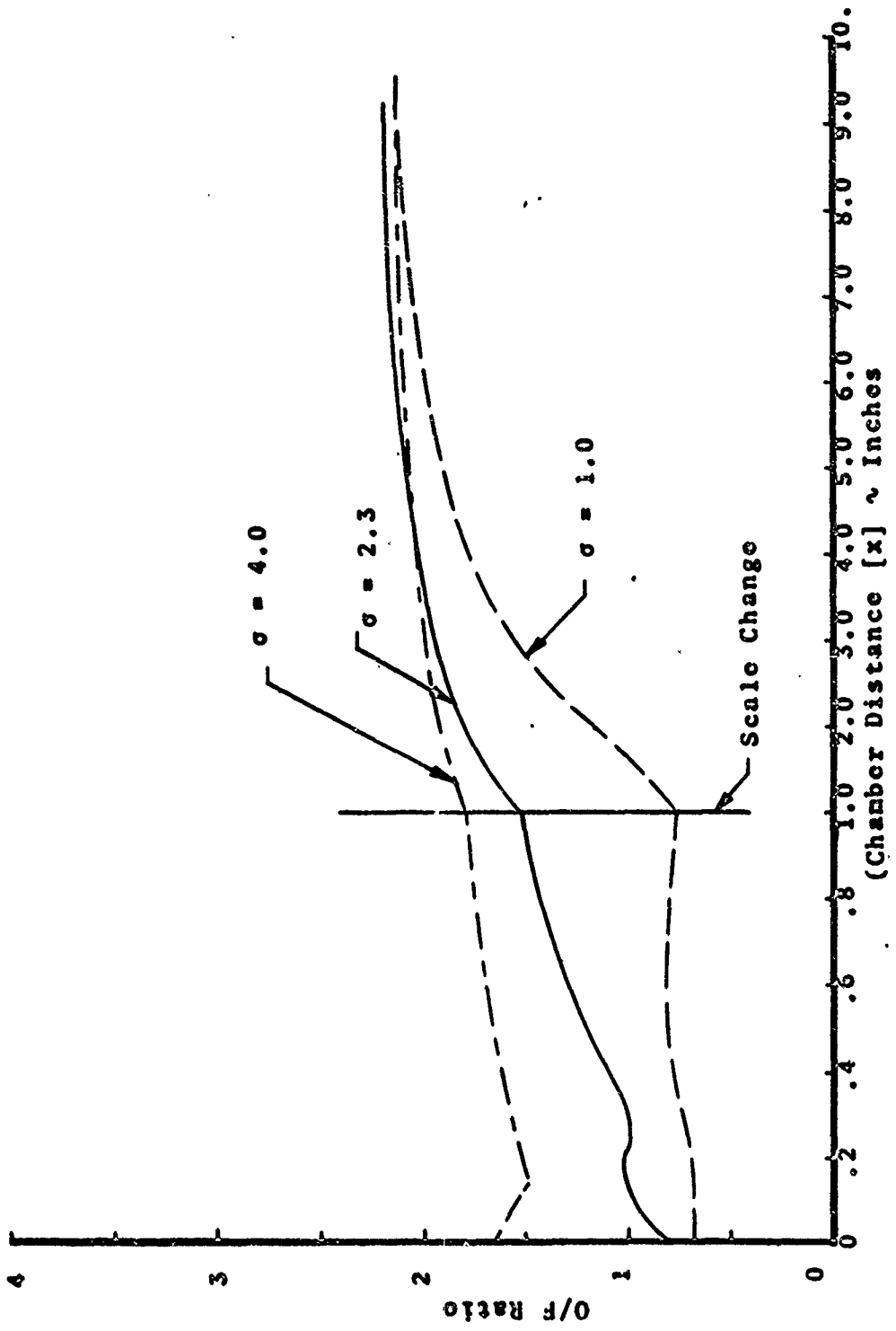


FIGURE 65. Variation of O/F Ratio with Standard Deviation of Spray

2. Stability Analysis

Combustion instability results are obtained by a method using a nonlinear model for determining the zones of a liquid rocket engine in which a tangential mode of high frequency instability is most easily initiated. The method for determining these zones was developed by Dynamic Science Corporation and details are presented in Reference 1. This method uses a nonlinear instability model with a propellant vaporization program. A rocket engine is analyzed by incrementally dividing the combustion chamber into annular nodes in the r and z directions as illustrated in Figure 8. Steady-state properties at each annular node or position in the chamber are computed from the propellant vaporization program. These steady-state properties and the stability limit curves from the instability model are used to determine the stability of the node. This process is repeated for each node to determine a stability map of the entire engine. Details of the application of this method are presented in Reference 1. This section will concentrate on the results of a parametric study of the influence of liquid rocket engine parameters on combustion instability. This study investigates the influences of propellant mixture ratio, injection velocity, droplet size and distribution, and chamber pressure on the minimum pulse strength required to trigger instability.

Steady-state and instability parameters at the most sensitive region in the engine are presented in Table II. The parameters varied were chosen as an average of what might be expected on a "Transtage" type engine, rather than to represent exact values actually obtained. These parametric variations around the base configuration were:

O/F	1.6 and 2.5
P_c	300 and 500 psi
Mass median droplet radius	25 μ and 225 μ
Droplet distribution	1 and 4 σ
Injection velocity	500 and 2000 in/sec.

Results of the parametric study show that, for the conditions considered, the oxidizer controlled the combustion process except where the "two flame" model was eliminated or the chamber pressure was above 300 psi. The "two flames" were suppressed in the 500 psi case due to the thin convective film thickness at high chamber densities. The study shows that the propellant vapor phase reactions reverse the vaporization rate trend indicated by the heat of vaporization, i.e. the oxidizer vaporizes slower than the fuel, thus enabling the oxidizer droplets to control the combustion process.

Results show that under the conditions studied droplet size and distribution have the largest effect on stability. Figures 66 and 67 present the variation of minimum pulse strength versus mass mean droplet radius and distribution. For a chamber configuration of the Transtage there is an optimum mass median droplet size for instability around 75 μ . Increasing or decreasing the droplet size increases the stability. For very large droplet radii the burning rate parameter is very small and the droplet Reynolds number is large; however, the net effect is to fall to the left side of the $\Delta P/P$ vs. L curve resulting in increased stability. For very small droplet radii the burning rate parameter is large; however, the Reynolds number is low, thus any burning rate parameter will have a high $\Delta P/P$. There is also an optimum distribution for instability at approximately 2 σ , increasing the distribution to 4 σ and decreasing the distribution to 1 σ increased stability. Increases in stability occur for the same reasons as for the effects of droplet radius. The greatest stabilizing effect was obtained at the large distribution end. At 4 σ there are a great number of very small and large droplets, with the small end controlling the stability character of the spray. Small droplets produce more stable combustion since, while the steady-state burning rate is high, their burning response w' is low, thus decreasing the wave-combustion rate coupling.

Increasing the droplet size moved the minimum relative velocity region further from the injector face, while decreasing the droplet distribution had the same effect. This is just the result of increased droplet surface area due to a greater number of smaller droplets for a given flow rate. It is interesting to note that a mass median droplet size of 75 μ and a distribution of 2.3 σ correspond to the worst conditions for stability and also droplet size and distribution produced by typical Transtage type injectors. Figure 68 has been developed from the results of Reference 3 with corrections for MMH and NTO physical properties. This figure shows that parallel and impinging jets have distributions of 2.3 σ , while in-line triplets have a distribution of 3.6 σ . For the study conducted, i.e., base engine conditions with a 75 μ mass-median droplet size, a triplet injector would be more stable than parallel or doublet jets. From Figure 68, droplet sprays between 50 μ to 100 μ are produced by jet diameters for parallel jets (-0.008 to 0.025 inches), impinging jets (-0.035 to 0.095 inches), and triplets (-0.125 to 0.650 inches). Injector atomization photographs taken by Dynamic Science Corporation indicate that Δ positioned triplets produce a coarser spray than in-line triplets and X quadlets produce a coarser spray than Δ triplets. This is due to the fact the doublets and in-line triplets produce fans. These fans form droplets by the formation of sheet instabilities with finer droplets being produced by thinner sheets.

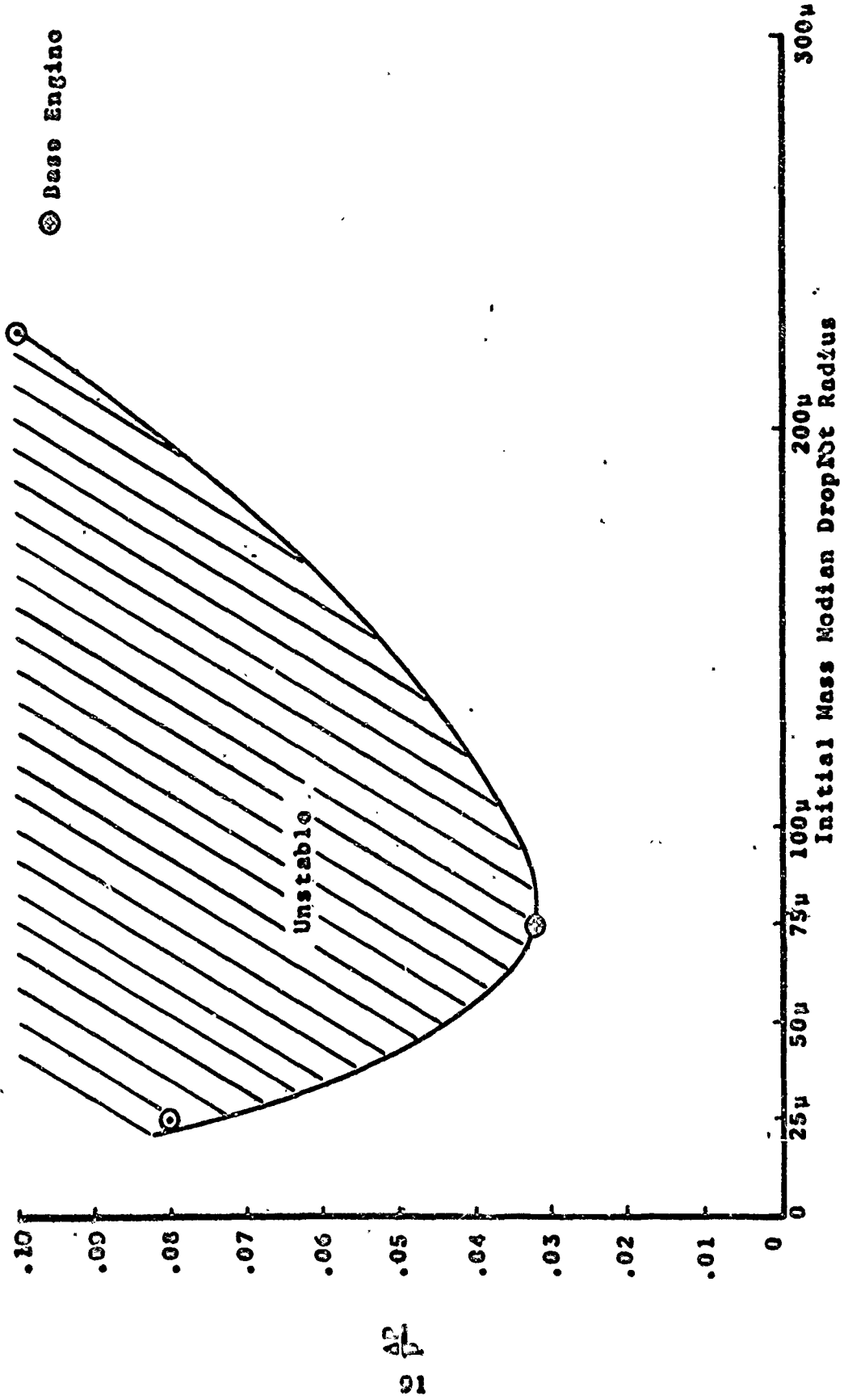
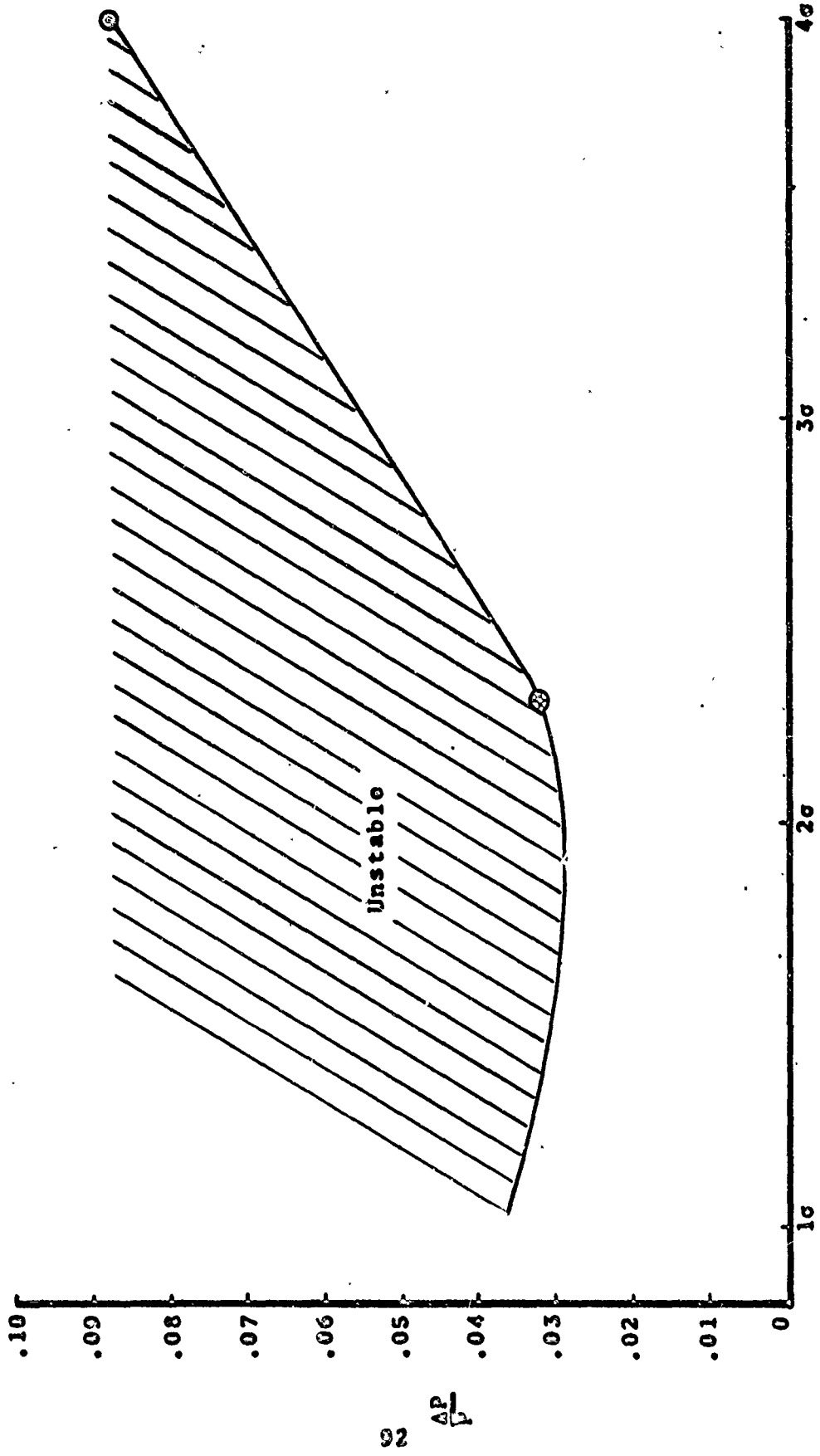


FIGURE 66. Effect of Droplet Radius on Minimum Threshold Disturbance.

⊗ Baso Engine



Droplet Distribution V

FIGURE 67. Effect of Droplet Distribution on Minimum Threshold Disturbance.

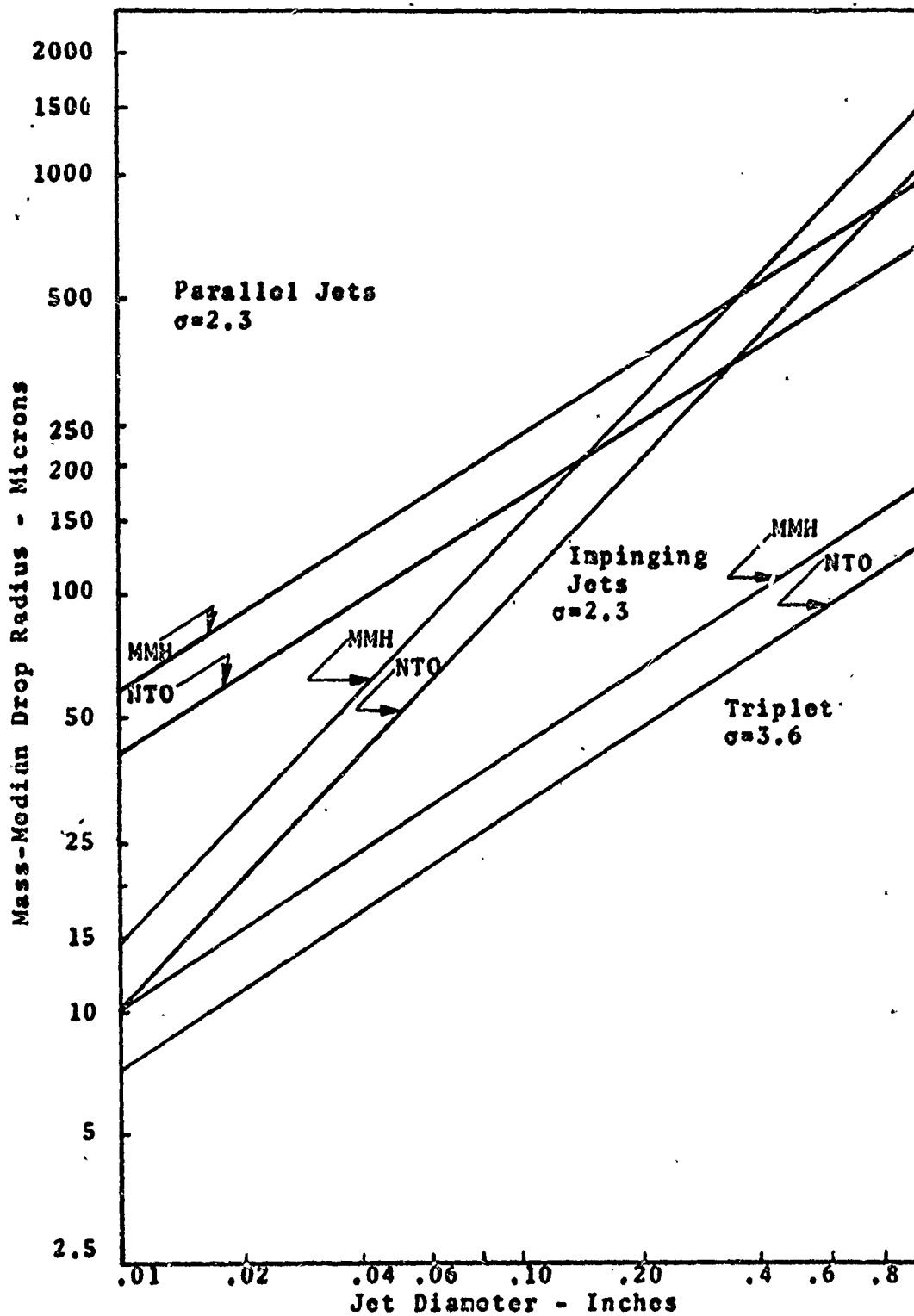


FIGURE 68. Drop Sizes Determined from Experimental Engine Performance. (Ref. 3)

Quadruplets and A triplets tend to form a stream which breaks up similar to parallel jets thus forming droplet sizes between the in-line triplet and parallel jets.

Chamber pressure was the third most important parameter affecting instability. Increasing chamber pressure moved the minimum relative velocity position away from the injector face. This occurs due to the fact that the gas velocity increases slower than the increased mass addition, since the gas density is higher. At 500 psi the burning rate was slower since the MMH droplets burned with a single flame. At this pressure the gas density is high thus the gas Reynolds number is high, resulting in a thin diffusion film thickness. Since the diffusion time is short due to the thin film the MMH does not have time to decompose. Thus the heat transfer is lower to the droplet and the vaporization process becomes slower. The effect of chamber pressure on stability is shown in Figure 69. For constant flow rates, i.e., the contraction ratio is increased to increase chamber pressure, stability remains constant with increased chamber pressure between 100 and 300 psia. Here the stabilizing effect of decreasing the burning rate parameter by increasing the contraction ratio equals the destabilizing effect of increasing the Reynolds number of the droplet by increasing chamber gas density. For the conditions considered, increasing the chamber pressure (at constant flow rate) to 500 psia produced a stabilizing effect. Since at this pressure the droplet spray considered burns in the slower single flame regime. Thus, the fraction vaporization rate decreases, decreasing the burning rate parameter offsetting the destabilizing effect of the gas density. For larger droplet sprays, where the droplets would continue to burn in the two flame regime at 500 psia, or propellants which do not decompose, stability would remain constant or decrease. The 500 psia case was the only condition where control switched from the oxidizer spray to the fuel spray. To determine the differences between MMH burning with a "two flame" model and a single flame considered in Reference 3, a case was run at base conditions with the decomposition flame suppressed. For this run the burning rate parameter was reduced from 0.40 to 0.19 corresponding to an increase of minimum threshold disturbance from 0.032 psi to .050 psi. Thus additives which would suppress the MMH decomposition would increase stability; however, this may tend to decrease performance.

For conditions where the chamber pressure is increased by increasing the flow rate, while keeping the contraction ratio constant, the engine is destabilized. Under these conditions the increased Reynolds number of the droplet overrides the decrease of the burning rate parameter due to the decreased fraction vaporized per inch.

⊗ Base Engine

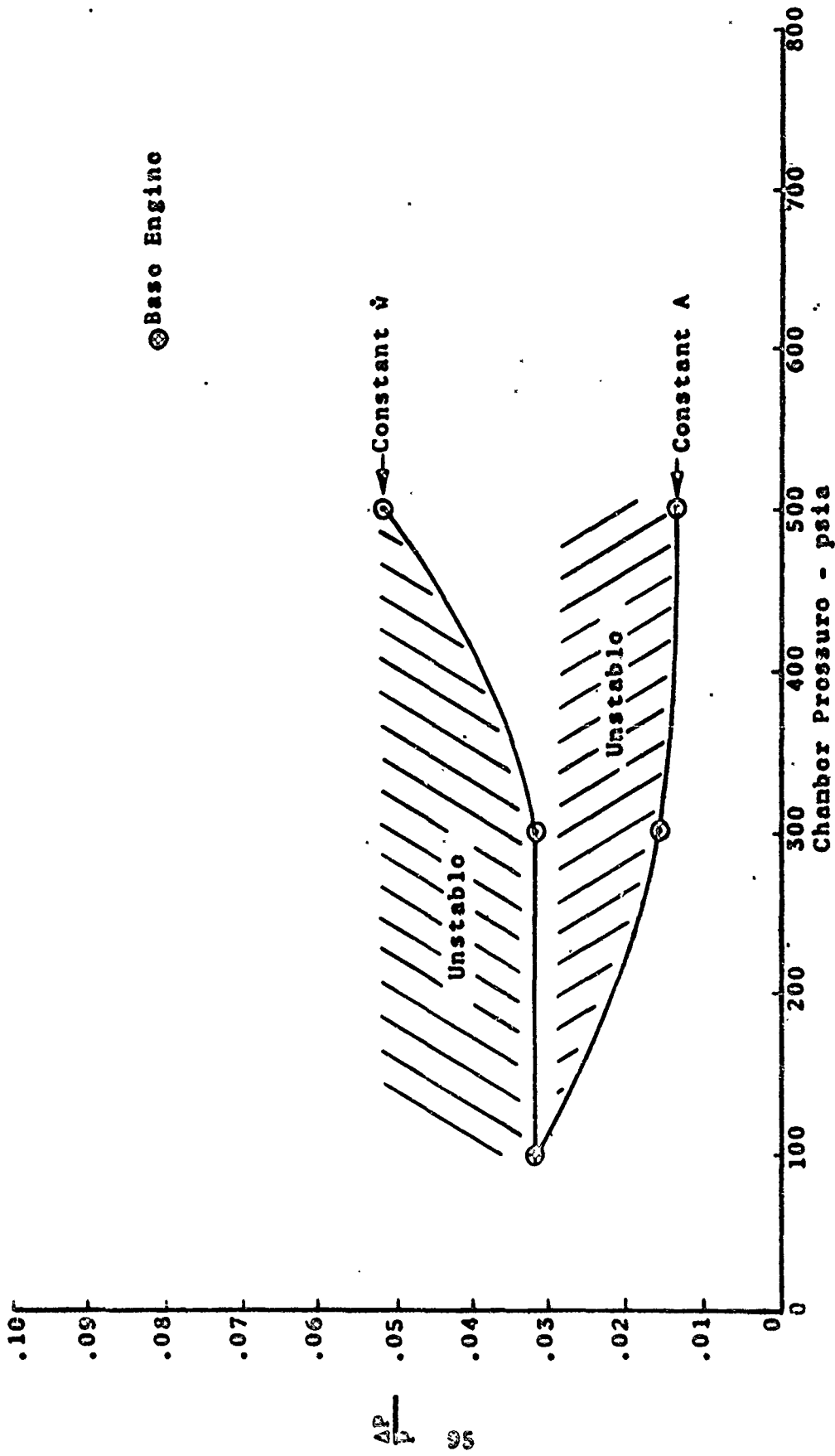


FIGURE 69. Effect of Chamber Pressure on Minimum Threshold Disturbance.

Injection velocity effects are shown in Figure 70. The point of minimum relative velocity was moved away from the injector face by increasing the injection velocity. Increasing the injection velocity decreases the stay time of the droplets requiring more distance to vaporize the same amount. As shown in Figure 70 increasing the injection velocity slightly increases the stability. The increased injection velocity, decreases the fraction vaporized per inch and thus the burning rate parameter, resulting in increased stability.

The effects of mixture ratio are presented in Figure 71. There is essentially no effect of mixture ratio on disturbance amplitude which remains approximately at 0.030 psi. It should be noted that this variance of mixture ratio only represents the proportions of propellant with the total flow rate kept constant. Experimentally, strong effects of mixture ratio are noted on stability characteristics; however, when mixture ratio is varied in a given configuration, changes result in droplet spray, injection velocity and chamber pressure as well as local mixture ratio. Thus, the effects of changing mixture ratio in an engine result from the influence on other parameters.

Experimental Correlation

Rocket engine tests utilizing the MMH/nitrogen tetroxide propellant combination were conducted at the Air Force Rocket Propulsion Laboratory and results were reported in Reference 17. Twenty three tests were conducted using two Transtago engine configurations. The two engines consisted of the Titan III Transtago combustion system, i.e., thrust chamber, injector and bipropellant valve. The stability evaluation test program used a workhorse steel thrust chamber having the same conical internal contour as the flight model ablative chamber. Models Trax 21-1D and Trax 21-11B injectors were tested. Major effort was expended on the Trax 21-1D injector which was tested 14 times with MMH at chamber pressures between 91-102 psia and mixture ratios between 1.75-2.56. The Trax 21-11B was tested 4 times with MMH at chamber pressures between 97-100 psia and mixture ratios between 1.78-2.33.

As described in Reference 17, the -1D injector has an aluminum dished face, is 11.645 inches in diameter, and possesses four radial baffle vanes extending from a small diameter center fuel hub. All the fuel is used to regeneratively cool the baffles prior to injection into the combustion chamber. The -1D injector has a quadlet pattern consisting of two oxidizer holes impinging with two fuel holes. The total included impingement angles for both sets of holes is 70 degrees. There are a total of 8 rows

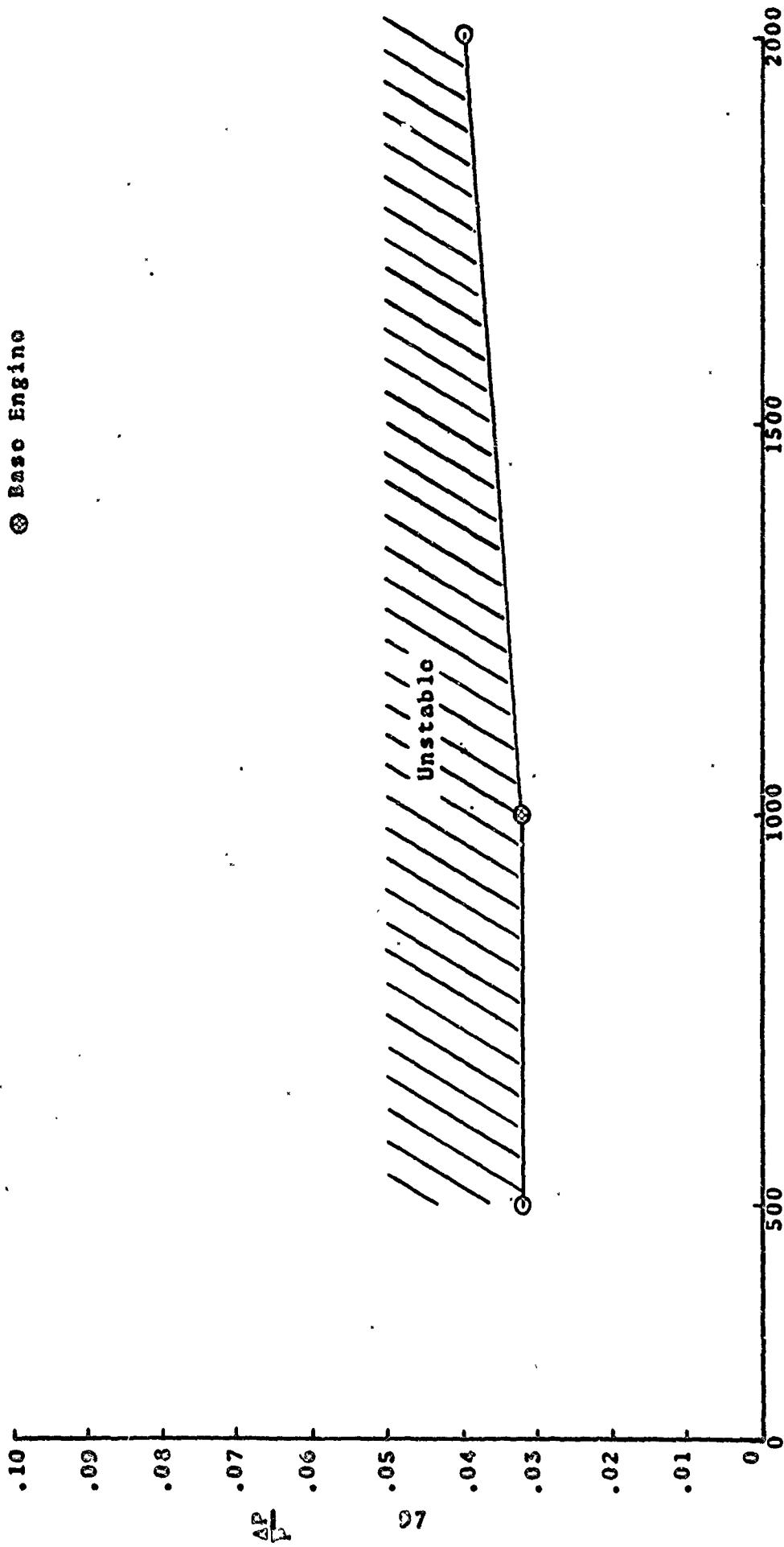


FIGURE 70. Effect of Injection Velocity on Minimum Threshold Disturbance.

⊗ Baso Engine

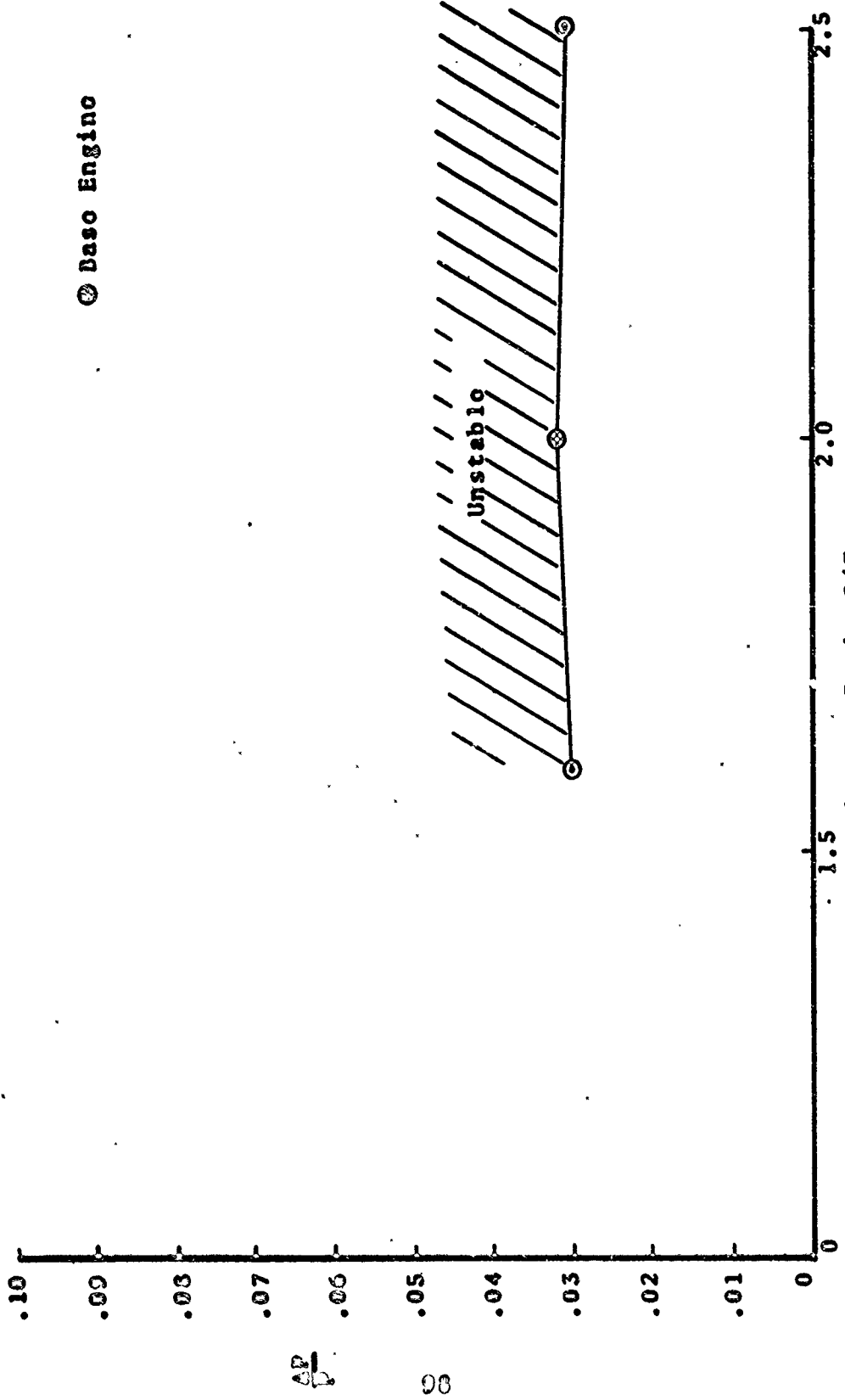


FIGURE 71. Effect of Mixture Ratio on Minimum Threshold Disturbance.

of injector elements with three fuel holes in each baffle tip and one row of fuel showerhead holes located around the periphery of the injector provide for film cooling. There are 672 oxidizer orifices with an orifice diameter of 0.0360 inches and 672 fuel orifices with an orifice diameter of 0.0292 inches.

The Trax 21-11B injector pattern also consists of 8 rows of injector elements of which the first, second, third, fifth, and seventh rows, starting from the injector center, are the quadlet pattern as the -1D injector. The fourth, sixth, and eighth rows were changed to provide for Δ triplets with two fuel holes impinging with one oxidizer hole. The fuel hole diameter has been enlarged to 0.0512 inches (0.0360 inches for the quadlet pattern). In addition, the outer rows of fuel film coolant holes have been eliminated.

The -1D and -11B injectors had approximately the same performance, with the -11B being higher at a mixture ratio of 1.8. All 14 tests conducted with the Transtage -D injector resulted in combustion instability; three of these instabilities were initiated by spontaneous pops with a ΔP higher than 40 psi, and the remainder of the tests were initiated with 10, 15, or 20-grain pulse charges. The 4 tests conducted with the -11B injector also were triggered unstable. Three of the 4 tests required a 40-grain pulse to initiate instability while the fourth required only a 20-grain pulse. Pulse charge size required to trigger instability for the Transtage injectors is plotted in Figure 72. All resultant instabilities with the Transtage injectors were of the second tangential mode with frequencies of oscillation of approximately 3700-3900 cps. Peak-to-peak pressure amplitudes were higher for the -1D injector (100-130psi) than the -11B injector (40-60 psi). In general, the 11-B injector showed much greater stability than the -1D injector.

To determine the droplet sizes produced by the -1D and -11B injectors, water flow tests were conducted at Dynamic Science Corporation. By taking spray photographs it was determined that X quadlets produced larger droplets than doublet injectors and Δ triplets produced larger droplets than in-line triplets under the same conditions. Larger droplets are formed since quadlets tend to produce a stream rather than a thin sheet, resulting in wave instabilities of longer period on the liquid surface. In-line triplets form fans, while Δ triplets tend to form thicker sheets or streams. Using the photographs taken by Dynamic Science and results of Figure 68, mass-median droplet sizes of the quadlet and triplet are estimated to be 65 μ and 20 μ respectively.

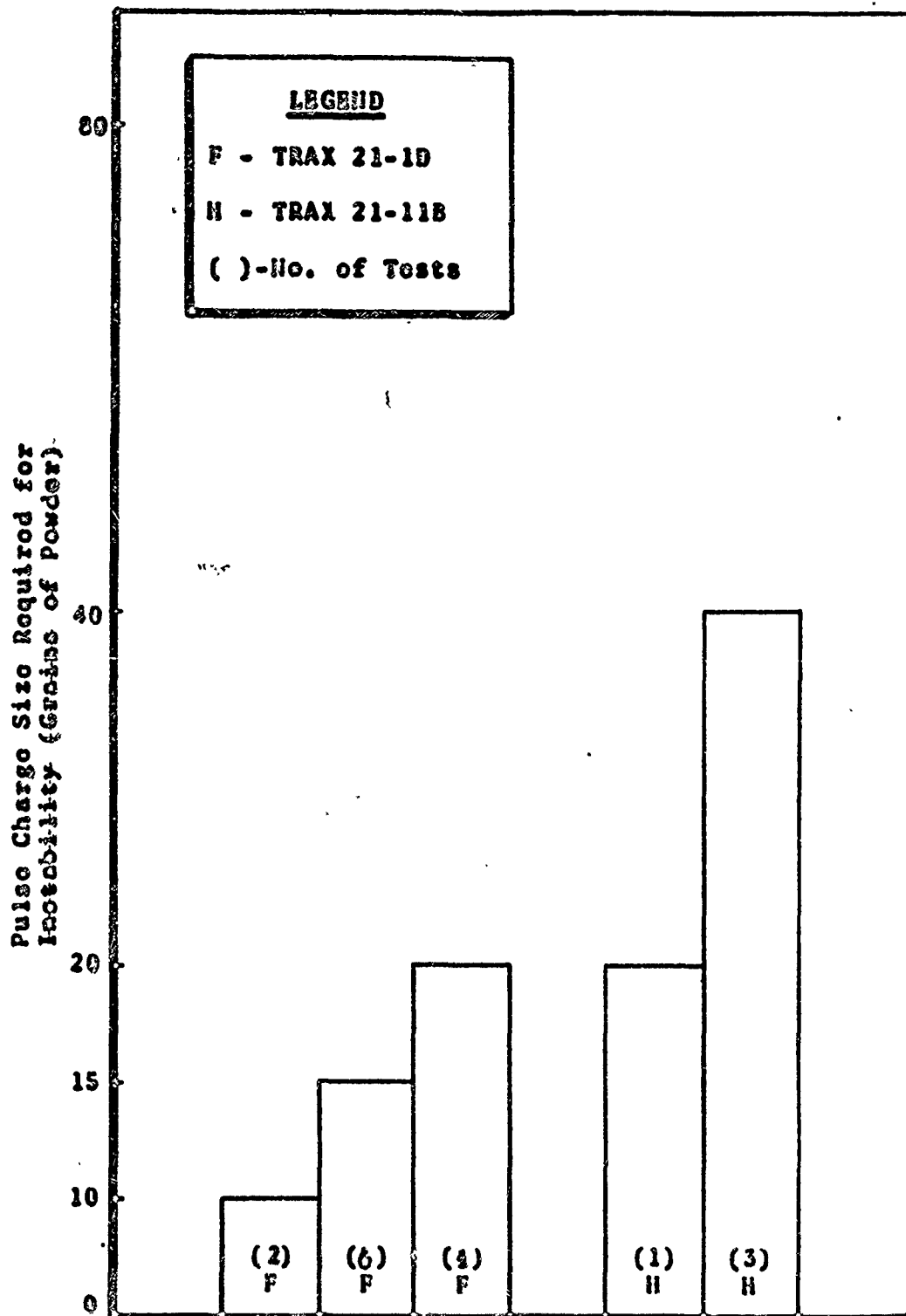


FIGURE 72 .Instability Tests for Transtage Using MMH & NTO

The mass-median fuel droplets produced by the cooling film parallel jets was estimated to be 115μ . Since the outer edge of the engine is most sensitive to be pulsed unstable, the effective droplet mass-median size can be estimated to be approximately 70μ for the -1D injector and 30μ for the -11B injector by weighting the outer elements heavier than the center. From Figure 66 it can be seen that for the propellant and conditions of the Transtage engine the -11B injector would be more stable. In addition, the -11B injector also has a greater droplet distribution since triplets are being utilized. Greater droplet distribution improves stability for the case considered. As shown in Figure 72 there is a scatter in the minimum pulse strength required to produce instability. Since these runs were made at different mixture ratios, variation occurred in injection velocity, chamber pressure, and local mixture ratio. Secondary effects also occur on the atomization process. Thus for these two injectors considered, injector patterns influenced the combustion characteristics considerable more than operating conditions.

Conclusions

Before a detailed experimental correlation can be obtained greater information about injector spray characteristics will be required. While correlation was obtained with the two injector tests considerably more work will be required to conclusively evaluate the value of the outlined model. While trends seem to be predicted there is a large difference between predicted and measured $\Delta P/P$ required to trigger instability. It was experimentally determined that the pulse amplitude required to trigger instability was 0.4 while calculated amplitudes are approximately 0.03. Greater refinement of the model will be required before quantitative results can be obtained; however a method which gives qualitative results is of value from a design standpoint.

Significant results of this study show that: 1) the two flame model showed increased burning rate and decreased stability. The oxidizer controlled the combustion process, except at 500 psi where the two flames were suppressed, thus the propellant vapor phase reactions reverse the vaporization rate trend indicated by the heat of vaporization. 2) There was a droplet size and distribution which produced minimum stability. Variation in either direction produced increased stability. 3) Chamber pressure variations resulting from changes in contraction ratio at constant flow rate, increased the stability. Keeping the contraction ratio constant and increasing chamber pressure by increasing flow rate decreased stability. 4) Stability increased with increasing injection velocity. Spray characteristics were held constant while injection velocity was varied. 5) Variance of mixture ratio, resulting from changing the proportions of propellant with constant flow rate, did not affect the stability characteristics. 6) Comparison with experiments showed that the model underestimated minimum disturbance levels but correctly indicated stability trends with injector designs.

IV. LIQUID PHASE MIXING AND REACTION

The amount of reaction between impinging unlike streams must be considered when calculating the combustion rate of hypergolic propellant systems. Liquid phase reaction and heat release during impingement would affect the droplet combustion rate.

The maximum amount of reaction which might occur between impinging hydrazine/nitrogen tetroxide streams was estimated using a conservative mixing model and the heat release data of Feiler and Somogyi (Ref. 18). In conjunction with this mixing model, criteria was established to predict the pressure potential tending to separate a mixed hypergolic emulsion. The percentage of liquid phase reaction and the subsequent separation of the unlike hypergolic streams was thus predicted for the hydrazine/NTO system. The physical model and the available data also lead to the postulation of an ignition index number suitable for rating the start-up and operational characteristics of hypergolic liquid phase contacting devices.

1. Liquid Phase Reaction.

a. Heat Release Rates.

Heat release rates of hypergolic liquid systems have been measured by Feiler and Somogyi (Ref. 18). Their experimental procedure consisted of a tangential mixing injector and a mixing cup of length L . The reaction was quenched as soon as it left the mixing length L . The heat release results of these experiments are shown in Figure 73.

The shape of these curves are characteristic of the degree of mixing, $F(M)$, occurring within the mixing length L . For complete mixing the data determine the maximum rate of the liquid phase heat release. Feiler and Somogyi explain the shape of these curves in the following way (Ref. 18):

"The increase in heat-release rate with injection velocity at the lower velocities (Fig. 73) may thus be attributed to an increase in interfacial area or in $F(M)$. The rapid rise in heat-release rate observed at injection velocities of 120 to 140 feet per second is attributed to an increase in temperature. In this velocity range it appears that heat generated in the interfacial area can no longer be dissipated to the surrounding fluid at a sufficient rate, and therefore the temperature of the reacting material increases, which results in an exponential increase in heat-release rate. At velocities greater than about

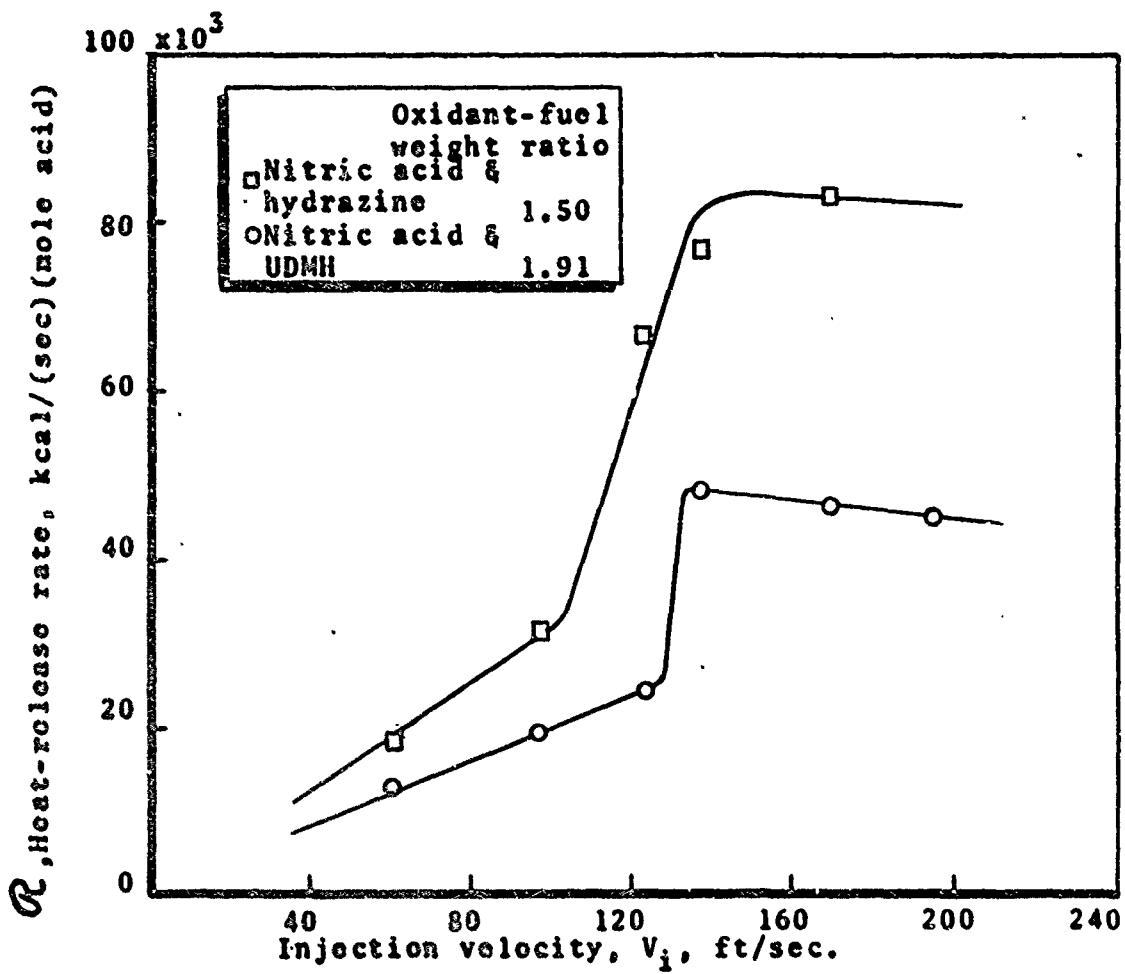


FIGURE 73. HEAT-RELEASE RATE AS FUNCTION OF INJECTION VELOCITY(Ref. 18).

140 feet per second the heat-release rates attain constant values or perhaps decrease slightly, which indicates that temperature has attained a constant value. This temperature is probably a characteristic temperature of the propellant system such as the flame temperature. It is possible that gas evolution rates accompanying the reaction are sufficient at the highest injection velocities to inhibit the mixing process. The resulting decrease in $F(M)$ (interfacial area) would thus account for a decrease in the heat-release rate."

The maximum heat release rates, with complete mixing, were thus determined to be 83,000 and 48,000 (kcal)/(sec) (mole HNO_3) for hydrazine and UDMH, respectively, (Figure 73).

b. Interfacial Resistance to Reaction.

Experiments (Ref. 18) determined that the maximum liquid phase heat release rate was independent of oxidant to fuel weight ratio (i.e., concentration), as shown in Figure 74. It was postulated rather that the maximum heat release rate was dependent upon the stoichiometric ratio of reactants for the following reasons: 1) the rate of heat release appears to be independent of concentration, 2) four times as many molecules are required to oxidize a molecule of UDMH as are required to oxidize a molecule of hydrazine, and 3) the heat of reaction per mole of acid for fuel is approximately the same for either fuel (UDMH-158, H-147, kcal/mole).

This treatment of the data may be justified by considering an interfacial resistance mechanism. The following two observations lead to the conclusion that reaction kinetics are not the controlling mechanism in liquid phase mixing:

(1) The observed rate of reaction is independent of concentration (Figure 74), and

(2) The half-life of a mixture of hydrazine/NTO is on the order of 10^{-7} seconds, according to gas phase kinetics of Glass and Sawyer, (Ref. 19). This kinetic rate is more than four orders of magnitude faster than the liquid phase mixing reaction rate data of Figure 75. Thus a mechanism other than kinetic reaction rate must be controlling the rate of liquid phase reaction. The mechanism postulated here is one of interfacial resistance.

It has been previously pointed out that hydrazine/NTO appear to be immiscible (Ref. 20). If the surface reaction time is faster than the characteristic mixing time and, if there is sufficient pressure potential in the products to

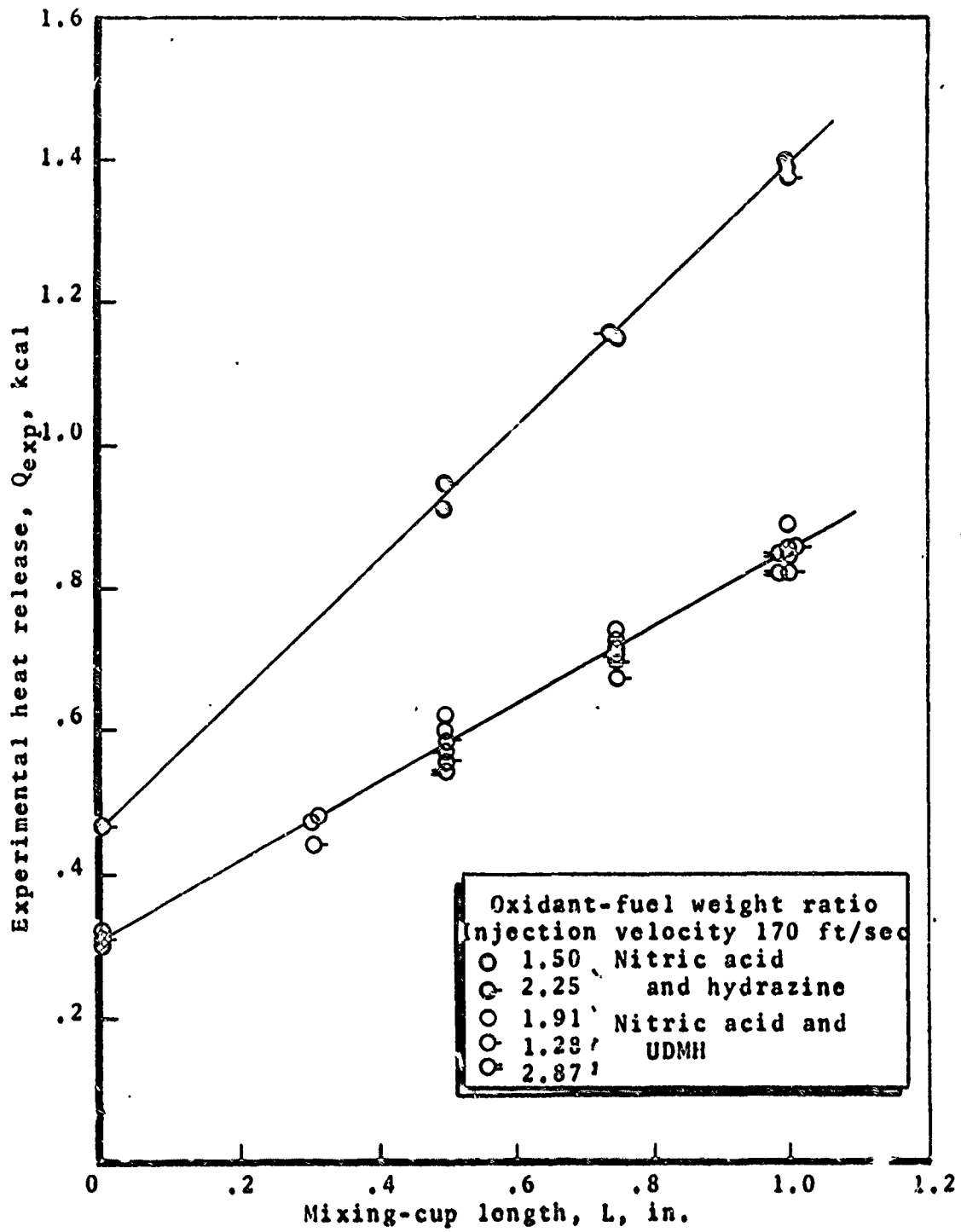


FIGURE 74. EXPERIMENTAL HEAT-RELEASE CURVES FOR VARIOUS CONCENTRATIONS. (Ref. 18)

maintain separation, then this immiscibility might be due to the fact that a drop of one component, having its own surface, will tend to maintain this surface when contacted with the other component. Under these conditions an interfacial resistance to reaction will be established and will produce an effect analogous to immiscibility. Comparison of reaction time to mixing time indicates this interfacial resistance mechanism, while the condition of pressure potential is treated below.

Considering this interfacial resistance to reaction, the rate of reaction will be controlled by the stoichiometric ratio. This is due to the fact that the two liquids, facing each other across this resistance, are both pure. Thus reaction is dependent on the stoichiometric ratio of each fuel system and the maximum rate with perfect mixing will give a conservative estimate of heat release for any hypergolic fuel system, based upon its stoichiometric ratio and the assumption that its reaction rate is slower than its mixing rate. Figure 75 presents an estimate of the maximum heat release rate produced upon complete mixing of hypergolic propellants. This maximum rate is valid as long as the propellants are confined together and are perfectly mixed.

c. Characteristic Confined Mixing Length.

The physical model of Figure 76 was postulated in order to estimate the length of time during which impinging streams are held together. An element of fluid is within the impingement area for an average length of time, T_{mix} :

$$T_{mix} = \frac{\pi D_0}{8} \cdot \frac{1}{v_f}$$

where: D_0 is the jet diameter, and v_j is the forward velocity of the jet as shown in Figure 76. While the element of liquid is within this area of impingement it is confined in the same way as if it were contained within a mixing cup similar to the experiment of Reference 18. Although perfect mixing may not occur for impinging streams, as in the case of the mixing cup, the assumption of perfect mixing sets a maximum limit upon the heat generation rate. Thus the average time within the area of impingement gives a conservative estimate of the amount of forced mixing occurring between two unlike hypergolic streams. Whatever happens after the element leaves this area of influence will be independent upon a force balance between the element's momentum and the pressure potential of reactant gases. This problem of stream separation is discussed in the next section of this report, in this section the purpose is to calculate the maximum amount of propellant reacted during liquid phase mixing.

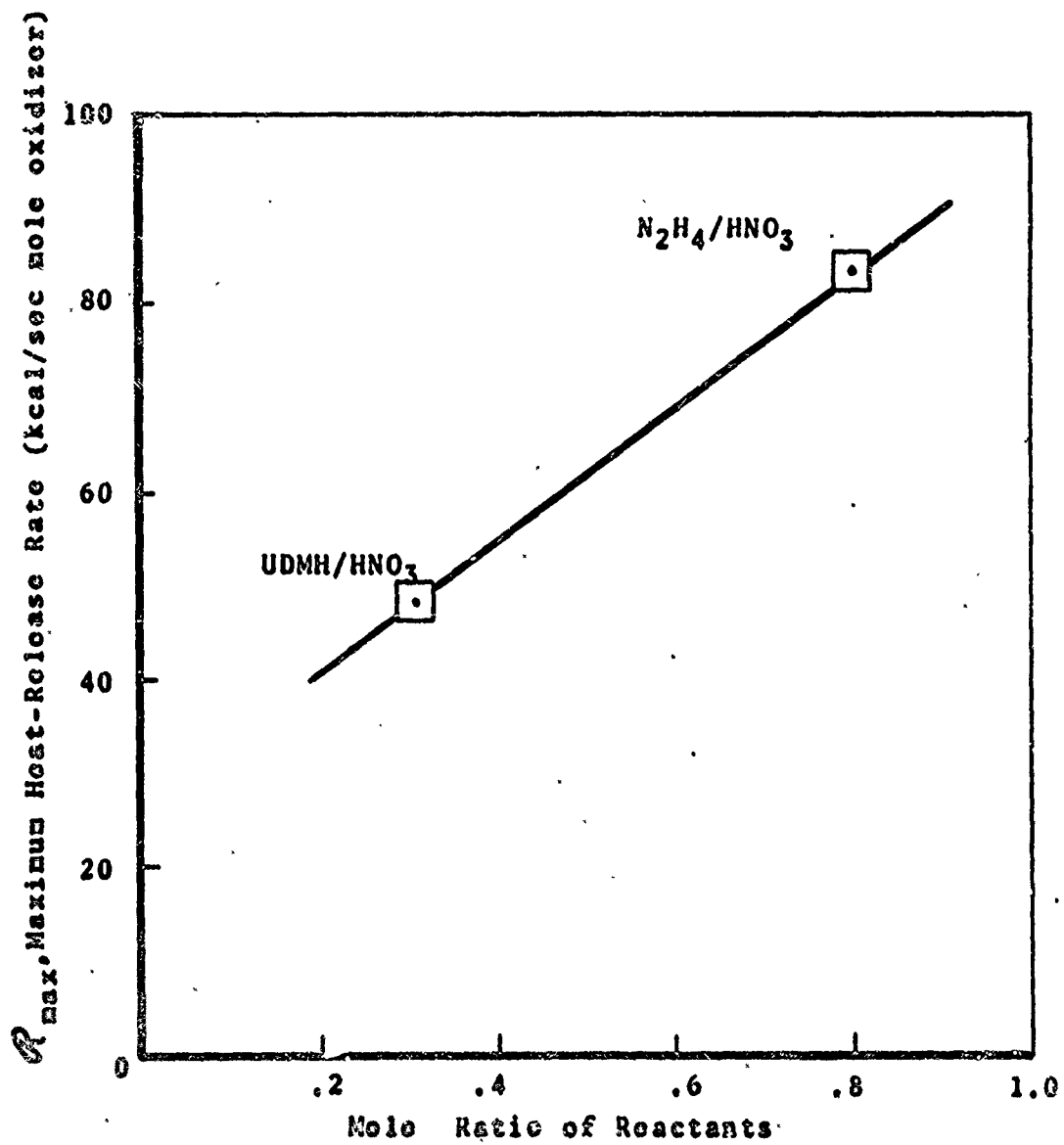


FIGURE 75. MAXIMUM HYPERGOLIC HEAT-RELEASE RATE, FOR HYDRAZINE TYPE FUELS, DATA FROM FEILER AND SOMOGYI (Ref. 18).

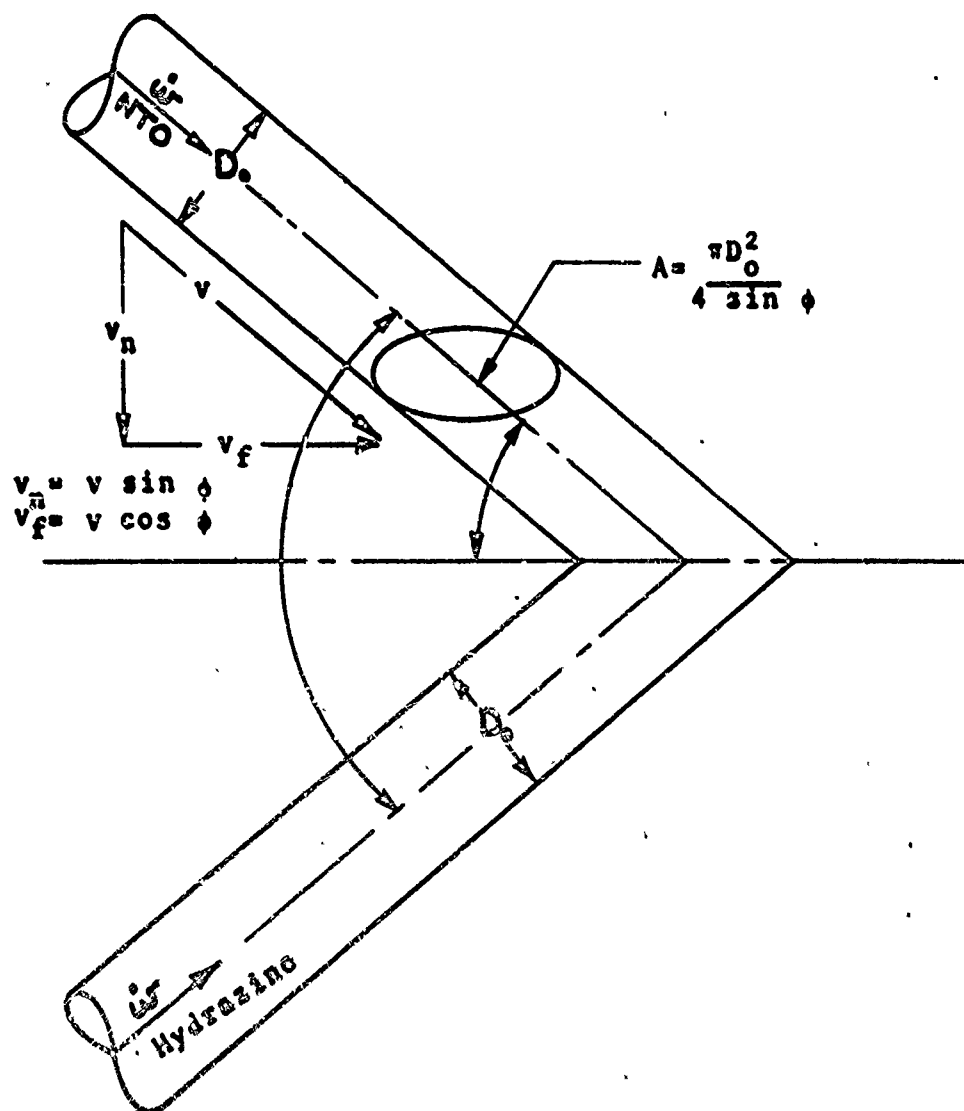


FIGURE 76. REACTIVE STREAM IMPINGEMENT GEOMETRY

d. Numerical Example.

The following example is based upon the model of Figure 4 and the maximum heat release rate data of Figure 75. Consider the unlike hypergolic impingement of hydrazine/nitrogen-tetroxide. Typical parameter values are: jet diameter equal to 0.050 inch diameter; jet velocity equal to 720 inches per second; and impingement angle equal to 90°. The characteristic time of mixing is

$$T_{mix} = \frac{\pi D_o}{8} \frac{1}{v_f}$$

The stoichiometric ratio of reactants for this system is 0.5. Thus from Figure 75 the estimated maximum heat release rate, \dot{R}_{max} , with perfect mixing is 62,000 cal/(sec) (mole acid). The heat generated by liquid phase reaction is given as

$$T_{mix} = \frac{(3.14) (5 \times 10^{-2})}{(8) (.707) (7.2 \times 10^4)}$$
$$= 4 \times 10^{-4} \text{ sec.}$$

$$Q_{liq} = \dot{R}_{max} T_{mix}$$

Thus $Q_{liq} = 24 \text{ cal/mole of oxidizer}$

Whereas the heat of reaction which will finally be released for the hydrazine/nitrogen tetroxide system is $\Delta H_{React} = 248,000 \text{ cal/mole oxidizer}$. Thus the amount of heat released during liquid phase mixing of a typical unlike impinging doublet is estimated at 0.01% or 1×10^{-4} fraction of the total amount of heat available. A similar impinging MMH/NTO doublet will have the same value for T_{mix} while its reactant mole ratio of 0.8 gives a maximum rate of heat release of 83,000 cal/sec. Thus the estimated liquid phase heat release is 33 cal/mole of oxidizer and the percentage reacted based upon a total heat release of 218 kcal/mole NTO is 0.015%.

2. Liquid Phase Separation Potential.

When chemical reaction occurs there is a temperature potential developed at the reacting interface which is characteristic of

- The magnitude of the heat of reaction.
- The enthalpy capacity of the immediate surroundings.
- The thermal transport properties of the immediate surroundings.

If conditions of confinement and transport properties are defined in the immediate surroundings, a physical model may be postulated so that absolute numbers for the transient temperature rise may be calculated. However, if the immediate surroundings are somewhat undefined, an index number may still be developed by making use of known characteristics of the system. For the case of reaction between impinging hypergolic streams, the immediate surroundings are not well defined.

In this section an estimation of impinging stream separation was developed for two cases.

First, for the adiabatic case which neglects thermal transport in the surrounding liquid, and

Second, for the unknown thermal case which requires definition of an index number, considering that the thermal transport will be characterized by this number and thus that the tendency of streams to separate may be rated according to this index.

a. Hypergolic Stream Impingement.

The two streams of Figure 4 impinge at 2ϕ degrees on a common plane. The common impingement area is

$$A = \frac{\pi D_o^2}{4 \sin \phi} = \text{area of ellipse.}$$

The normal force of impingement is determined from a momentum balance on the stream before and after impingement:

$$F_n = \frac{wV}{g_c} \sin \phi$$

This force results in a pressure at A such that,

$F_n = \Delta P \times A$. Note: Rupe (Ref. 21) has treated the dynamic characteristics of free liquid jets in detail. However, detail has been omitted from this order-of-magnitude analysis.

Substituting:

$$\Delta P = \frac{4wV(\sin \phi)^2}{\pi D_o^2 g_c}$$

For impinging reactive liquids the temperature rise of product vapor is given by a heat balance

$$\Delta T = \frac{\Delta H_R - \Delta H_V - \Delta H_L}{C_p}$$

where ΔH_R - heat of reaction
 ΔH_V - heat of vaporization
 ΔH_L - heat lost to the surroundings

This temperature potential may be related to the pressure potential necessary to overcome the momentum of impingement by the Clapeyron equation

$$\Delta P = \left(\frac{\Delta H_V}{T V_g} \right) \Delta T = \left(\frac{\Delta H_V P}{nRT^2} \right) \Delta T.$$

where the coefficient $(\Delta H_V / T V_g)$ is the average slope of the vapor pressure curve in the range of interest.

Substituting the temperature potential for pressure results in the criteria that:

$$\text{If, } \frac{\Delta H_R - \Delta H_V - \Delta H_L}{C_p} > \frac{nRT}{\Delta H_V P} \frac{4Wv(\sin \phi)^2}{\pi D_0^2 g_c}$$

the streams will be blown apart by reaction and thus cannot be mixed by impact momentum.

b. Adiabatic Case.

If it is assumed that no heat is lost to the surrounding liquid, (i.e., the reaction time is small compared to the time required for thermal transport - then Q_L is equal to zero.

Thus if

$$\frac{\Delta H_R - \Delta H_V}{C_p} > \frac{nRT^2}{\Delta H_V P} \frac{4Wv(\sin \phi)^2}{\pi D_0^2 g_c}$$

the streams will be blown apart.

An example is made of the hydrazine/NTO system considered previously. The numerical values are

$$\Delta H_R = \Delta H_V \quad 82.6 \text{ kcal/mole of reactant}$$

$$C_p = 8.6 \times 10^{-3} \text{ cal/(mole of products) } (^{\circ}\text{K})$$

with 7 moles of products per 3 moles of reactant.

Thus the adiabatic temperature potential (evaluated at 200°C) available in this system is

$$\Delta T_p = \frac{3}{7} \frac{82.6}{8.6 \times 10^{-3}} = 41 \times 10^3 \text{ } ^\circ\text{K}$$

Whereas the temperature potential to be overcome in order to separate the streams of Figure 76 with numerical values of example in paragraph IV-1.-d., evaluated at 200°C and 300 pzi, is

Temperature-Pressure Conversion

$$\frac{nRT^2}{\Delta H_v P} = 3.9 \times 10^{+2} \text{ } ^\circ\text{K/atm}$$

Momentum Pressure

$$\Delta P = \frac{4Wv(\sin \phi)^2}{\pi D_o^2 g_c} = 1.65 \text{ atm}$$

Thus

$$\frac{nRT}{\Delta H_v P} \frac{4Wv(\sin \phi)^2}{\pi D_o^2 g_c} = 6.42 \times 10^2 \text{ } ^\circ\text{K}$$

Since $4.1 \times 10^4 > 6.4 \times 10^2$, the hydrazine/NTO streams may be predicted to separate after initial contact and surface reaction.

c. Separation Index Number.

Since the stream impingement is not truly adiabatic a separation index based upon the Clapyron potential conversion can be used to evaluate hypergolic stream separation.

This index is

$$I_s = \frac{(\Delta H_R - \Delta H_v)}{\frac{nRT^2}{\Delta H_v P} \frac{4Wv(\sin \phi)^2}{\pi D_o^2 g_c}}$$

so that the larger the value of I_s the greater the tendency of the streams to separate.

3. Characteristic Ignition Index.

The data reported by Feiler & Somagyí (Ref. 18) which is presented in Figure 73, can be used to develop an index to relate ignition characteristics of different injector devices. The words which Feiler uses to describe the rapid rise in heat release rate observed in Figure 73 can be interpreted as defining the beginning of ignition (Ref. 18):

"The rapid rise in heat-release rate observed at injection velocities of 120 to 140 feet per second is attributed to an increase in temperature. In this velocity range it appears that heat generated in the interfacial area can no longer be dissipated to the surrounding fluid at a sufficient rate, and therefore the temperature of the reacting material increases, which results in an exponential increase in heat-release rate."

The onset of ignition in the terms defined by Feiler represents a microscopic view of the heat release per unit of heat available. Macroscopically this heat released determines the average rise in temperature of the liquid (i.e., after thermal transport has occurred.) The heat is released on a microscopic scale at an immisible interface, causing local heating. When sufficient contact time is allowed, heat is available to raise the average fluid temperature to an ignition level. The percentage of liquid-phase heat released is thus a guide to ignition. It should prove that when this number exceeds a certain value smooth ignition will occur. The percentage of heat released with impingement should thus prove to be a useful ignition indexing system for rating the smoothness of start-up and operation of injector devices. This index number is given by the formula:

$$I_I = \frac{R_{\max} T_{\text{mix}}}{\Delta H_R}$$

where R_{\max} (Figure 75) and T_{mix} are defined s in Section IV-1.

4. Conclusions

(a) The percentage liquid phase heat release of typical impinging hypergolic streams (MMH, Hydrazine/NTO) was estimated at 0.01%. If this amount of heat went to heat the remaining liquid it would lead to a temperature rise of approximately 4°K. The percentage of liquid reacted upon impingement appears to be negligible, while the amount of heat released may cause a measurable liquid phase temperature rise. However, the calculated 4°K temperature rise is not significant enough to warrant its inclusion in state-of-the-art rocket chamber calculations.

(b) The data used to estimate the percentage liquid phase heat release also lead to the postulation of an interfacial resistance to mass transfer as the reaction rate controlling mechanism. It was postulated that this interfacial resistance would predominate when reaction kinetics were faster than mixing times and when there was sufficient pressure potential generated from the reaction. These two conditions were satisfied for the cases of Hydrazine/NTO and MMH/NTO.

(c) Therefore, based upon conclusions (a) and (b), typical MMH/NTO or Hydrazine/NTO streams will separate without significant heat release under conditions of simple impingement.

(d) Feiler and Somogyi explain their heat release curves in terms of a tendency to local ignition at the interfacial surface. Based upon their physical description and their measurement of maximum heat release rates, an index for rating ignition and start-up devices was developed.

V. ATOMIZATION

Combustion calculations based upon droplet vaporization models require that the distribution of drop sizes be known. Many experiments have been performed and empirical distribution functions have been determined. However, there is little current agreement on which distribution function is most satisfactory. Since all the empirical distribution functions have particular shortcomings, a theoretical distribution function has been derived here. Among other advantages, this theoretical distribution allows relation of the droplet size to the physical injection process. Derivation of this distribution involves determining the most probable way in which a given amount of surface energy would be distributed among a group of drops having a given total mass. The derivation is presented here; and it is shown that the theoretical distribution fits experimental data and can be related to atomization efficiency.

Of the several better known distribution functions commonly used to describe atomized drop sizes none have been related by theory to parameters of the atomization process. The Nukiyama-Tanasawa, (Ref. 22) Rosin-Rammler, (Ref. 23), Logarithmic-normal, (Ref. 24) and Upper-Limit distributions (Ref. 25) are primarily useful for fitting curves to observed data. The first three contain two distribution parameters, one representing some mean diameter and the other the dispersion. The values of these parameters are adjusted to fit the data in question. The last function, the Upper-Limit, is a modification of the Logarithmic-normal distribution to give the distribution an upper limit to conform better with some observed data. The former three distributions allow for infinite drop diameters as a possibility. The Upper-limit distribution includes a third parameter, which, however, may be related to the conditions of the atomization process. At best, then, with any of these distribution functions the mean drop size and dispersion cannot be characterized except through observation. However, there is a distribution that might be related to the atomization process. That would be the most probable thermodynamic distribution. Attempts to apply a thermodynamic distribution to atomized dispersions has not been reported previously and should be examined.

1. Theoretical Development

Consider an atomizer or nozzle which in a given increment of time discharges N_T total number of drops, having associated with them a quantity of energy E_T , where

$$N_T = \sum_i N_i$$

and

$$E_T = \sum_i \epsilon_i N_i$$

where N_i = number of drops possessing a particular energy level/drop.

ϵ_i = energy level of a single drop belonging to the i^{th} group.

If all energy states have equal probability of occurring and the drops are distinguishable with no degeneracy, with the two constraints of N_T and E_T being fixed the most probable thermodynamic distribution is the Maxwell-Boltzmann distribution

$$N_i = e^{-\lambda - \beta \epsilon_i}$$

where λ and β are Lagrangian multipliers.

$$\text{Then } N_T = \sum_i e^{-\lambda - \beta \epsilon_i}$$

$$E_T = \sum_i \epsilon_i e^{-\lambda - \beta \epsilon_i}$$

Now if the energy of each drop ϵ_i is related to the size of the drop, the drop size distribution can be determined. For example suppose that the distributed energy is that of surface energy, then,

$$\epsilon_i = \sigma \pi D_i^2$$

where σ is the energy per unit surface area of the drop.

For large numbers of drops we can write.

$$N_T = \int_0^{\infty} e^{-\lambda - \beta \sigma \pi D^2} dD$$

and

$$E_T = \int_0^{\infty} \sigma \pi D^2 e^{-\lambda - \beta \sigma \pi D^2} dD$$

These equations yield values β and λ .

$$\beta = \frac{N_T}{2E_T}$$

$$\lambda = - \ln \left\{ N_T \sqrt{\frac{2H_T \sigma}{E_T}} \right\}$$

Now D_{20} is defined by

$$\pi D_{20}^2 N_T = \sum_i \pi D_i^2 N_i$$

where:

$$D_{20} = \left(\frac{\sum D_i^2 n_i}{\sum n_i} \right)^{1/2} \quad \text{and generally,} \quad D_{no} = \left(\frac{\sum D_i^n n_i}{N_T} \right)^{1/n}$$

$$\text{Then } \sigma \pi D_{20}^2 N_T = \sum_i \sigma \pi D_i^2 N_i = E_T$$

The number cumulative distribution function $F(N)$, the number fraction of drops with diameter equal to or less than D , is given by -

$$F(N) = \sqrt{\frac{2}{\pi}} \int_0^{\frac{D}{D_{20}}} e^{-\frac{1}{2} t^2} dt \quad \text{or} \quad F(N) = \text{erf} \left(\sqrt{\frac{1}{2}} \frac{D}{D_{20}} \right)$$

and the probability density function $f(N)$ associated with $F(N)$ is

$$f(N) = \frac{dF(N)}{d(D/D_{20})} = \sqrt{\frac{2}{\pi}} e^{-\frac{1}{2} \left(\frac{D}{D_{20}} \right)^2}$$

The volumetric distribution function $F(v)$, the volume fraction of the total drops with diameter equal to or less than D is

$$F(v) = \frac{1}{4} \int_0^{\frac{D}{D_{20}}} t^2 e^{-\frac{1}{2} t^2} dt$$

$$\text{or} \quad F(v) = \Psi(P) = 1 - e^{-P} (P+1)$$

$$\text{where } P = \frac{1}{2} \left(\frac{D}{D_{20}} \right)^2$$

and the probability density function associated with $F(v)$ is

$$f(v) 2 \frac{dF(v)}{d\left(\frac{D}{D_{20}}\right)} = \frac{1}{2} \left(\frac{D}{D_{20}}\right)^3 e^{-\frac{1}{2} \left(\frac{D}{D_{20}}\right)^2}$$

Furthermore the total volume V_T of the N_T drops can be shown to be

$$V_T = \frac{1}{3} \sqrt{2\pi} N_T D_{20}^3$$

which since D_{30} is defined by

$$V_T = \frac{1}{6} N_T \pi D_{30}^3$$

leads to a relationship between D_{20} and D_{30} .

$$\left(\frac{D_{30}}{D_{20}}\right)^3 = \sqrt{\frac{8}{\pi}}$$

From this the Sauter-mean diameter can be found to be

$$D_{32} = \frac{D_{30}^3}{D_{20}^2} = \sqrt{\frac{8}{\pi}} D_{20}$$

and the ratio of total energy to total mass

$$\frac{E_T}{\rho V_T} = \frac{6\sigma}{\rho D_{32}} = 6 \sqrt{\frac{\pi}{8}} \frac{\sigma}{\rho D_{20}}$$

The last expression is a most significant one in that it relates the ratio of total energy per mass to the average surface diameter of the atomized spray through the physical properties of the fluid system. Thus if the energy per mass could be determined from the physical circumstances for a particular atomization the drop size distribution would be completely described.

Up until now no limitations have been placed on the possible diameters of the drops. However, another distribution can be developed by an identical approach which limits the possible diameters to a range between a lower and upper diameter D_L and D_U . The resulting equations are,

$$F(N) = \frac{\text{erf}(\sqrt{P}) - \text{erf}(\sqrt{P_L})}{\text{erf}(\sqrt{P_U}) - \text{erf}(\sqrt{P_L})}$$

$$\text{where } P = \phi \left(\frac{D}{D_{20}} \right)^2$$

and

$$\phi = \frac{\gamma\left(\frac{3}{2}, P_U\right) - \gamma\left(\frac{3}{2}, P_L\right)}{\gamma\left(\frac{1}{2}, P_U\right) - \gamma\left(\frac{1}{2}, P_L\right)}$$

where $\gamma(v, x)$ is the incomplete gamma function defined as

$$\gamma(v, x) = \int_0^x t^{v-1} e^{-t} dt$$

Note that $\sqrt{\pi} \text{erf}(x) = \gamma\left(\frac{1}{2}, x^2\right)$ so that $F(N)$ can be written finally as Cumulative number distribution

$$F(N) = \frac{\gamma\left(\frac{1}{2}, P\right) - \gamma\left(\frac{1}{2}, P_L\right)}{\gamma\left(\frac{1}{2}, P_U\right) - \gamma\left(\frac{1}{2}, P_L\right)}$$

and the Probability density becomes

$$f(N) = \frac{\sqrt{2} e^{-\phi \left(\frac{D}{D_{20}} \right)^2}}{\gamma\left(\frac{1}{2}, P_U\right) - \gamma\left(\frac{1}{2}, P_L\right)} = \frac{\sqrt{2} e^{-P}}{\gamma\left(\frac{1}{2}, P_U\right) - \gamma\left(\frac{1}{2}, P_L\right)}$$

The remaining final equations corresponding to those developed for no maximum or minimum diameter are

Cumulative volume distribution

$$F(V) = \frac{\psi(P) - \psi(P_L)}{\psi(P_U) - \psi(P_L)}$$

Volume probability density

$$f(V) = 2\phi^2 \frac{D}{D_{20}} \frac{e^{-\phi \left(\frac{D}{D_{20}} \right)^2}}{\psi(P_U) - \psi(P_L)}$$

Relationship between D₂₀ and D₃₀

$$\left(\sqrt{\phi} \frac{D_{30}}{D_{20}}\right)^3 = \frac{\psi(P_U) - \psi(P_L)}{\gamma\left(\frac{1}{2}, P_U\right) \gamma\left(\frac{1}{2}, P_L\right)}$$

Sauter mean diameter

$$\phi^{3/2} D_{32} = D_{20} \frac{\psi(P_U) - \psi(P_L)}{\gamma\left(\frac{1}{2}, P_U\right) \gamma\left(\frac{1}{2}, P_L\right)}$$

When $P_L \rightarrow 0$ and $P_U \rightarrow \infty$ these equations reduce to the simpler case given before.

2. Theoretical Distribution Function Compared to Experimental Data.

At the present time only a preliminary evaluation of the usefulness of the derived distribution has been made. Experimentally measured distributions by several investigators have been compared to the distribution functions above as shown in Figures V-1, 2, 3. These comparisons pertain only to the ability of the functions to account for the observed dispersion of drop diameters purely as a function of the observed mean drop diameter, in this case the surface average diameter. In other words the comparisons are merely tests of the distribution function to "fit" the data.

The results of these first comparisons are very encouraging. In some cases the theoretical distribution does an excellent job of predicting the number of drops even at the extremes of the diameter ranges. Furthermore, in situations where only some mean diameter were known and nothing known about the dispersion, the theoretical distribution might provide a reasonable estimate of the distribution for many engineering problems. (Note: a mean diameter based upon any definition is suitable since for a given distribution function all mean diameters can be related). Where this is possible the theoretical distribution has a distinct advantage over the empirical distributions which have been proposed, since various investigators have determined empirical models for predicting mean diameters for some nozzle types, but in many cases have failed

DROP SIZE DISTRIBUTION FROM TWO IMPINGING JETS
 Foster, H., and Heidmann, M., Spatial Characteristics
 to Two Impinging Jets at Several Jet Velocities in
 Quiescent Air, NASA TN D-301, July 1960

$D_{20} = 208$ microns

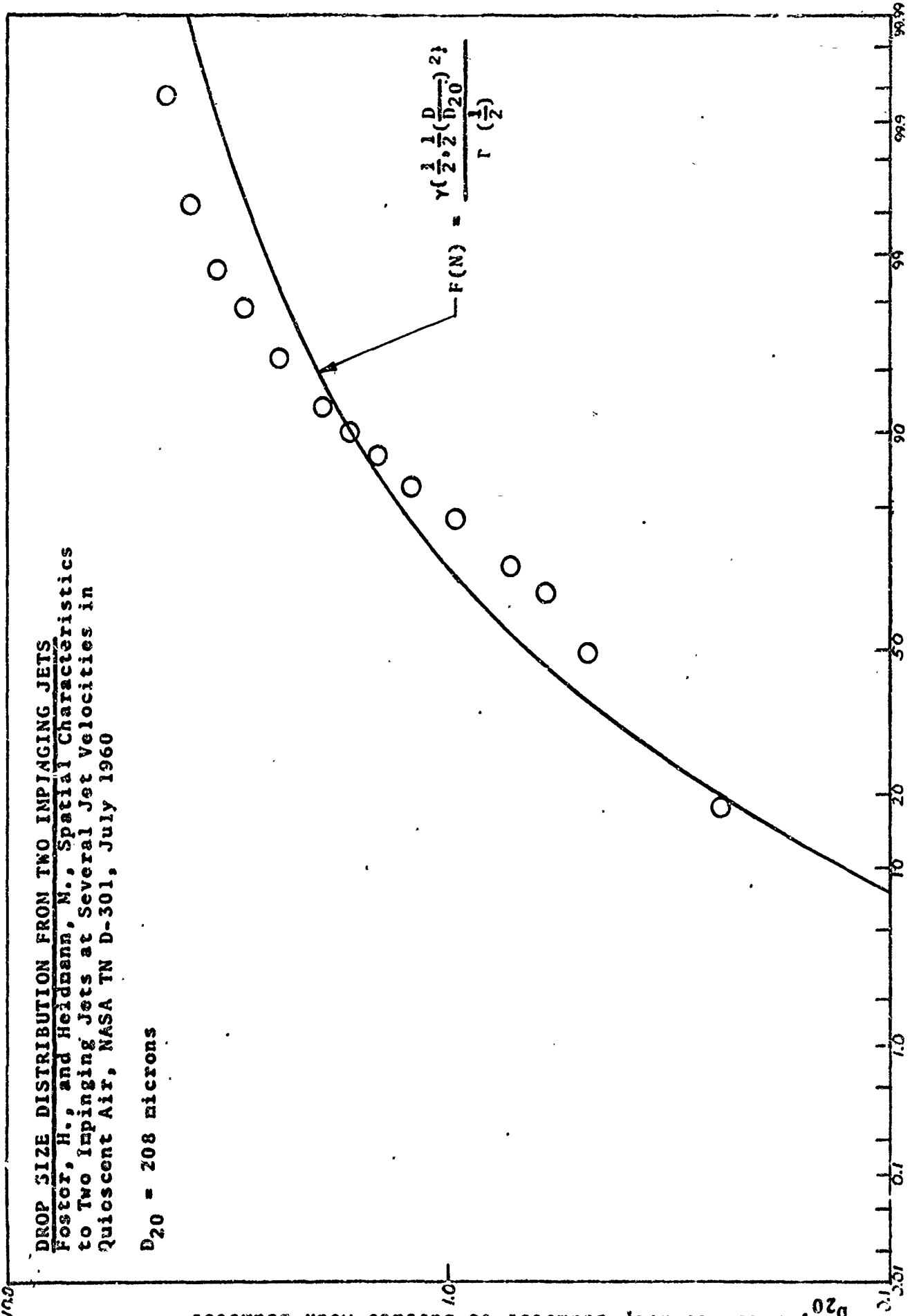


FIGURE 77 F(N), Cumulative Number Percent

$D_{p,0}$ Ratio of drop diameter to surface mean diameter

- 01
- △ 04
- △ 07
- △ 10
- △ 13
- △ 16
- △ 19
- 22

DROP SIZE DISTRIBUTION FROM TWO IMPINGING JETS
 Bittker, D. A., Effect of Ambient Air Velocity on
 Atomization of Two Impinging Water Jets, NASA TN D-2087, February 1964
 (See Legend for detail)

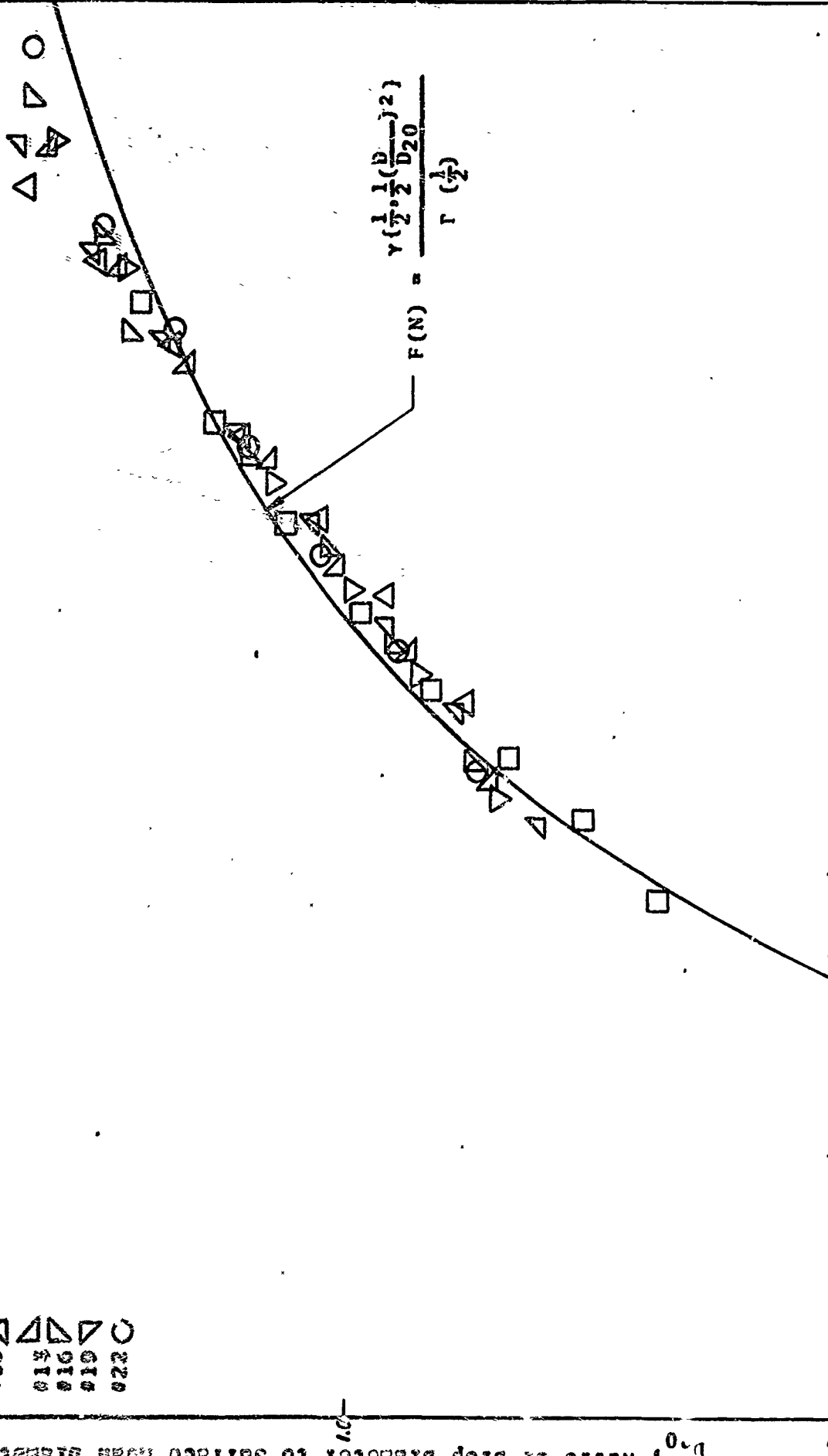


FIGURE 78 F(N), Cumulative Number Percent

Legend For

DROP SIZE DISTRIBUTION FROM TWO IMPINGING JETS

Bittker, D. A., Effect of Ambient Air Velocity on Atomization of Two Impinging Water Jets, NASA TN D-2087, February, 1964

Impingement Angle	Jet Velocity ft./sec.	Sampling Distance, Inches	Air Velocity Minus Jet Velocity ft./sec	Surface Mean Diameter, μ
#1 □	30	16	0	1212
#4 △	30	16	120	493
#7 ▽	74	16	60	573
#10 ▲	30	16	30	687
#13 ▽	60	8	-30	549
#16 ▽	60	8	60	514
#19 ▽	74	8	30	498
#22 ○	30	8	37	507

123

(Legend for Figure 78)

FIGURE 79

DROP SIZE DISTRIBUTION OF BURNING DROPS
 Ingobo, R.D., Photomicrographic Tracking of
 Ethanol Drops in a Rocket Chamber Burning
 Ethanol and Liquid Oxygen, NASA TN D-290, June 1960

$D_{20} = 140\mu$

$$F(N) = \frac{\gamma(\frac{1}{2}, \frac{1}{2}(D/D_{20})^2)}{\Gamma(\frac{1}{2})}$$

$$F(N) = \frac{\gamma(\frac{1}{2}, \phi(\frac{D}{D_{20}})^2)}{\gamma(\frac{1}{2}, \phi(\frac{D_u}{D_{20}})^2)}$$

$$\phi = 0.43 \quad D_u = 344\mu$$

921 $\frac{D}{D_{20}}$, Ratio of Drop Diameter to Surface Mean Diameter

0.1 0.1 1.0 1.0 10 10 50 50 90 90 99 99 99.9 99.9

FIGURE 80. $F(N)$, Cumulative Number Percent

to relate the drop size dispersion to any useful physical parameters, and therefore cannot determine the distribution where needed.

A second significant feature of the theoretical distribution is that it opens an avenue of investigation for predicting drop sizes heretofore only briefly explored. According to the development of the distribution function the mean surface diameter should be related to the specific surface energy of the spray. This implies that examination of the energy exchanges involved in the atomization process of some nozzles might be used to predict drop size distributions. Thus a thermodynamic approach rather than a fluid mechanical one may prove fruitful. Certainly for some nozzles, formulation of a fluid mechanical model is almost hopelessly complex, when for the same nozzle a thermodynamic examination is feasible.

In the development of the distribution function presented here, only the surface energy of the drops was considered. Actually other forms of energy such as kinetic and vibrational energies might be distributed as a function of drop size and would affect the thermodynamic distribution. Some consideration of these factors should be included in any future investigations of the relation between drop size distribution and the distributed energy.

3. Correlation of Atomization to Process Parameters.

Considering only the surface energy it has been shown that the sprays from some nozzles can be "fit" very well by the theoretical distribution. Two questions for immediate investigation would appear to be:

(a) Can the deviations of some distributions from the theoretical distribution be related to nozzle type, experimental method used, or other physical parameters of the system?

(b) Can the surface energy of the drops formed by a nozzle be calculated from examination of the energy exchanges in the atomization process with sufficient accuracy to be useful in predicting mean drop diameter? If so, then the efficiency of an atomizer in converting kinetic energy into surface energy could be correlated directly to give mean diameter and thus droplet distribution.

Some answers to both questions might be found in very careful examination of the many sets of data already reported in the literature. It is also likely that additional experimental measurements might be needed to supplement the available data, but no concrete suggestions for experimental study can be proposed until an analytical investigation is made.

4. Conclusions

On the basis of what has been accomplished so far it can be said that a theoretical distribution of drop sizes can be derived which is related to the physical process of atomization and the properties of the fluid. These parameters determine the efficiency of surface energy production by particular atomizer devices. Preliminary tests of this distribution for "fitting" data are encouraging. Ability to predict the surface energy from the energy exchanges in the atomization process have yet to be tested. The theoretical distribution which has been developed here should serve as a valuable limiting case for comparison and help in correlation. In addition it gives physical meaning to distribution fitting attempts.

REFERENCES

1. Beltran, M. R., et al, "Analysis of Liquid Rocket Engine Combustion Instability," Air Force Rocket Propulsion Laboratory Technical Report No. AFRPL-TR-65-254, January 1966.
2. Beltran, M. R., Breen, B. P., and Gerstein, M., "Liquid Rocket Engine Combustion Instability Studies," Dynamic Science Corporation Semiannual Report No. SN-68-S1, Monrovia, California, 1965.
3. Priem, R. J. and Heidmann, M. F., "Propellant Vaporization As a Design Criteria for Rocket Engine Combustion Chambers," NASA TR R-67, 1960.
4. Heidmann, M. F. and Foster, H. H., "Effect of Impingement Angle on Drop Size Distribution and Spray Pattern of Two Impinging Water Jets," NASA Tech. Note D-872, 1961.
5. Bittker, D. A., "Effect of Ambient Air Velocity on Atomization of Two Impinging Water Jets," NASA Tech. Note D-2087, 1964.
6. Bevans, R. S., "Mathematical Expressions for Drop Size Distributions in Sprays," Paper at Conference of Fuel Sprays, University of Michigan, 1949.
7. Ingobo, R. D., and Foster, H. H., "Drop Size Distribution for Crosscurrent Breakup of Liquid Jets in Airstreams," NACA Tech. Note 4087, 1957.
8. Ingobo, R. D., "Drop Size Distributions for Impinging Jet Breakup in Airstreams Simulating the Velocity Conditions in Rocket Combustors," NACA Tech. Note, 4222.
9. Ingobo, R. D., "Photomicrographic Tracking of Ethanol Drops in a Rocket Chamber Burning Ethanol and Liquid Oxygen," NACA Tech. Note D-290, 1960.
10. Murrington and Richardson, "The Breakup of Liquid Jets," Proc. of the Physical Soc., Vol. 59, Part 1, No. 331, p 1, 1947.
11. Giffen, E. and Lamb, T.A.J., "The Effect of Air Density on Spray Atomization," Motor Industry Research Assn. Report No. 1953/5, 1953.
12. Radcliffe, A., "The Performance of a Type of Swirl Atomizer," Proc. Inst. Mech. Eng., Vol. 169, pp 93-100, 1955.

13. Fraser, R. P. and Eisenklam, P., "Liquid Atomization and the Drop Size of Sprays," Trans., Inst. Chem. Engrs. Vol. 34, pp 294-319, 1956.
14. Lewis, J. D. and Squibbs, N. E., Unpublished work at R.P.E. Westcott, 1958.
15. Gardiner, J.A., Unpublished work at N.G.T.E., Pyestock, 1961.
16. Epstein, P.S. and Carhart, R.R., "The Absorption of Sound in Suspensions and Emulsions, I. Water Fog in Air," No. 3 pp 553-565, 1953.
17. Weiss, R. R., R. D. Klopotek, "Experimental Evaluation of the Titan III Transtage Engine Combustion Stability Characteristics," Air Force Rocket Propulsion Laboratory Technical Report No. AFRPL-TR-66-51, March, 1966.
18. Somogyi, Dezo and Feiler, C. E., "Liquid-Phase Heat Release Rates of the Systems Hydrazine Nitric Acid and Unsymmetrical Dimethylhydrazine-Nitric Acid," NASA TN-D-469, September 1960.
19. Sawyer, R. F. and Glassman, I., "Reaction Kinetics of the Hydrazine-Nitrogen Tetroxide Propellant System," CPIA Publication No. 95, September 1965.
20. Wells, H. G. and Johnson, Bruce, "Modification of the Hydrazine-Nitrogen Tetroxide Ignition Delay," AIAA Journal pp 2222-2223, December 1964.
21. Rupe, Jack H., "On the Dynamic Characteristics of Free-Liquid Jets and a Partial Correlation with Orifice Geometry," JPL Tech Rept. No. 32-207, 1962.
22. Nukiyama, Shiro, and Tanasawa, Yasushi (E. Hope, trans): "Experiments on the Atomization of Liquids in an Air Stream" Rept. No. 3, on the Droplet-Size Distribution in an Atomized Jet, Defence Res. Board, Dept. Natl. Defence, Ottawa (Canada), March 18, 1950, (Trans. from Trans. Soc. Mech. Eng. (Japan), Vol. 5, No. 18, Feb. 1939, pp 62-67.
23. Rosin P., and Rammler, E.: "The Laws Governing the Fineness of Powdered Coat," J. Inst. Fuel. Vol. 7, No. 31, Oct. 1933 pp 29-36.
24. Epstein, Benjamin, "Logarithmico-Normal Distribution in Breakage of Solids," Ind. & Eng. Chem, Vol. 40, No. 12 December 1948, pp 2289-2291.
25. Mugolo, R.A., and Evans, H.D.: "Droplet Size Distribution in Sprays," Ind. and Eng. Chem. Vol. 43, No. 6, June, 1951, pp 1317.

Unclassified
Security Classification:

DOCUMENT CONTROL DATA - R&D

(Security classification of title, body of abstract and indexing annotation must be entered when the overall report is classified)

1. ORIGINATING ACTIVITY (Corporate author) Dynamic Science, A Division of Marshall Industries, 1900 Walker Avenue, Monrovia, California	2a. REPORT SECURITY CLASSIFICATION Unclassified
	2b. GROUP Propulsion

3. REPORT TITLE

LIQUID ROCKET ENGINE COMBUSTION INSTABILITY STUDIES

4. DESCRIPTIVE NOTES (Type of report and inclusive dates)

R&D - January 1, 1965 - March 31, 1966

5. AUTHOR(S) (Last name, first name, initial)

M. R. Beltran	C. F. Sanders
B. P. Breen	R. J. Hoffman
T. C. Kosvic	R. O. Wright

6. REPORT DATE

1 July 1966

7a. TOTAL NO. OF PAGES

137

7b. NO. OF REFS

25

8a. CONTRACT OR GRANT NO.

AF 04(611)-10542

b. PROJECT NO.

3505

9a. ORIGINATOR'S REPORT NUMBER(S)

SN-68-F

9b. OTHER REPORT NO(S) (Any other numbers that may be assigned this report)

AFRFL-TR-66-125

10. AVAILABILITY/LIMITATION NOTICES

Qualified users may obtain copies from the Defense Documentation Center

11. SUPPLEMENTARY NOTES

12. SPONSORING MILITARY ACTIVITY

Air Force Rocket Propulsion Lab.
Research and Technology Division
Edwards Air Force Base, California

13. ABSTRACT

This final report describes the work performed on various combustion problems related to high frequency instability in liquid rocket engines. Using the steady-state and instability computer programs developed under this study, a parametric investigation was conducted. This investigation determined the influence of droplet radius, droplet distribution, injection velocity, chamber pressure, and mixture ratio on the minimum threshold disturbance required to trigger combustion instability in a Transtage type engine configuration. The propellant combination considered was monomethylhydrazine/nitrogen tetroxide. Results of the study show that increases in injection velocity and droplet distribution increased stability. An increase in chamber pressure, based on constant flow rate increased stability while increases in chamber pressure, at a constant contraction ratio, decreased stability. There appears to be a droplet size for minimum stability, with changes in either direction resulting in improved stability. Results also show that due to the vapor phase reactions, monomethylhydrazine/nitrogen tetroxide vaporize at approximately the same rate. Thus, the oxidizer or fuel could be made to control the combustion process by slight changes in the injector and engine parameters. For the engine configuration studied the oxidizer vaporized slower than the fuel. A program review summarizes the work reported in the Semiannual (DSC SN-68-51) and Special report (AFRPL-TR-65-254 written under this program.

DD FORM 1473
1 JAN 64

Security Classification